



TECHNISCHE
UNIVERSITÄT
WIEN
Vienna University of Technology

Diplomarbeit

Detailed fluid dynamic investigations of the fuel reactor of a novel DUAL FLUID reactor concept for Chemical Looping Combustion for solid fuels

ausgeführt zum Zwecke der Erlangung des akademischen Grades eines
Diplom-Ingenieurs unter der Leitung von

Univ. Prof. Dipl.-Ing. Dr. techn. Hermann Hofbauer

Dipl.-Ing. Stefan Penthor

Dipl.-Ing. (FH) Johannes C. Schmid

E166

Institut für Verfahrenstechnik, Umwelttechnik und Technische Biowissenschaften

eingereicht an der Technischen Universität Wien
Fakultät für Maschinenwesen und Betriebswissenschaften

von

Michael Stollhof

Matrikelnummer: 0425352

Favoritenstraße 180/1/26

1100 Wien

Wien, Mai 2014

.....
Michael Stollhof

Danksagung

An dieser Stelle möchte ich mich bei all jenen Personen bedanken die mich bei der Verwirklichung dieser Arbeit unterstützt haben.

Zunächst möchte ich mich bei Dipl.-Ing. (FH) Johannes C. Schmid für die Bereitstellung des Kaltmodells sowie der Unterstützung bei den Umbauarbeiten bedanken. Bei Dipl.-Ing. Stefan Penthor, meinem Betreuer, möchte ich mich für seine konstruktiven Ratschläge wie auch das angenehme und produktive Arbeitsklima bedanken. Des Weiteren möchte ich Univ. Prof. Dipl.-Ing. Dr. techn. Hermann Hofbauer für die Ermöglichung dieser Arbeit an dem Institut für Verfahrenstechnik, Umwelttechnik und Technische Biowissenschaften danken. Ein Dankeschön geht auch an die Arbeitsgruppe Zero Emission Technologies für die freundliche Atmosphäre und Hilfsbereitschaft.

Außerdem will ich mich an dieser Stelle auch noch besonders bei meinen Eltern, Margarete und Ewald Stollhof, für Ihre Unterstützung während der gesamten Studienzeit herzlich bedanken.

Abstract

Since the beginning of the industrial revolution, the demand for energy and consequently the CO₂ emissions have strongly increased. As CO₂ represents the greenhouse gas with the strongest influence on the greenhouse effect, which influences the Earth's temperature, this is also recognizable at an increase of the mean global temperature in the last centuries. Since a CO₂ neutral energy production cannot be expected in the near future, it will be necessary to develop solutions for the reduction of CO₂ emissions.

A mid-term solution represents the concept of carbon capture and storage (CCS), which means to capture CO₂ from large point sources and transport it to storage sites. An energy efficient method for the separation of CO₂ in a combustion process is chemical looping combustion (CLC). The main idea is to divide the combustion process into two steps which take place in two different zones, so that air and fuel are never mixed. An oxygen carrier, a metal oxide, transports the oxygen from the so called air reactor (AR) to the fuel reactor (FR) where the oxidation of the fuel takes place. Thereby the exhaust gas stream of the FR consists ideally only of H₂O and CO₂. Afterwards the CO₂ can be easily separated by condensation.

The objective of this thesis is the investigation of a cold flow model (CFM) of a fluidized bed system which operates according to the novel DUAL FLUID reactor concept. This new reactor concept constitutes an advanced development of the Dual Circulating Fluidized Bed technology (DCFB), with simple geometrical constrictions inside the FR. The main idea behind these periodic constrictions is to increase the solid fraction over the entire height of the FR as well as to improve the contact between the solid and fluid.

To investigate the influence of the constrictions on the behavior of the CFM, a pressure measuring system was used, recording the pressure at 40 positions of the CFM. In addition, a mathematical model based on the conservation of mass and equation of motion, was developed to simulate the influence of the constrictions. For the determination of the solid mass flows in the CFM, measurements of the global and internal circulation were performed.

Both, the pressure observations at the CFM and the mathematical model clearly confirm the expected increase of the solid fraction over the height of the FR. This can be seen at a dramatically increasing pressure gradient over the constrictions compared to that between the constrictions (up to more than 100 times). Further, the highest particle concentration could be identified in the upper part of the constrictions. The solid distribution over the height of the FR can be influenced by AR and FR fluidization rate, whereby the share of the solid distribution of the upper parts increases with increasing fluidization rates. In contrast to the solid distribution of the whole FR, the investigated pressure distribution between two constrictions indicates that the solid distribution is not influenced by the AR and FR fluidization rates. During the experiments limitations of the operating range of the CFM could be observed. This limitation of the operating range depends on the ratio of the AR to FR fluidization rate. Further, the mechanisms which lead to these limitations could be identified using the mathematical model for the simulation of the influence of the constrictions. Investigations at the last stable operating points showed that the FR contains always similar amount of solid particles at the transition to

unstable operation. Further, it shows that at the solids distribution initially changes for an operation near to unstable operation.

Kurzfassung

Seit Anbeginn der Industriellen Revolution hat der Energiebedarf und damit der Ausstoß von CO₂ stark zugenommen. Da CO₂ jenes Treibhausgas mit dem größten Einfluss auf den Treibhauseffekt, welcher die Temperatur der Erdoberfläche beeinflusst, bemerkbar ist dies auch an einem Anstieg der mittleren globalen Temperatur. Da in naher Zukunft nicht mit einer CO₂-neutralen Energieproduktion gerechnet werden kann, wird es notwendig sein Lösungen für die Reduzierung des Ausstoß von CO₂ zu finden.

Eine Übergangslösung stellt das Konzept der CO₂ Abscheidung und Speicherung (Carbon Capture and Storage - CCS) dar. Dabei wird CO₂ an Stellen, an denen es in großen Mengen anfällt abgeschieden und danach zu Lagerstätten weitertransportiert. Eine energieeffiziente Methode für die Abscheidung von CO₂ für Verbrennungsprozesse ist Chemical Looping Combustion (CLC). Die Grundidee dabei ist die Aufteilung des Verbrennungsprozesses in zwei Schritte, welche in zwei verschiedenen Zonen stattfinden, sodass Luft und Brennstoff nie vermischt werden. Ein Sauerstoffträger, ein Metalloxid, transportiert den Sauerstoff von dem sogenannten „Air Reactor“ (AR) in den „Fuel Reactor“ (FR) wo die Oxidation des Brennstoffes stattfindet. Der Abgasstrom des FR besteht dabei idealerweise nur aus H₂O und CO₂, wobei das H₂O danach einfach mittels Kondensation abgeschieden werden kann.

Ziel dieser Arbeit ist die Untersuchung eines Kaltmodells (Cold Flow Model - CFM) eines Wirbelschichtsystems, welches nach dem novel DUAL FLUID Reaktorkonzept arbeitet. Dieses neue Reaktorkonzept, mit simplen geometrischen Einschnürungen im FR, stellt eine Weiterentwicklung des Dual Circulating Fluidized Bed (DCFB) dar. Der Grundgedanke hinter den periodischen Einschnürungen ist eine Erhöhung des Feststoffanteils über die gesamte Höhe des FR, sowie eine Verbesserung des Kontaktes zwischen Feststoff und Fluid.

Um den Einfluss der Einschnürungen auf das Verhalten des CFM zu untersuchen wurde ein Druckmesssystem verwendet, um den Druck an 40 Positionen am Kaltmodell aufzuzeichnen. Zusätzlich wurde ein mathematisches Modell erstellt, basierend auf Massenbilanz und Bewegungsgleichung, um den Einfluss der Einschnürungen zu simulieren. Zur Bestimmung der Feststoffmassenströme des CFM wurden der globale sowie der interne Umlauf bestimmt.

Sowohl die Druckmessungen am CFM als auch das mathematische Modell bestätigen eindeutig den erwarteten Anstieg des Feststoffanteils über die Höhe des FR. Dies ist ersichtlich an einem starken Anstieg des Druckgradienten über die Einschnürungen im Vergleich zu jenem zwischen den Einschnürungen (mehr als 100 mal größer). Zusätzlich konnte der höchste Feststoffkonzentration im oberen Teil der Einschnürungen identifiziert werden. Die Feststoffverteilung über die Höhe des FR kann mittels der AR als auch der FR Fluidisierungsrate beeinflusst werden, wobei jener Anteil im oberen Teil des FR mit der Fluidisierungsrate ansteigt. Im Gegensatz zur Feststoffverteilung im gesamten FR lässt die Druckverteilung zwischen zwei Einschnürungen vermuten, dass die Feststoffverteilung nicht von den AR und FR Fluidisierungsraten beeinflusst wird. Während den Untersuchungen wurden Einschränkungen des Betriebsbereiches des CFM festgestellt werden. Dabei konnte festgestellt werden, dass diese Einschränkungen von einem Verhältnis zwischen AR zu FR Fluidisierungsrate abhängig sind. Desweiteren konnten die Mechanismen welche zu diesen Einschränkungen des

Betriebsbereiches führen, mittels des mathematischen Modells identifiziert werden. Untersuchungen der letzten möglichen stabilen Betriebspunkte zeigen, dass der FR an den Betriebsgrenzen immer einen ähnlichen Feststoffanteil enthält. Zusätzlich wurde ersichtlich, dass sich die Feststoffverteilung zwischen den Einschnürungen, im Gegensatz zum normalen Betrieb, bei einem Betrieb nahe den Betriebsgrenzen verändert.

Contents

1.	Introduction.....	1
1.1	Development of the worldwide energy demand over time	1
1.2	Greenhouse effect and climate change	2
1.3	Carbon capture and storage.....	4
1.3.1	CO ₂ capture	5
1.3.2	CO ₂ transport.....	6
1.3.3	CO ₂ storage.....	7
1.4	Chemical looping combustion.....	8
1.5	Challenges in the application of CLC to solid fuels.....	9
1.6	Motivation and objectives.....	10
2.	Theoretical Background.....	11
2.4	Fluid dynamic background	11
2.4.1	Pressure changes in stationary flowing and incompressible fluids.....	11
2.4.2	Fluid dynamic dimensionless numbers	14
2.5	Fluidized bed technology	15
2.5.1	Particles	15
2.5.2	Fluid dynamic background	18
2.5.3	Fluidized bed regimes.....	21
2.5.4	Regime maps	22
2.6	Cold flow modeling	24
2.6.1	Scaling relationships by Glicksman	24
2.7	Calculation of the solid fraction in a fluidized bed.....	26
2.8	Novel DUAL FLUID reactor concept	27
3.	Experimental set-up	29
3.1	Description of the cold flow model.....	29
3.2	Bed material	32
3.2.1	Classification according to Geldart.....	32
3.2.2	Bed material of the CLC pilot plant	32
3.2.3	Bed material of the cold flow model.....	33
3.3	Application of scaling relationships.....	34
3.4	Measurement set-up.....	36
3.4.1	Volume-flow measurement	36

3.4.2	Pressure measurement	37
3.4.3	Solids mass flow measurement.....	40
3.4.4	Data-acquisition	41
4.	Mathematical model	42
5.	Results and Discussion.....	46
5.1	Overview of the pressure inside the CFM	46
5.1.1	Pressure without bed material.....	46
5.1.2	Pressure at the standard operating point	48
5.2	Solid circulation	50
5.2.1	Global circulation	50
5.2.2	Internal circulation	52
5.3	Solid distribution in the FR.....	53
5.3.1	Solid distribution by variation of the FR fluidization rate	54
5.3.2	Solid distribution by variation of the AR fluidization rate.....	56
5.4	Solid distribution in a chamber	58
5.4.1	Solid distribution without AR fluidization	59
5.4.2	Solid distribution by variation of the FR fluidization rate	60
5.4.3	Solid distribution by variation of the AR fluidization rate.....	62
5.5	Mean solid fraction in a chamber	64
5.6	Mechanisms influencing the operating range	65
5.6.1	Operating mechanisms	66
5.6.2	Operating limitations	70
5.6.3	Last stable operating points	72
6.	Conclusion	77
7.	References.....	78
8.	Nomenclature.....	80
9.	List of Figures.....	82
10.	List of Tables.....	84

1. Introduction

1.1 Development of the worldwide energy demand over time

Since the beginning of humanity, people used the energy which was available to them to improve their quality of life as well as to accelerate transport and production. While in the early years humanity was restricted to food and the muscle force received from it, it discovered soon additional energy sources. These were found in the mechanical energy received from wind and water as well as the thermal energy of biomass (e.g. wood). [1]

With the beginning of the industrial revolution the energy received from until then used energy sources, could no longer meet the demand. As a consequence, new energy sources had to be explored and were finally found in fossil fuels. Especially, the invention of the steam engine, which happened during this period, enabled the conversion from thermal into mechanical energy and facilitated the use of fossil fuels. [1]

As fossil fuels could now be easily extracted in large quantities, the amount of available energy increased strongly. However, the growth of energy consumption also implicated new problems. The use of fossil fuels involves the emission of green house gases, which are described in the following section. [1]

Today, as illustrated in Figure 1, the trend of an ongoing increasing energy demand continues. Thereby, the fossil fuels (coal, oil, natural gas) are still representing the main part of the primary energy sources. [2]

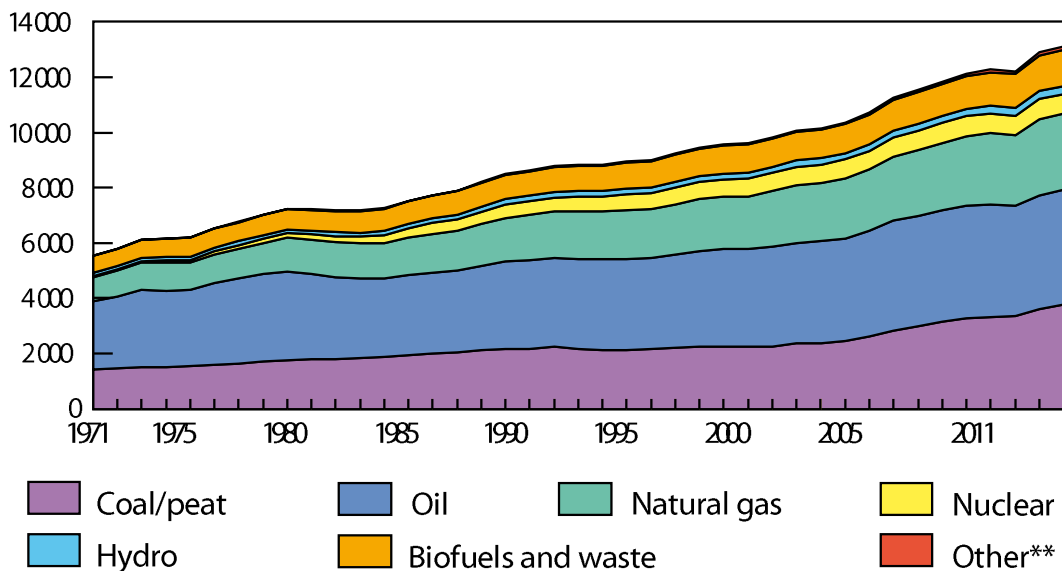


Figure 1: Development of the worldwide energy demand over time in million tons of oil equivalent (Mtoe) [2]

1.2 Greenhouse effect and climate change

The sun emits radiation at a temperature of 6000 K, which corresponds to a spectral peak of approximately 500 nm. At this wavelength the green house gases in the earth's atmosphere are largely transparent and absorb only a small part of the radiation. The incoming radiation from the sun gets absorbed by the earth's surface and warms it. The earth's surface itself also emits radiation, but due to its lower temperature, the spectral peak shifts towards longer wavelengths of approximately 10000 nm. At this wavelength a large part of the radiation gets absorbed by green house gases. They re-radiate in all directions, so that a part of the radiation is returned to the earth's surface and thereby further warms it. This effect is called the greenhouse effect. [3]

The influence of the individual green house gases on the greenhouse effect can be expressed by their radiative forcing measured in W/m^2 . Figure 2 shows the radiative forcing of the most important green house gases, which are carbon dioxide (CO_2), nitrous oxide (N_2O), and methane (CH_4). As the illustration shows, CO_2 dominates the radiative forcing and therefore represents the green house gas with the greatest influence on the greenhouse effect. Because of its great importance, CO_2 is used to express the effect of other green house gases. The equivalent carbon dioxide (CO_2e) gives the concentration of CO_2 that would cause the same radiative forcing than a specific concentration of another green house gas. [4]

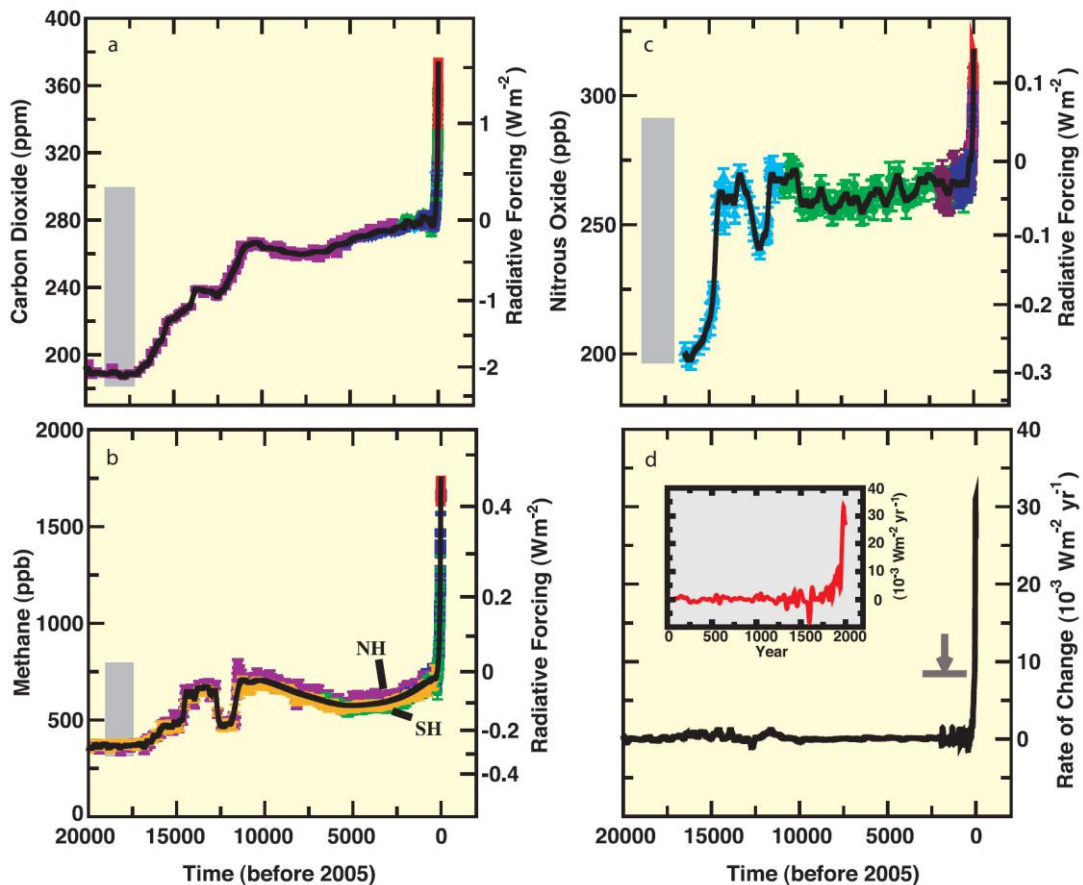


Figure 2: Influence of the most important green house gases expressed by their radiative forcing [4]

From Figure 3 it can be abstracted, that the emission of CO₂ is almost exclusively caused by combustion of fossil fuels, representing the most important energy source (86 %). As there are no indications until now that the proportion of the fossil fuels on the worldwide energy supply will change in the near future, it can be assumed that the demand of energy and the greenhouse effect will still correlate in the future. Furthermore, statistics show that the worldwide energy demand will increase over the next centuries. [5]

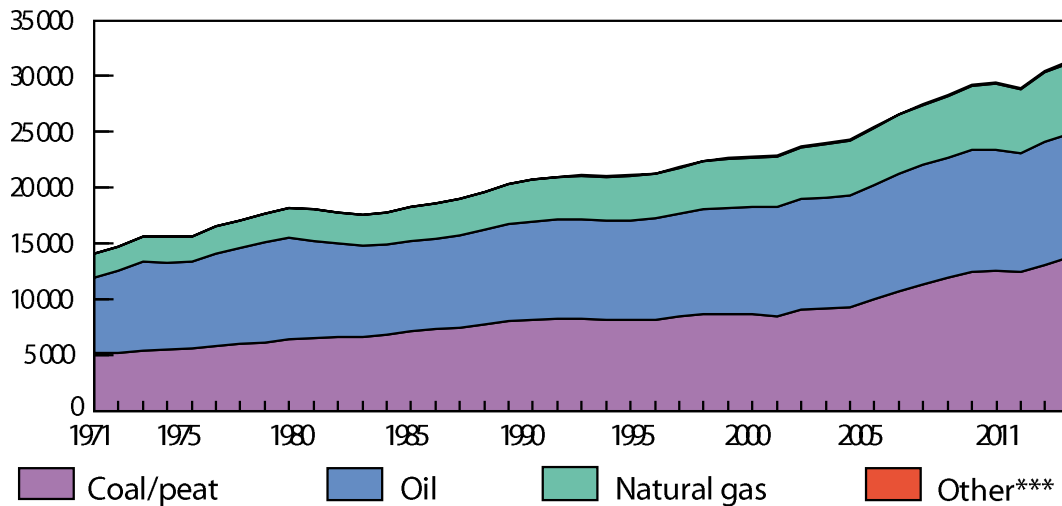


Figure 3: Development of the worldwide CO₂ emissions over time by fuel in megatonnes (Mt) [2]

According to the Intergovernmental Panel on Climate Change (IPCC) the average temperature of the Earth's surface has increased about 0.74 °C between 1906 and 2005. To keep the increase of the temperature below 2 °C compared to pre- industrial levels, the climate model of the IPCC predicts that the CO₂e concentration in the atmosphere has to be stabilized between 445 and 490 ppm. [4]

For a CO₂e concentration below 450 ppm, the International Energy Agency (IEA) proposes the 450 Scenario. According to this scenario, the CO₂e emissions have to be reduced by 49 % or 20.9 Gt until 2035 relative to the Current Policies Scenario, which takes the formally initiated policies until mid 2010 into account.

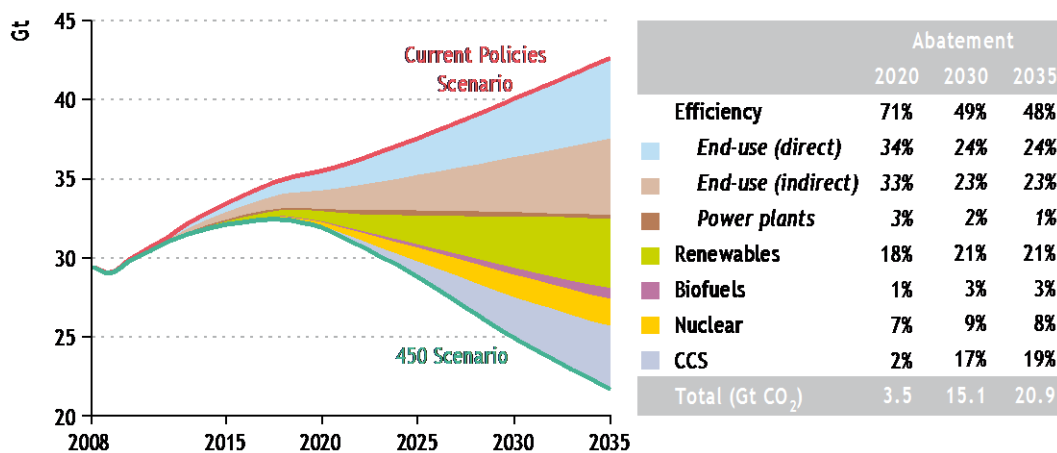


Figure 4: CO₂e savings relative to the Current Policies Scenario [5]

According to the IEA this reduction should be achieved as illustrated in Figure 4. Thereby, it is planned that beside the End-use efficiency and the use of renewables, also Carbon Capture and Storage (CCS) will account for a large part of the CO₂e savings with 19 % until 2035. [5]

1.3 Carbon capture and storage

The aim of CCS is to prevent the release of CO₂ into the atmosphere. It is planned to be applied to large CO₂ sources in industry and power generation like power plants, cement plants or refineries, which would be most effective for CO₂ capture. CCS implies the use of a technology for capturing emitted CO₂ at high concentrations, further to transport it to a suitable storage location, and to deposit it such that it will not enter the atmosphere for a long period of time. Therefore, CCS can be divided into three main steps, which are,

- CO₂ capture,
- CO₂ transport, and
- CO₂ storage.

Thereby, capturing CO₂ represents the most energy intensive part, while the storage is the most critical aspect with respect to safety of the environment. Transportation requires a high purity of the CO₂ stream to avoid condensation and corrosion. Further critical points are the amount in which CO₂ occurs and the efficiency losses associated with it. [6]

Figure 5 shows the emissions of a power plant with and without CCS as well as the net reduction of the CO₂ emissions.

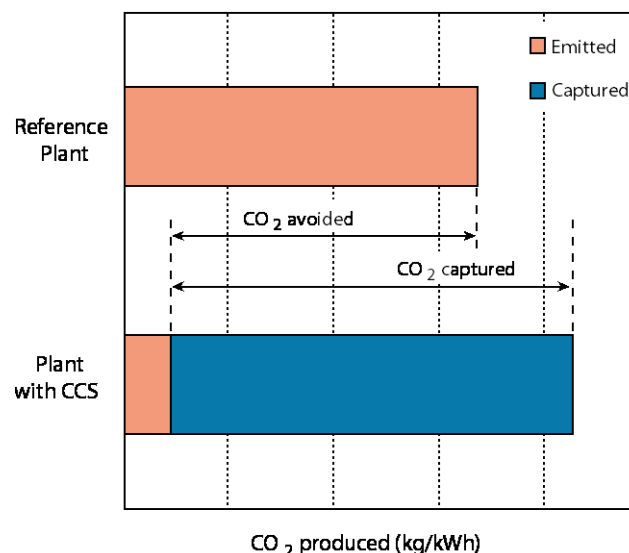


Figure 5: CO₂ emissions with and without CCS [6]

The power plant with CCS shows an increased CO₂ production, which is due to the decreased overall efficiency. This is a result of the additionally required energy for capture, transport and storage as well as leakages in the CCS system.

1.3.1 CO₂ capture

Until now, four groups of technologies for capturing CO₂ have been developed. The aim of all these technologies is to produce a highly concentrated CO₂ stream, to ensure transport and storage at acceptable costs. Until now, the capture of CO₂ at industrial scale is still under development and a commercial use cannot be expected until 2020. [6]

Post-combustion capture refers to a technology, which separates CO₂ from an exhaust gas stream after combustion by absorption or adsorption. The efficiency of the process depends to a large extent on the CO₂ concentration in the exhaust gas stream, whereby efficiency increases with concentration. As end of pipe technology, this technology can be applied to existing power plants. [6]

Pre-combustion capture is a technology that separates the CO₂ before combustion. Therefore, in a first step the fuel is converted into a synthesis gas (CO₂, CO and H₂), typically in a gasification or reforming process. In a next step the synthesis gas reacts with water steam to CO₂ and hydrogen (H₂). The CO₂ is then separated and the H₂ rich stream is used as decarbonized fuel. [6]

Oxyfuel is a combustion technology where oxygen (O₂) is separated from the air before it is used for combustion. Thereby, the combustion process with pure oxygen produces an exhaust gas stream which consists mainly of CO₂ and water steam (H₂O). Afterwards, the water can then be removed from the exhaust stream by condensation. Oxyfuel needs an air separation unit, to separate O₂ from the air, which reduces the overall plant efficiency. [6]

Unmixed Combustion refers to a technology, in which a chemical reaction is separated into two steps which take place in two different reaction zones. In one reaction O₂ gets selectively bound to a carrier material, while in another reaction the O₂ is used for combustion of the fuel. Therefore, air and fuel are never mixed and the exhaust gas stream consists ideally only of CO₂ and H₂O in form of steam. Afterwards, the water can be separated from the CO₂ by condensation. Examples for unmixed combustion are fuel cells or chemical looping combustion (CLC). [7]

1.3.2 CO₂ transport

After capturing the CO₂, it has to be transported from the point of capture to a storage site. The following opportunities are proposed:

- Transport by pipeline

The transport by pipeline represents the most common method for transporting CO₂ until now, as it is already used in the oil and gas industry. First, the gaseous CO₂ is compressed and then transported in a liquid state, making it easier and less costly to transport. To avoid a two-phase regime, the pressure has to be kept above 80 bar. The transport by pipeline is relatively safe and the losses are very small. [6, 7]

- Transport by ship, road or train

If CO₂ has to be transported over large distances or over sea, transport by ship may be a solution. For the transport, the CO₂ is liquified but kept under a lower pressure of 7 bar, compared to the transport by pipeline.

Transportation by road or train would be also possible, but they are more uneconomic than the transport by pipeline or ship and therefore rather unusual. The transport would be realized at a temperature of - 20 °C and a pressure of 20 bar.

As in Figure 6 illustrated, the transport by pipeline is more cost efficient for distances smaller than 1000 km for offshore transportation and 1700 km for onshore transportation, than the transport by ship. [6, 7]

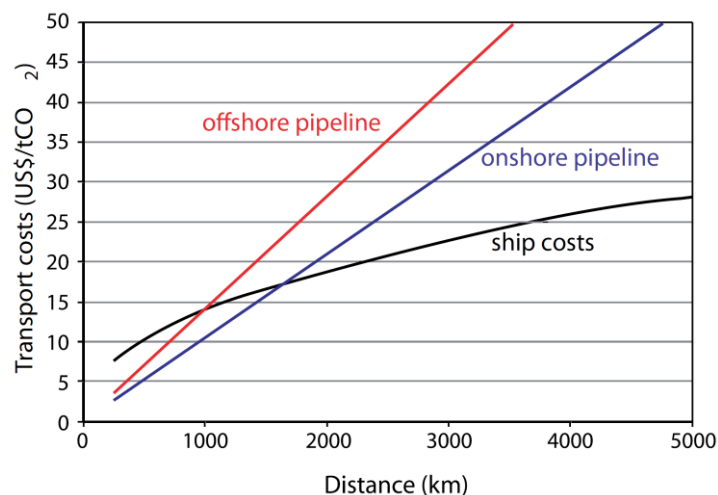


Figure 6: Comparison of transportation costs by ship and pipeline [6]

1.3.3 CO₂ storage

For storage of the captured and transported CO₂ three possibilities arise, which are described now briefly.

- Geological storage

Geological storage is realized in a depth of approximately 800 m below the earth's surface, whereby the CO₂ is injected in a dense form into a rock formation. If the CO₂ is trapped for several ten thousand years, due to chemical reactions with rock minerals, the CO₂ will be converted to solid carbonate minerals.

Due to the ambient pressure and temperature in this depth, CO₂ is kept in a liquid state with a density closely to those of crude oils. This leads to buoyancy forces which drive the CO₂ upward. Therefore, a well sealed cap rock above the storage site is important to keep the CO₂ trapped. Suitable geological formations could be depleted oil or gas reservoirs, deep saline formations, and unminable coal beds.

Potential risks can occur due to leakages, influencing human health in a local area or in large quantities the climate. [6, 7]

- Ocean storage

An alternative to geological storage is the storage of CO₂ in the sea. The captured CO₂ can be placed on ships and injected into the sea. At a depth of 3000 m below the sea level the density of the CO₂ will be higher than that of the sea water. The CO₂ sinks to the bottom of the sea and forms CO₂ lakes, where most of it would be isolated from the atmosphere for centuries. Since ocean storage would lead to ocean acidification, it is highly controversial to the influence on the deep sea ecosystem and a deployment seems rather unlikely. [6]

- Mineralization

Another option for CO₂ storage is mineralization by which the CO₂ is converted into solid inorganic carbonates. Chemical reactions between CO₂ and alkaline or alkaline earth oxides (e.g. MgO and CaO) produce silica and carbonates that are stable over a long time scale. The storage of these compounds would be possible at low risks and little need of monitoring. The major disadvantage is the low energy efficiency which would be 30 to 50 % of the capture plant output. [6]

1.4 Chemical looping combustion

Chemical looping combustion (CLC) is a carbon capture technology which belongs to the unmixed combustion technologies. The main principle of CLC is that fuel and air are never mixed. Therefore, the combustion reaction is divided into two steps which take place in two different reaction zones (air reactor and fuel reactor). For the transport of oxygen from one reaction zone to the other an oxygen carrier material is used. Typical oxygen carriers are metal oxides based on Ni, Cu, Fe and Mn. An illustration of the principle of CLC is shown in Figure 7.

In the air reactor (AR) the oxygen carrier gets oxidized and transports the oxygen to the fuel reactor (FR). There the oxygen carrier is reduced, while the fuel is ideally fully oxidized to CO_2 and H_2O . Afterwards, the oxygen carrier is returned to the AR and oxidized again.

Due to the fact that fuel and air are never mixed, the exhaust gas of the FR consists only of CO_2 and H_2O . Only in case of an incomplete combustion the FR exhaust stream can also contain uncombusted gas species like CO and H_2 . The H_2O leaving the FR with the exhaust stream can then be separated from the CO_2 in a condenser. The AR exhaust stream consists of oxygen depleted air and can be released to the atmosphere.

Due to the avoidance of the energy intensive gas-gas separation steps, CLC is one of the most energy efficient processes for carbon capture. [7]

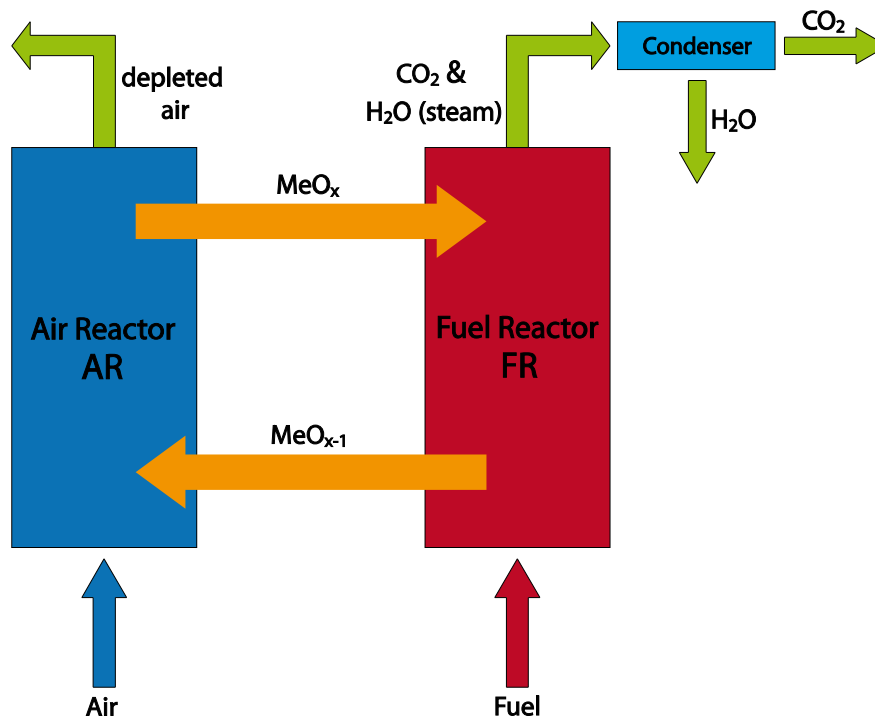
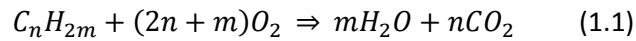


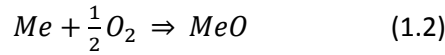
Figure 7: Principal of a CLC process

Chemical reactions

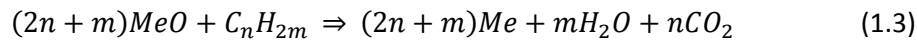
In a CLC process, the combustion reaction (1.1) takes place in two separate reactors (AR and FR).



In the AR, the oxygen carrier metal gets oxidized. This reaction is always exothermic and can be gathered from equation 1.2.



In the FR, the oxygen carrier metal gets reduced, while the fuel is oxidized. This reaction can be endothermic or exothermic, depending on the used oxygen carrier. However, according to the energy conservation the sum of the energy released in the two reactions has to be equal to the conventional combustion. The chemical reaction of the FR is given in equation 1.3. [8]



The heat of the exhaust gas streams leaving the AR and FR can then be used for power production, for example in a steam turbine process. Until now, CLC has been demonstrated using gaseous fuels up to a fuel power of 120 kW. Due to its huge potential, a lot effort is put in CLC for solid fuels. CLC reactor systems are typically designed as fluidized beds, where the bed material is used as oxygen carrier circulating between the two reactors.

1.5 Challenges in the application of CLC to solid fuels

As mentioned in the last chapter, the CLC concept for gaseous fuels has been demonstrated at relevant operating conditions. However, the progress in developing CLC for the direct use of solid fuels is not as far as for gaseous fuels. [9]

In CLC, the solid fuel has to be decomposed into its gaseous compounds. Thereby, it showed that devolatilization is rather fast, while the gasification of the char proceeds considerably slower and represents the limiting step. Further, after decomposition the gaseous compounds need sufficient contact with the oxygen carrier as well as enough time to react with the provided oxygen. Furthermore, the residual ash and inert contents need to be separated from the oxygen carrier. [9]

The Novel DUAL FLUID reactor concept, which will be described in chapter 2.8, represents a possibility for direct biomass CLC. [9]

1.6 Motivation and objectives

The aim of this work was to evaluate the potential of the novel Dual Fluid reactor concept for the application to CLC of solid fuels. This new reactor concept uses simple geometrical constrictions inside the FR and will be introduced in chapter 2.8. To evaluate the fluid dynamic behavior of a reactor with such constrictions a cold flow model (CFM) is used for the tests based on the design for a pilot plant for solid fuels.

Following main objectives have been of interest:

- The general operation of the novel DUAL Fluid reactor concept
- To investigate the possibility of the novel Dual Fluid reactor concept to increase the solid fraction over the height of the FR.
- To identify the mechanisms which influence the operating range of the fluidized bed system.

To obtain an insight into the fluid dynamic behavior of the CFM, the pressure at 40 positions as well as solid circulation rates are measured. To investigate the solid distribution and solid fraction between the constrictions, three pressure measurement ports are placed inside one constriction and eight more between two constrictions. In addition, a mathematical model, based on the conservation of mass and equation of motion, is developed to simulate the influence of the constrictions.

2. Theoretical Background

2.4 Fluid dynamic background

2.4.1 Pressure changes in stationary flowing and incompressible fluids

In principal there are three reasons for a change of pressure in a stationary flowing and incompressible fluid. These are

- frictional losses,
- changes of the velocity, and
- gravitational influence.

This is apparent, for example, at the extended Bernoulli equation (2.10) which can be derived from the conservation of energy for a stationary and incompressible flowing fluid. This equation is compared to the regular Bernoulli equation expanded by a frictional loss term ($\Delta p_{1/2}$).

$$p_1 + \rho_f * g * h_1 + \rho_f * \frac{u_1^2}{2} - \Delta p_{1/2} = p_2 + \rho_f * g * h_2 + \rho_f * \frac{u_2^2}{2} \quad (2.1)$$

This equation can also be expressed in the following form, using the definitions of static pressure (p), dynamic pressure (p_{dyn}) and total pressure (p_{tot}).

$$p_{tot/1} + \rho_f * g * h_1 - \Delta p_{1/2} = p_{tot/2} + \rho_f * g * h_2 \quad (2.2)$$

$$p_{tot} = p + p_{dyn} \quad (2.3)$$

The above mentioned and used definitions for the pressure of a stationary flowing and incompressible fluid, which are static pressure (p), dynamic pressure (p_{dyn}) and total pressure (p_{tot}) will now be described more detailed. It is important to note, that dynamic pressure and total pressure are not pressures in the usual sense and the term pressure alone refers to static pressure. [10, 11]

The measuring methods for the different pressures in a flowing fluid are illustrated in Figure 8.

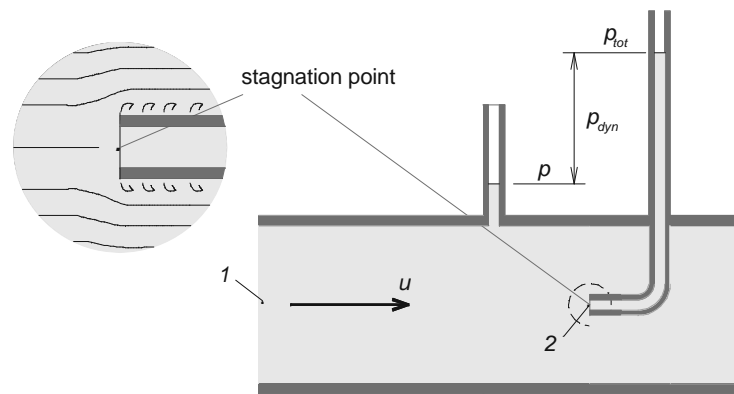


Figure 8: Measuring methods for pressure [10]

- Static pressure

This pressure is typically meant when talking about the pressure in a fluid. If this pressure should be demonstrative distinguished from other pressure definitions it is called static pressure. The static pressure is defined as the pressure which a fluid exerts on a body moving with the fluid. Therefore, it equals to the pressure which a fluid exerts on a wall running parallel to the fluid flow. It is typically measured by little holes which are placed perpendicular to the fluid flow. [10, 11]

- Dynamic pressure

The dynamic pressure is equal to the kinetic energy per unit volume of a fluid particle and is defined by equation 2.4. It can be measured as the differential pressure between total pressure and static pressure. [10, 11]

$$p_{dyn} = \rho_f * \frac{u^2}{2} \quad (2.4)$$

- Total pressure

The total pressure (2.3) is defined as the sum of the static pressure and the dynamic pressure. It can be measured at a point at which the fluid velocity reaches zero. Such a point is called a stagnation point. [10, 11]

Pressure changes due to changes of the velocity

As can be gathered from equation 2.1, a variation of the fluid velocity has to be compensated by a change of the static pressure. Thereby, the static pressure increases with decreasing velocity. In other words, the dynamic pressure is converted into static pressure or vice versa. In a stationary flow of an incompressible fluid, the velocity depends on the cross sectional area. [10, 11]

A change of the cross sectional area can be produced by

- construction related constrictions or enlargements, and
- solid bodies such as particles inside the fluid.

Pressure changes due to frictional losses

Friction leads to a resistance which acts against the fluid flow. As the dynamic pressure in a stationary flow cannot change due to the conservation of mass, this has to be compensated by a reduction of the static pressure. This pressure change is irreversible, in contrast to a velocity induced pressure change. [10, 12]

Friction in a fluid flow can occur

- between fluid and wall,
- inside the fluid, and
- between fluid and solid bodies.

Pressure changes due to gravitational influence

As can be gathered from equation 2.1, the static pressure depends on the gravitational height of the fluid. Therefore, the static pressure decreases with increasing height. This pressure change is, like for velocity induced pressure changes, reversible. For gases the gravitational influence on the pressure is relatively small due to their low density. [10, 11]

Pressure change due to inertial effects

A special combination of a velocity and friction caused pressure change can be recognized at flow contractions and enlargements due to inertial effects. The influence of such a combined pressure change is depicted schematically in Figure 9. [10, 12]



Figure 9: Streamlines of flow due to inertial effects

At a sharp or sudden contraction or enlargement, due to inertial effects, the streamlines of the fluid get bend. This leads to a reduced effective cross sectional area (A_{eff}) compared to the cross sectional area of the tube and moreover to a lower pressure than for the real cross sectional area. Further, recirculation regions occur near the contraction or enlargement at which due to inner friction of the fluid energy is dissipated. This dissipation caused by the recirculation means that not all the dynamic pressure is converted into static pressure or vice-versa. [10, 12]

2.4.2 Fluid dynamic dimensionless numbers

Dimensionless numbers are important in tests with scaled models to ensure similarity between original and scaled model. If all dimensionless numbers in two processes are the same they show similar behavior. They arise from dimensional analysis of mathematical models of physical processes. For example, the Reynolds number and the Froude number are obtained by non-dimensionalization of the Navier Stokes equation which describes the behavior of Newtonian fluids. [12, 13] The most important for this thesis are:

Reynolds number

The Reynolds number (2.5) gives the ratio of inertial forces to the viscous forces.

$$Re = \frac{\text{inertial forces}}{\text{viscous forces}} = \frac{\rho_f * u * d}{\mu} \quad (2.5)$$

Archimedes number

The Archimedes number (2.6) is defined as the ratio of gravitational forces to viscous forces.

$$Ar = \frac{\text{gravitational forces}}{\text{viscous forces}} = \frac{\rho_f * d^3 * (\rho_s - \rho_f) * g}{\mu^2} \quad (2.6)$$

Froude number

The Froude number (2.7) gives the ratio of inertial forces to gravitational forces.

$$Fr = \frac{\text{inertial forces}}{\text{gravitational forces}} = \frac{u}{\sqrt{g * d}} \quad (2.7)$$

2.5 Fluidized bed technology

A fluidized bed is achieved when a fluid flows through a bulk of solid particles, to cause the particles to behave like a fluid. This is achieved by compensating the gravitational force of the particles by the frictional force between particles and fluid, so that the particles have the ability to move freely under gravitational influence.

2.5.1 Particles

The particles in fluidized beds can be described by

- diameter (d),
- sphericity (ψ),
- particle density (ρ_p)

or in bulk by their

- bulk density (ρ_B),
- porosity (ε) and
- particle size distribution.

Further they can be divided into four groups which were defined by Geldart. [17]

Diameter and sphericity

As the form of the particles deviates generally from a sphere, different diameters are used to describe the size of a particle. [14]

Symbol	Name	Description
d_p	Sieve diameter	Side length of a square through which the particle can pass.
d_v	Volume diameter	Diameter of a sphere which has the same volume as the particle.
d_s	Surface diameter	Diameter of a sphere which has the same surface as the particle.
d_{sv}	Sauter diameter	Diameter of a sphere with the same surface/volume ratio as the particle.

The sphericity describes the deviation of a particle compared to a sphere and is defined by equation 2.8. [15]

$$\psi = \left(\frac{d_v}{d_s}\right)^2 \quad (2.8)$$

Particle density, bulk density and porosity

The particle density (2.9) is calculated using the particle volume including all inter particle void volumes and internal pore volumes. Therefore, the particle density is lower than the material density. [14]

$$\rho_P = \frac{M_P}{V_P} \quad (2.9)$$

The bulk density (2.10) is calculated with the mass of a large amount of particles and the volume they occupy. Therefore, the bulk density is lower than the particle density. Further, it is determined without any compaction of the particles. [14]

$$\rho_B = \frac{M}{V_B} \quad (2.10)$$

The porosity (2.11) is a dimensionless number and gives the interparticle volume fraction of the total volume. [14]

$$\varepsilon = 1 - \frac{\rho_B}{\rho_P} \quad (2.11)$$

Particle size distribution and mean diameter

The particles in a fluidized bed normally do not have the same diameter. The particle size distribution shows the percentage by weight of the different diameters and is used to calculate a mean diameter which represents the particle size for all particles. [16]

In a sieve analysis the mean diameter can be calculated by equation 2.12.

$$d_p = \frac{1}{\sum_{i=0}^i \frac{x_i}{d_{pi}}} \quad (2.12)$$

The mean Sauter diameter (2.13), which is usually used to characterize a bed material can be calculated by multiplication of the mean sieve diameter by the sphericity.

$$d_{sv} = \psi * d_p \quad (2.13)$$

Geldart groups

In 1973, Geldart proposed the partition of fluidized bed materials based on their density difference to the fluidizing medium and mean Sauter diameter into four groups. The individual Geldart groups can be visualized in a diagram, which is depicted in Figure 10.

Group C “cohesive”

The powders which belong to this group are cohesive and difficult to fluidize. They tend to clump and build channels in which the particles lift as a plug. The reason therefore is that in this group the attraction forces predominate the drag forces. This is in general the reason for very small particles, electrostatic charges or sticky material (e.g. flour, starch). [17, 18]

Group A “aeratable”

These powders show a considerably expansion of the bed and a delayed bubbling point. The bubbles are rather small, split and coalesce very frequently. They show a high solid mix even when only a few bubbles are present (e.g. milk powder, cracking catalyst). [17, 18]

Group B “sand like”

The particles show only a small bed expansion. Bubbling starts at the minimum fluidization velocity with large growing bubbles which burst at the surface. Noticeable solid mixing occurs only at increased bubbling. Very small attraction forces and cohesion between the particles. The most typical powder of this group is sand. [17, 18]

Group D “spoutable”

Particles of this group build very large bubbles which tend to spout. Also sticky materials can be fluidized because of the reduced particle to particle contacts which minimize agglomeration. Drag forces predominate the attraction forces (e.g. coffee beans, grain). [17, 18]

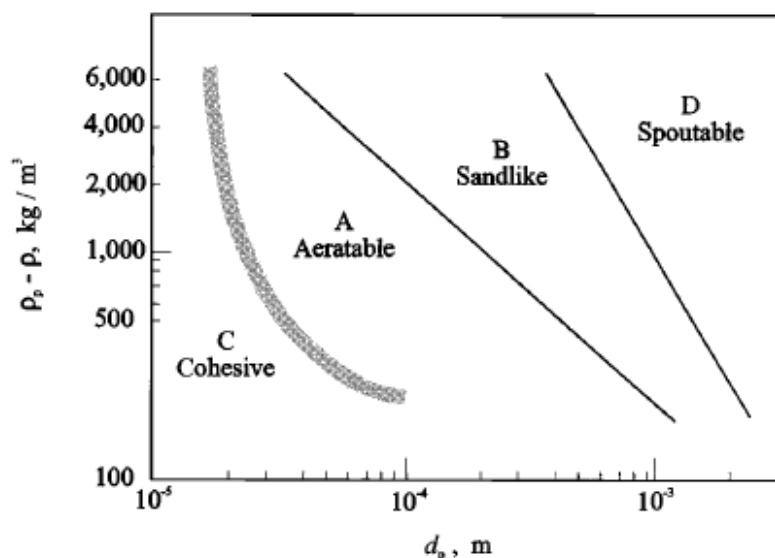


Figure 10: Geldart's classification of fluidized bed materials [14]

2.5.2 Fluid dynamic background

The fluidized bed regime is limited by two fluidization velocities. These are the minimum fluidization velocity (U_{mf}) and the terminal velocity (U_t). The minimum fluidization velocity limits the fluidized bed region to the fixed bed region while the terminal velocity describes the boundary to the pneumatic transport region.

Figure 5 shows the principle progression of the pressure drop from the fixed bed regime to the pneumatic conveying regime in a pressure – velocity diagram.

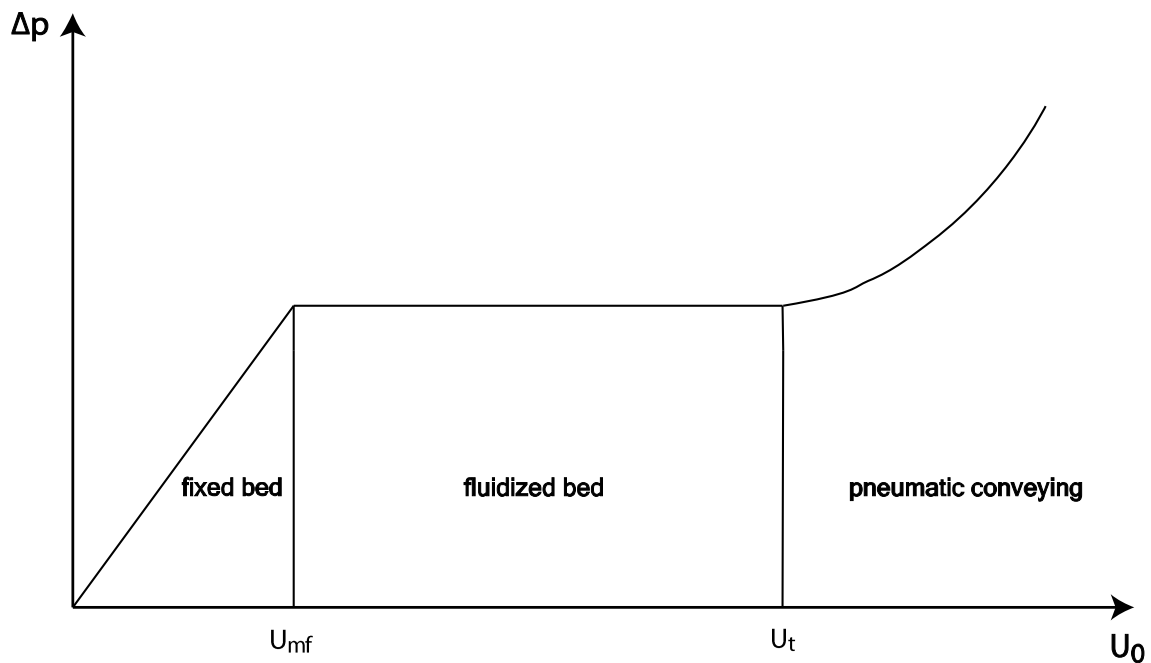


Figure 11: Progression of the pressure drop with superficial gas velocity

Pressure drop in the fixed bed

For the calculation of the pressure drop in a fixed bed the empirical found Ergun equation (2.14) has proved to be effective. The equation consists of a linear gas velocity dependent term accounting for the laminar flow and a quadratic term representing the turbulent flow. [14]

$$\frac{\Delta p}{H} = 150 * \frac{(1-\varepsilon)^2}{\varepsilon^3} * \frac{\mu * U_0}{d_{sv}^2} + 1,75 * \frac{1-\varepsilon}{\varepsilon^3} * \frac{\rho_f * U_0^2}{d_{sv}} \quad (2.14)$$

Pressure drop in the fluidized bed

The pressure drop in the fluidized bed (2.15) can be calculated via a balance of forces. From the minimum fluidization velocity until the terminal velocity the sum of the friction force and the buoyancy force are equal to the gravitational force of the particles. Therefore, the pressure drop

is independent from the fluidization velocity and keeps constant throughout the fluidized bed regime.

$$\Delta p = (1 - \epsilon_{mf}) * (\rho_p - \rho_f) * g \quad (2.15)$$

Pressure drop during pneumatic conveying

From the terminal velocity, the sum of the friction force and the buoyancy force exceeds the gravitational force of the particles which are carried with the gas stream and leave the reactor. For the pressure drop two possibilities arise. If the particles are returned into the reactor the pressure drop increases in comparison to the fluidized bed region. Contrary, if the particles are not returned into the reactor the pressure drop decreases with time, because of the decreasing number of particles which are inside the reactor. [14]

Minimum fluidization velocity

The minimum fluidization velocity (U_{mf}) (2.17) can be derived from the consideration that at this velocity the pressure drop in the fixed bed and the pressure drop in the fluidized bed have to be the same. Equating the two equations leads to the following general expression with the constants $C1$ and $C2$ which depend on the porosity at the minimum velocity.

$$Ar = C1 * Re_{U_{mf}} + C2 * Re_{U_{mf}}^2 \quad (2.16)$$

Different values can be found in the literature for these constants. For the expression of U_{mf} in equation 2.16 the values found by Wen and Yu for $C1$ and $C2$ were used. [14]

$$U_{mf} = \frac{\mu}{\rho_G * d_{sv}} * (\sqrt{33.7^2 + 0.0408 * Ar} - 33.7) \quad (2.17)$$

Terminal velocity

The terminal velocity (U_t) (2.18) can be derived from a force balance on a single particle under the assumption of spherical and un-accelerated particles. This leads to the following equation for U_t with the particle Reynolds number dependent drag coefficient (C_D). [14]

$$U_t = \sqrt{\frac{4}{3} * \frac{\rho_p - \rho_f}{\rho_f} * \frac{d_{sv} * g}{C_D}} \quad (2.18)$$

Figure 12 shows the change of C_D with increasing Re for a sphere.

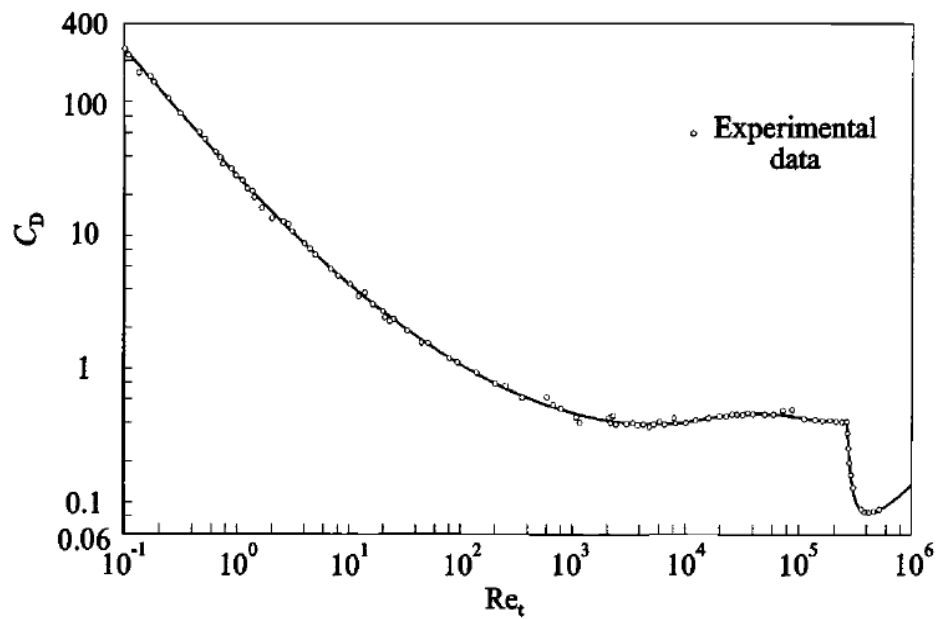


Figure 12: Development of the drag coefficient for a sphere with the Reynolds number [14]

The drag coefficient (C_D) for a sphere can be approximately calculated for three flow regions [19].

Laminar region ($Re < 0.2$):

$$C_D = \frac{24}{Re} \quad (2.19)$$

Transition region ($0.2 < Re < 1000$):

$$C_D = \frac{24}{Re} + \frac{4}{\sqrt{Re}} + 0,4 \quad (2.20)$$

Turbulent region ($Re > 1000$):

$$C_D = 0.43 \quad (2.21)$$

2.5.3 Fluidized bed regimes

Dependent on the superficial gas velocity in a container filled with bulk solids, different fluidization regimes appear, which are illustrated in Figure 13. These fluidization regimes can be characterized as follows:

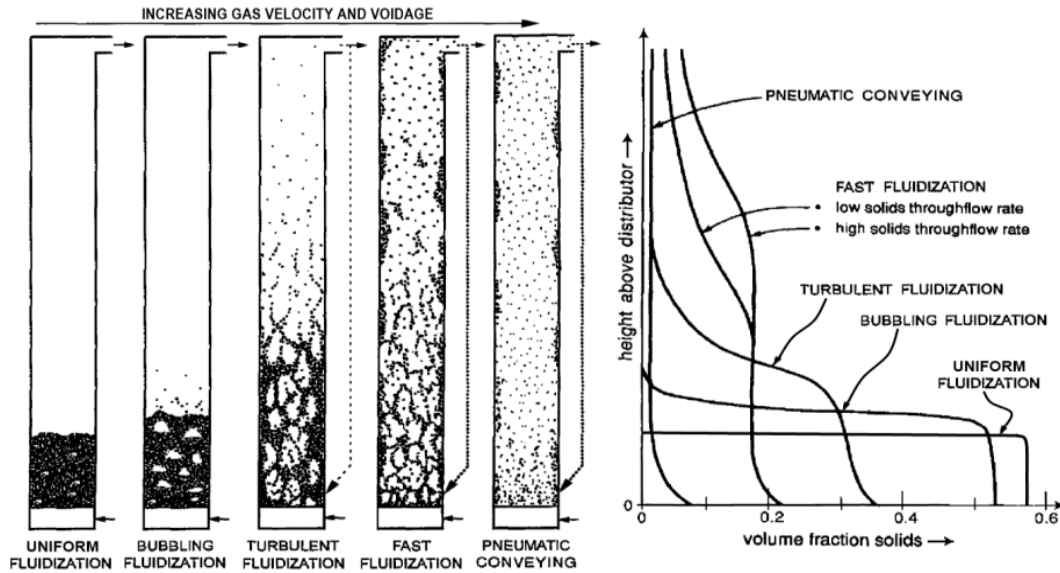


Figure 13: Fluidization regimes and corresponding typical solid distributions [21]

Fixed bed ($0 < U_0 < U_{mf}$)

For low superficial gas velocities the particles remain in a fixed position and do not move while the fluid flows through the interstices. This is called a fixed bed. If the superficial gas velocity is increased until it reaches U_{mf} (see equation 2.17), the bed expands uniformly and the porosity increases. At this point the frictional forces and the weight of the particles are in balance and the particles behave like a fluid. The bed is considered to be fluidized. [20]

Bubbling fluidization ($U_{mb} < U_0 < U_c$)

If the superficial gas velocity reaches the minimum bubbling velocity (U_{mb}) bubbles occur near the distributor which grow by coalescence and rise to the well defined upper bed surface. The minimum bubbling velocity can be evaluated by equation 2.22. [20]

$$U_{mb} = 33 * d_p * \left(\frac{\rho_g}{\mu_g}\right)^{0.1} \quad (2.22)$$

Turbulent fluidization ($U_c < U_0 < U_{se}$)

The turbulent regime is defined as the condition at which bubble coalescence and break-up reach a dynamic balance, which is the case, when the pressure fluctuations reach a maximum. The porosity further increases and particles build clusters which float up and down. First solid entrainment occurs and the upper bed surface is not clearly defined anymore. The transition from bubbling regime to turbulent regime occurs at the superficial gas velocity U_c , which can be estimated by its Reynolds number (Re_c) and equation 2.23. [20]

$$Re_c = 1.24 * Ar^{0.45} \quad (2 < Ar < 1 \times 10^8) \quad (2.23)$$

Fast fluidization ($U_0 > U_{se}$)

The fast fluidization regime is reached at the significant solid entrainment velocity (U_{se}) at which a significant entrainment of particles occurs. The upper bed surface has disappeared and clusters of particles are moving down near the wall. Though, the porosity in the lower region is notable lower than in the upper regions of the container. U_{se} can be evaluated with its calculated Reynolds number (Re_{se}) using equation 2.24. [20]

$$Re_{se} = 1.53 * Ar^{0.5} \quad (2 < Ar < 6 \times 10^6) \quad (2.24)$$

Pneumatic conveying

If the superficial velocity is still increased the porosity and solid entrainment further increase while the dense phase regions disappear. [20]

2.5.4 Regime maps

There are two important phase diagrams to describe the different fluidization regimes, which were proposed by Reh in 1961 and Grace in 1986. Both diagrams use dimensionless numbers to visualize the fluidization regimes, whereby a minimum of two dimensionless numbers is needed to determine an operating condition. It must be considered that the boundaries between the regime regions are not sharp and the transition is smooth. [20]

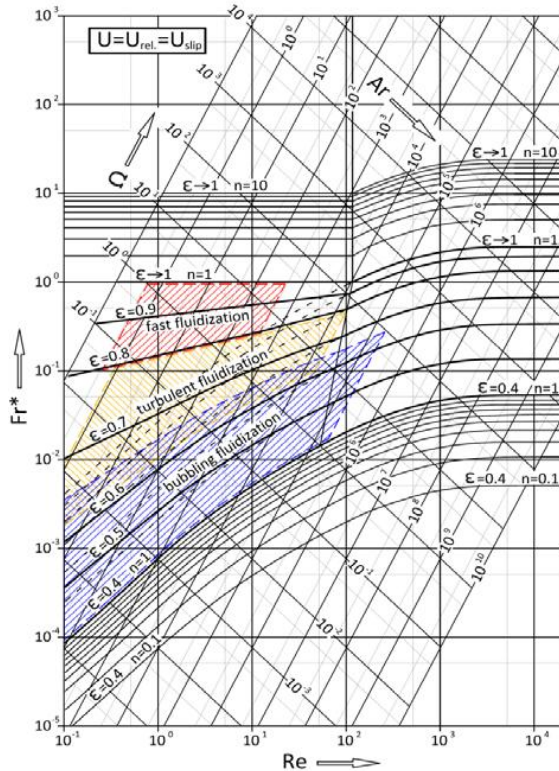


Figure 14: Regime map according to Reh [21]

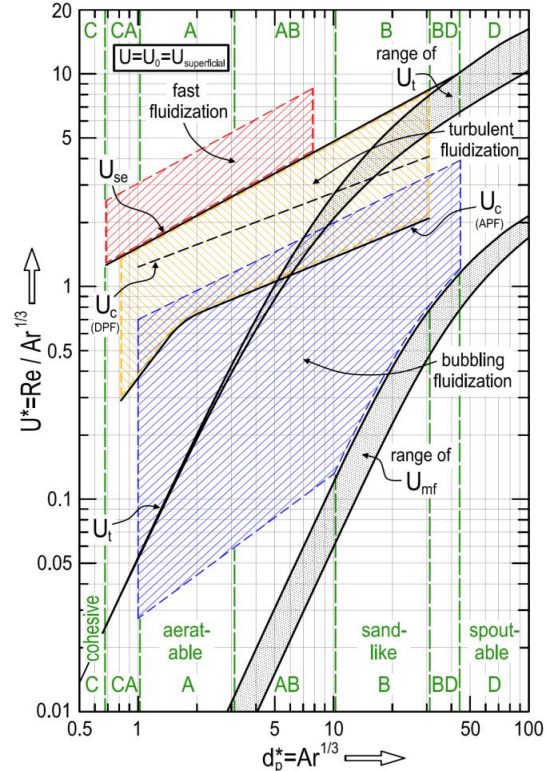


Figure 15: Regime map according to Grace [21]

Reh diagram

For this diagram, which is illustrated in Figure 14, Reh used the modified Froude number (Fr^*) (2.25) on the vertical axis and the Reynolds number on the horizontal axis, as well as two further axes which represent the Litaschenko number (Ω) (2.26) and the Archimedes number. Thereby, the Reynolds number is calculated using the slip velocity (U_{slip}) between gas and particles, which is usually not known. Particles which belong to Geldart group A and group B have a significant different behavior than single particles. Reh considered this effect by spreading up the fluidized bed porosity between $\epsilon = 0.4$ (representing U_{mf}) and $\epsilon = 1$. [20, 21]

$$Fr^* = \frac{3}{4} * \frac{U^2 * \rho_f}{g * d_p * (\rho_s - \rho_f)} \quad (2.25)$$

$$\Omega = \frac{3}{4} * \frac{U^3 * \rho_f^2}{g * \mu * (\rho_s - \rho_f)} \quad (2.26)$$

Grace diagram

Grace chose for his diagram, which is depicted in Figure 15, the dimensionless particle diameter (dp^*) (2.27) on the horizontal and the dimensionless velocity (U^*) (2.28) on the vertical axis. The dimensionless numbers in the Grace diagram are calculated with the superficial gas velocity, which is usually known, in contrast to the slip velocity used in the Reh diagram. To consider the

differing behavior of Geldart group A and B particles compared to single particles, Grace implemented a line at which a significant solid entrainment (U_{se}) occurs. Further, the horizontal axis can be used to visualize the particle classification according to Geldart. As the boundary between the bubbling regime and the turbulent regime can be determined with two methods which are the differential pressure fluctuations method (DPF) and the absolute pressure fluctuations method (APF) the diagram includes two boundary lines. [20, 21]

$$dp^* = Ar^{1/3} \quad (2.27)$$

$$U^* = \frac{Re}{Ar^{1/3}} \quad (2.28)$$

2.6 Cold flow modeling

Cold flow modeling is an important tool in processes design. It involves the construction of a scaled model of the proposed hot plant. The scaled model is an experimental model which is smaller than the original plant and operated at ambient temperature, but with the same hydrodynamic behavior. Such a model is usually operated at ambient conditions and fluidized with air. To ensure the hydrodynamic similarity between scale model and commercial plant Glicksman developed a set of scaling laws. [15, 22]

2.6.1 Scaling relationships by Glicksman

Glicksman derived the scaling laws from the valuation that the scaled model has to follow the same equations and boundary conditions than the hot plant. Therefore he non-dimensionalized the governing equations which are the conservation of mass (2.29 and 2.30) and the equation of motion (2.31 and 2.32) for fluid and solid. For these equations Glicksman considered the fluid and the particulate phases as a continuum. Further, he assumed the fluid as incompressible and the inter particle forces (particle to particle forces, electrostatic forces) are neglected. To ensure similar behavior, all of the non-dimensionalized parameters in the equations and boundary conditions have to be the same. [22]

Conservation of mass

The equations 2.29 and 2.30 show the conservations of mass for the fluid and solid phase, respectively.

$$\text{div}(\varepsilon * u) = 0 \quad (2.29)$$

$$\text{div}((1 - \varepsilon) * v) = 0 \quad (2.30)$$

Equations of motion

In equation 2.31 the equation of motion (expressed as eulerian form) for the fluid phase is shown while equation 2.32 represents the solid phase.

$$\rho_f * \varepsilon * \left(\frac{\partial u}{\partial t} + u * \text{grad}(u) \right) + \rho_f * g * \varepsilon + \text{grad}(p) + \beta * (u - v) = 0 \quad (2.31)$$

$$\rho_s * (1 - \varepsilon) * \left(\frac{\partial v}{\partial t} + v * \text{grad}(v) \right) + \rho_s * g * (1 - \varepsilon) - \beta * (u - v) = 0 \quad (2.32)$$

These equations can also be expressed in the following form: With F_F representing the friction term while a_f and a_s are used for the particular acceleration terms.

$$\rho_f * \varepsilon * a_f + \rho_f * g * \varepsilon + \text{grad}(p) + F_F = 0 \quad (2.33)$$

$$\rho_s * (1 - \varepsilon) * a_s + \rho_s * g * (1 - \varepsilon) - F_F = 0 \quad (2.34)$$

Boundary conditions

The boundary conditions at the wall are shown in the equations 2.35 for the fluid and 2.36 for the solid.

$$u = 0 \quad (2.35)$$

$$v_n = 0 \quad (2.36)$$

Further there are boundary conditions at the bottom which are shown in equation 2.37 for the fluid and 2.38 for the solid.

$$u = \frac{U_0}{\Delta} \quad (2.37)$$

$$v_n = \frac{G_s}{\rho_s * (1 - \varepsilon)} \quad (2.38)$$

From these equations (2.29 to 2.38) the following set of non-dimensional parameters can be identified and is referred to as the full set of scaling relationships.

Table 1: Full set of scaling relationships

Dimensionless number	Equation
Re	$\frac{\rho_f * U_0 * d_p}{\mu}$
Ar	$\frac{\rho_f * d_p^3 * (\rho_s - \rho_f) * g}{\mu^2}$
Fr	$\frac{U_0}{\sqrt{g * d_p}}$
Ratio of fluid to solid density	$\frac{\rho_s}{\rho_f}$
Ratio of bed to particle diameter	$\frac{D}{d_p}$
Ratio of bed height to particle diameter	$\frac{H}{d_p}$
Sphericity	ψ
Particle distribution	-
Dimensionless solid circulation rate	$\frac{G_s}{\rho_s * U_0}$

2.7 Calculation of the solid fraction in a fluidized bed

Under certain assumptions, it is possible to calculate the mean solid fraction (ϵ_m) via a pressure profile. Therefore, the equations of motion for the fluid and solid phase from chapter 2.6.1 are integrated over the height and are used as a conservation of energy criterion. This leads to the equations 2.39 and 2.40. Each of these equations consists of a dissipation term, kinetic energy term, and potential energy term. Further, the equation of motion for the fluid phase includes a term representing the pressure energy. Then the following assumptions are made:

- $\rho_f \ll \rho_s$
- $v_{H_1} = v_{H_2}$
- steady state behavior
- friction occurs only between the solid particles and the fluid

As for the assumption that friction occurs only between particles and fluid, the friction terms have to be equal in both equations. Further, with the assumptions of the same solid velocity at both limits of integration (H_1 and H_2) the term representing the kinetic energy of the solid phase is canceled out. Due to the assumption that the fluid density can be neglected with respect to

the solid density the terms for the kinetic energy and the potential energy of the fluid phase are also canceled out.

$$\int_{H_1}^{H_2} F_F * dH = \int_{H_1}^{H_2} -grad(p) - \rho_f * \varepsilon * a_f - \rho_f * \varepsilon * g * dH \quad (2.39)$$

$$\int_{H_1}^{H_2} F_F * dH = \int_{H_1}^{H_2} \rho_s * (1 - \varepsilon) * a_s + \rho_s * (1 - \varepsilon) * g * dH \quad (2.40)$$

After application of the above mentioned assumptions, the two equations are reduced to equation 2.41, which can be used for the calculation of the mean solid fraction over the limits of integration.

$$(1 - \varepsilon_m) = \frac{p_{H_1} - p_{H_2}}{g * (H_2 - H_1) * \rho_s} \quad (2.41)$$

2.8 Novel DUAL FLUID reactor concept

The cold flow model (CFM) which was used for the experiments is based on the novel DUAL FLUID reactor concept, which is an advanced development of the Dual Circulating fluidized bed technology (DCFB). This new reactor concept which was developed at Vienna University of Technology with simple geometrical constrictions inside the FR constitutes an opportunity for CLC and is shown in Figure 16. [21, 23]

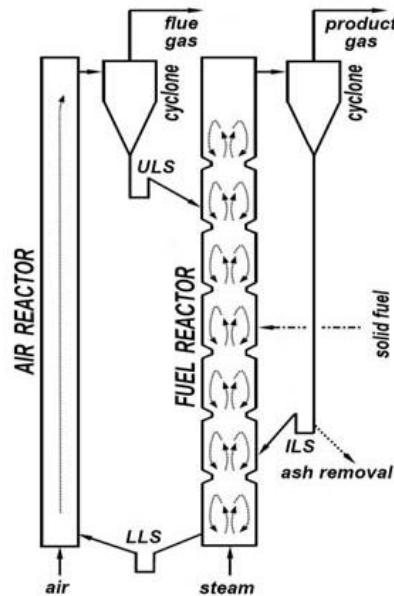


Figure 16: Novel DUAL FLUID reactor concept [21]

The particles rise in the AR (which is operated in the fast fluidization regime) from the bottom to the top where they leave the AR through a separator (e.g. cyclone) and the upper loop seal (ULS) into the FR. There the particles move against the gas flow (countercurrent flow) in the FR to the bottom, from which they are transported back into the AR via the lower loop seal (LLS). Particles which leave the FR at the top are separated from the fluid and returned via the internal loop seal

(ILS) into the FR. Further ULS and LLS, which separate FR and AR, act as a gas seal between the two reactors. Further, it is important to know, that for the fluidization of all loop seals as well as the fluidization of the FR steam is used to avoid the intrusion of nitrogen into the FR. [21]

The constrictions in the FR should achieve two functions. On the one side they should increase the solid fraction over the entire height of the fuel reactor. Further, it is expected that they cause local zones of turbulent fluidization regimes above each constriction, due to the increased superficial gas velocity in the constricted area. This combination of an increased solid fraction and zones of turbulent fluidization regimes after each constriction should ensure dense areas of particles as well as excellent mixing conditions. [21]

Figure 17 shows the assumed development of the pressure drop, pressure gradient and the particle volume fraction over the height of a FR with such constrictions as well as a picture during operation. Especially, from the picture it can be recognized that in such a reactor a good particle distribution over the entire height can be reached. [24]

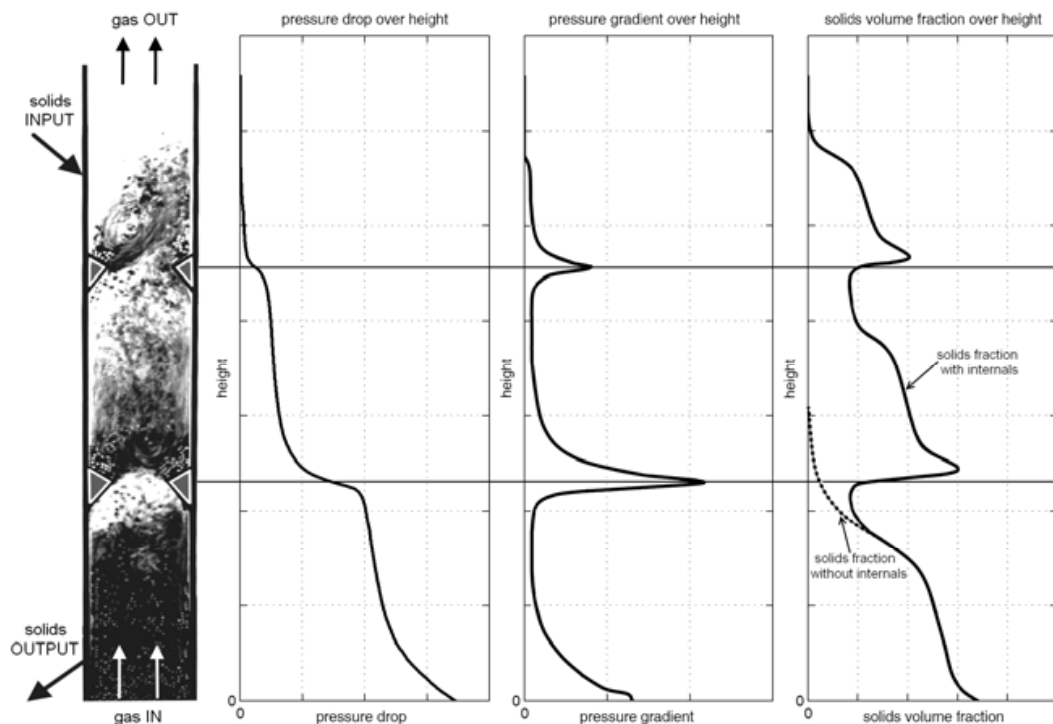


Figure 17: pressure drop, pressure gradient and particle volume fraction [24]

3. Experimental set-up

3.1 Description of the cold flow model

The experiments were performed at a CFM with a scaling factor of 1 : 2.5 from a CLC pilot plant. The plant follows the novel DUAL FLUID reactor concept as described in chapter 2.8.

As illustrated in the Figure 18 and Figure 20, the CFM generally consists of two reactors (AR and FR), five loop seals (LLS, ULS, ILS, AR CYL LS and FR CYL LS), two separators (AR SEP and FR SEP) as well as two cyclones (AR CYL and FR CYL). Further, to avoid an emission of fine dust a filter is placed at the outlet of each cyclone.

The AR and FR have a circular cross section with a diameter of 52 mm and 62 mm, respectively. Further, the FR with simple geometrical constrictions inside, has an aperture ratio (constricted area to free cross section area) of 28.75 %. While the ILS and the FR CYL and AR CYL are used to return particles into the AR or FR, the LLS and ULS allow the transportation of the particles from one reactor to the other. To reach a very high solids separating efficiency after each reactor, a separator followed by a cyclone, is placed.

As no fines were used during the measurements, the loop seals of the cyclones were not fluidized and the refeed connection into the FR and AR were sealed with a plug.

The model is built from transparent acrylic glass to enable visual observations of the fluid dynamic behavior. The entire model is grounded and a copper wire is wrapped around it to avoid electrostatic charging.

A schematic drawing of the CFM, with ground plan and elevation as well as the basic dimensions is given in Figure 20 and Figure 18, respectively. Further, in Figure 19, a detailed construction drawing of a constriction is illustrated.

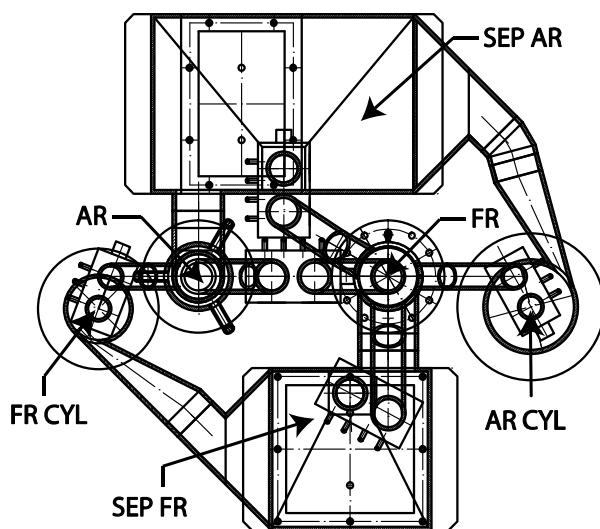


Figure 18: Elevation view of the CFM

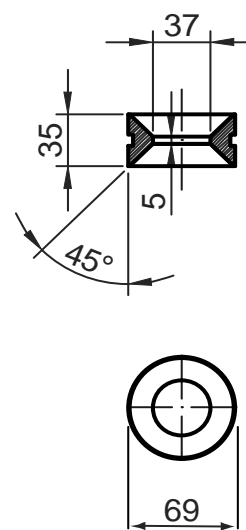


Figure 19: Drawing of a constriction (dimensions in mm)

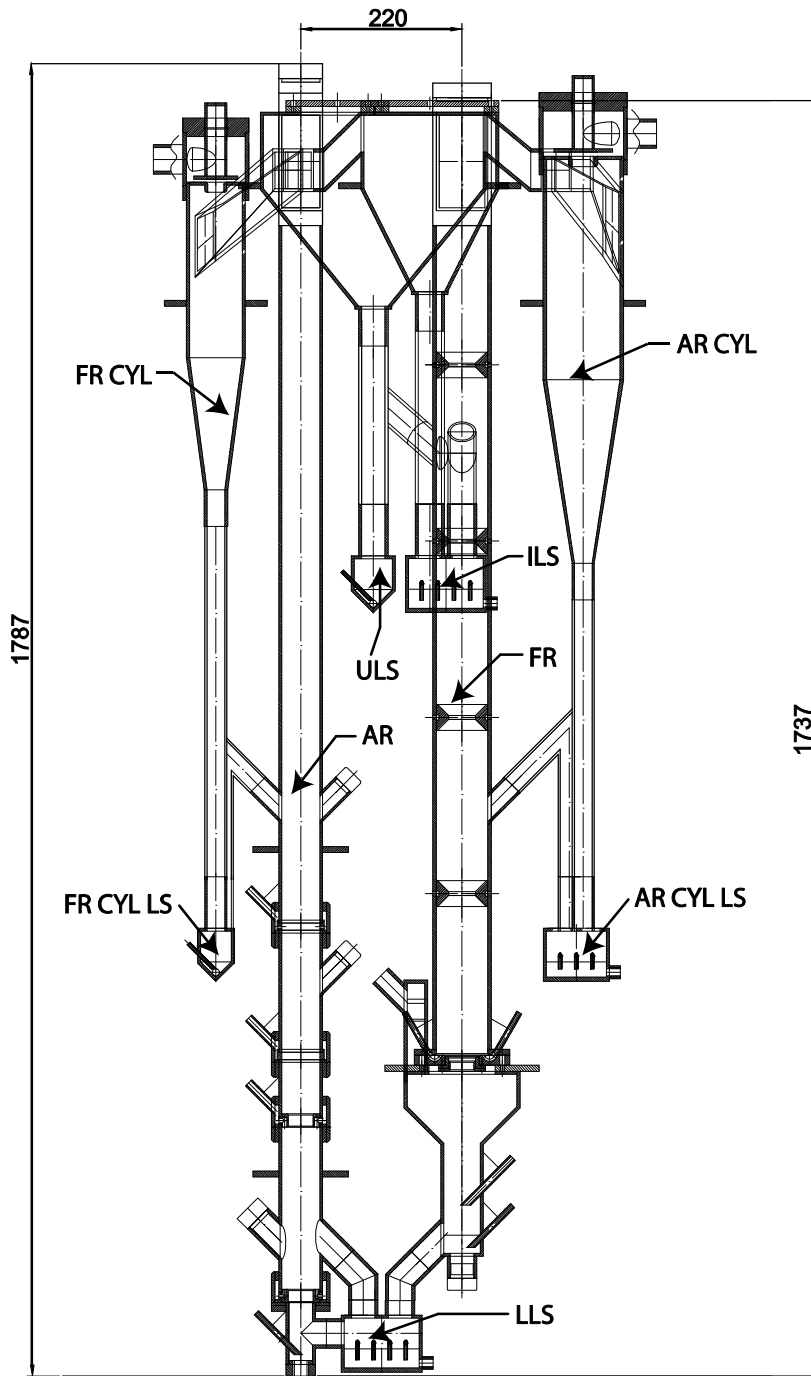


Figure 20: Ground plan of the CFM (dimensions in mm)

The CFM is fluidized with air and operated at ambient conditions. The fluidization of the AR (three stages) and the FR (three stages) can be supplied in stages, to provide a better control of the solid flows. During the measurements the FR III and AR BA fluidization were not used. A flow chart of the CFM is depicted in Figure 21.

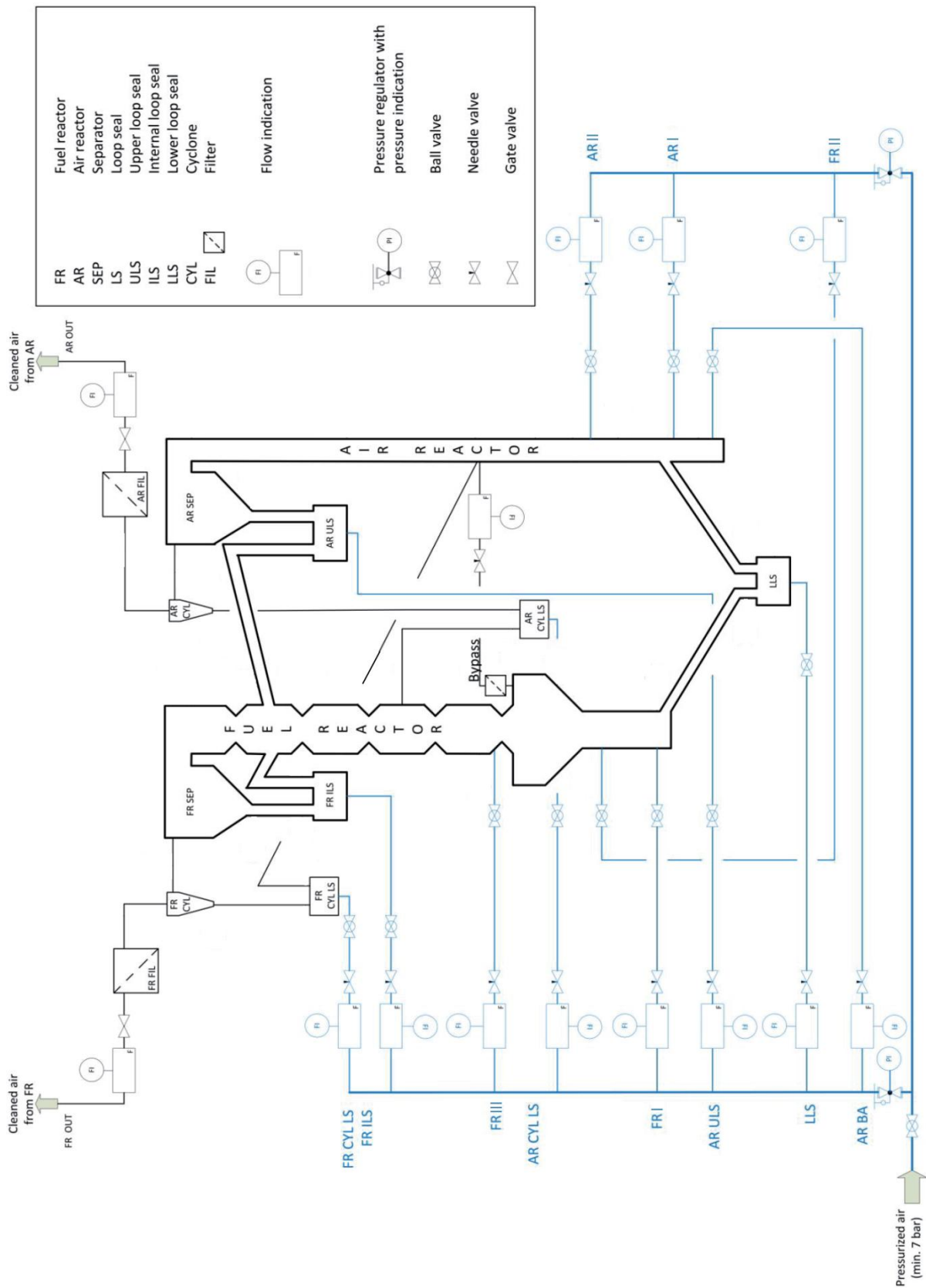


Figure 21: Flow chart of the CFM [26]

3.2 Bed material

In this section, the bed materials for the CLC pilot plant and the CFM are described. Further, the bed materials are assigned to the classification according to Geldart.

3.2.1 Classification according to Geldart

In the classification according to Geldart, both bed materials can be assigned to group B. The position of the bed materials in a diagram, which was suggested by Yang, for the illustration of the Geldart groups, is depicted in Figure 22.

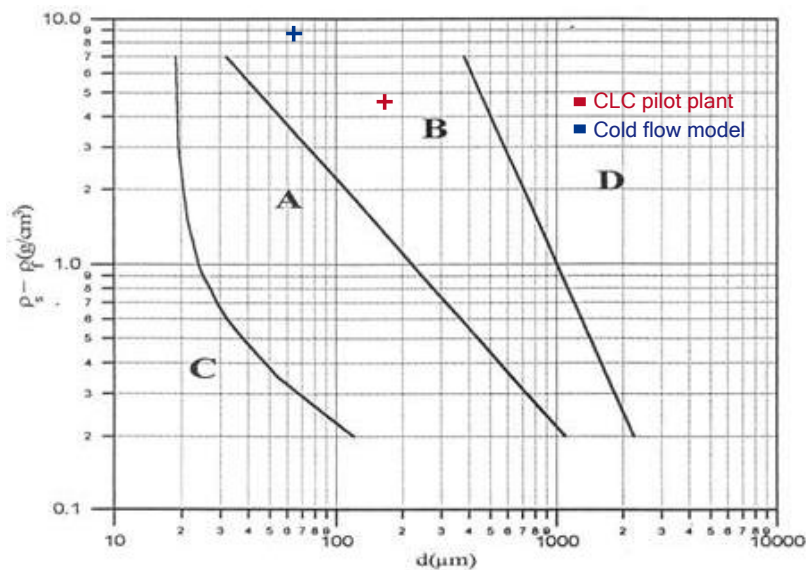


Figure 22: Classification of the bed materials according to Geldart

3.2.2 Bed material of the CLC pilot plant

The particles which are planned to be used in the CLC pilot plant are made of Ilmenite, a natural ore (Fe_2TiO_3), and have a globular shape. Their mean diameter of 170 μm was calculated by equation 2.5 using the particle size distribution. The particle size distribution was determined by a sieve analysis and is shown in Figure 23. The particle density is stated with 4700 kg/m³. The terminal velocity of the particles can be calculated using equation 2.16, with 1.32 m/s for the conditions inside the CLC pilot plant and 0.35 m/s at ambient conditions.

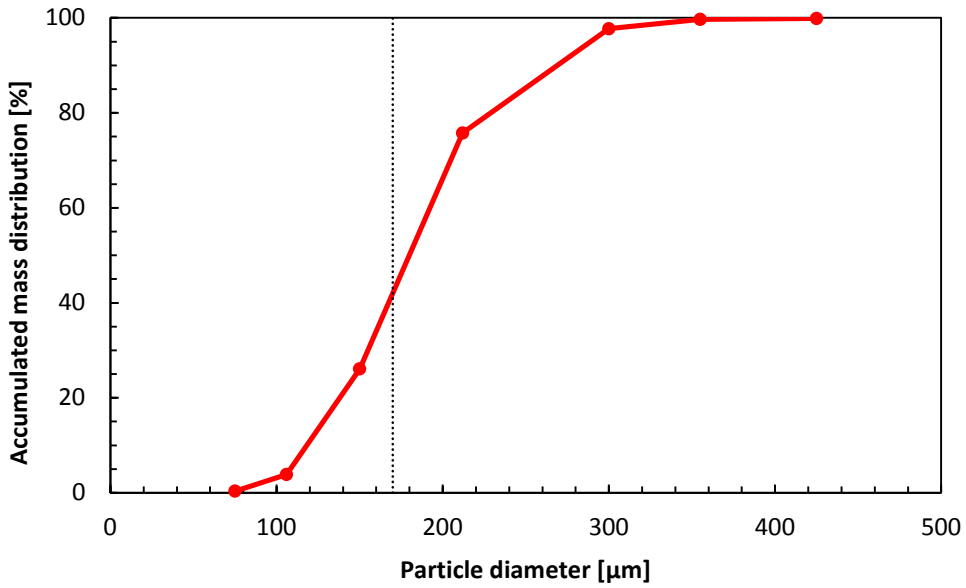


Figure 23: Particle size distribution Ilmenite

3.2.3 Bed material of the cold flow model

For the CFM, particles made of bronze with a nearly spherical shape were used. An image of the particles is shown in Figure 25. They have a mean diameter of 64 μm, which was calculated from their particle size distribution using equation 2.5. Their particle size distribution is depicted in Figure 24 and was determined by optical measurement using a microscope. The particles have a particle density of 8800 kg/m³ and a terminal velocity of 0.8 m/s. Their bulk density was determined with 5470 kg/m³ which correspond to a porosity of 38 %.

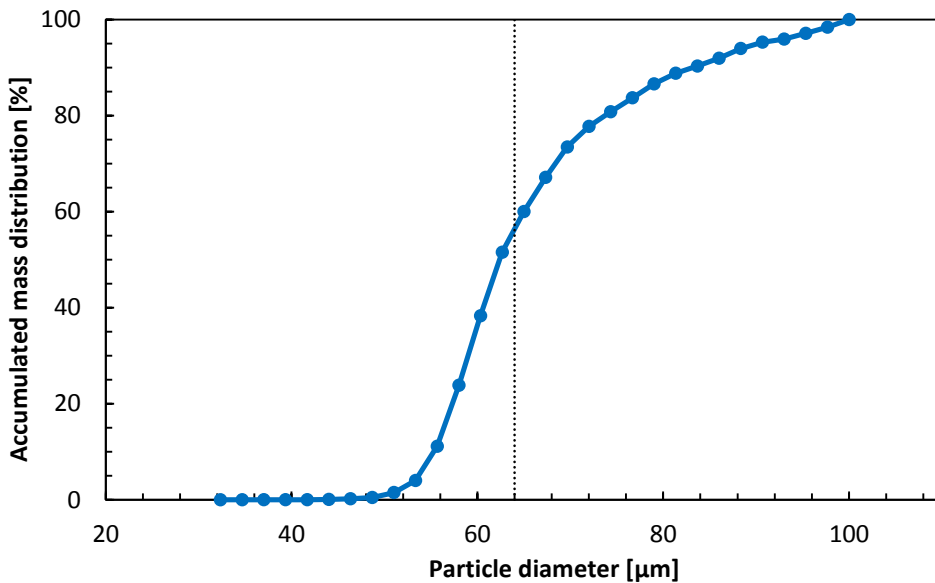


Figure 24: Particle size distribution Bronze

At the beginning of the experiments the CFM was filled with 21 kg of the bronze particles, while at the end 1.1 kg have been lost to the loop seals of the cyclones, as the refeed to the reactors

was disconnected. After opening the filters, which are placed after the cyclones, no accumulation of particles could be recognized.

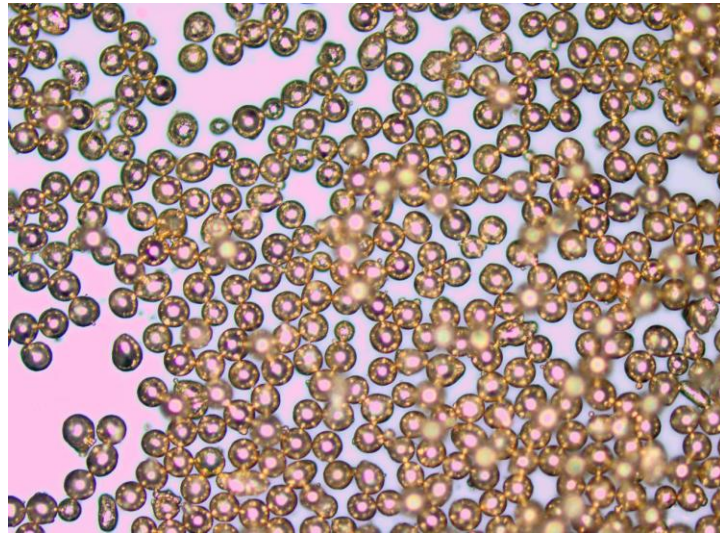


Figure 25: Image of bronze particles [26]

3.3 Application of scaling relationships

In Table 2 the relevant scaling parameters for scaling of the CFM, according to Glicksman, are depicted. These correspond to the standard operating point of the CLC pilot plant, with a fuel power of approximately 65 kW and the expected temperatures for the AR (1000 °C) and the FR (950 °C). Further, the index “H” refers to the CLC pilot plant, while the index “C” represents the CFM and the Index “con” is used for the constricted area.

Table 2: Scaling parameters for AR and FR

Parameter	Unit	AR _H	FR _H	FR _{H/con}	AR _C	FR _C	FR _{C/con}
ρ_f	[kg/m ³]	0.274	0.285	0.285	1.168	1.168	1.168
μ	[Pa s]	$5.06 \cdot 10^{-5}$	$4.61 \cdot 10^{-5}$	$4.61 \cdot 10^{-5}$	$1.87 \cdot 10^{-5}$	$1.87 \cdot 10^{-5}$	$1.87 \cdot 10^{-5}$
ρ_s	[kg/m ³]	4700	4700	4700	8800	8800	8800
d_p	[m]	$1.70 \cdot 10^{-4}$	$1.70 \cdot 10^{-4}$	$1.70 \cdot 10^{-4}$	$6.40 \cdot 10^{-5}$	$6.40 \cdot 10^{-5}$	$6.40 \cdot 10^{-5}$
U_0	[m/s]	8.12	2.3	9.21	3.3	0.96	3.86
D	[m]	0.125	0.156	0.078	0.052	0.069	0.037

The corresponding dimensionless numbers as well as their relative ratio from the CFM to the CLC pilot plant are given in Table 3 and Table 4 for the AR and FR, respectively. As there was no information available about the sphericity of the particles, which are used in the CLC demonstration plant and the CFM, it is not considered for the scaling. Further, as the relative ratio from the CFM to the CLC demonstration plant, of all dimensional numbers concerning the FR, are equal for the constricted and free cross section, they are shown for the whole FR in Table 4.

For a perfect similarity between the CLC pilot plant and the CFM, which is the case for a relative ratio of one, bronze particles with a mean diameter of 45 μm for the CFM would be required. However, previous investigations on the CFM showed, that the use of particles with a diameter of 45 μm would cause agglomerations, thus particles with a mean diameter of 64 μm were chosen. This affects mainly the Archimedes number, but as all dimensionless numbers are in one order of magnitude, a good similarity can be expected.

Table 3: Dimensionless numbers AR

Dimensionless number	AR_H	AR_C	Relative (hot/cold)
Re	7.46	13.20	0.57
Fr	39528.83	17304.30	2.28
Ar	24.17	75.77	0.32
D/d_p	730.23	812.50	0.90
ρ_s/ρ_f	17176.51	7531.39	2.28

Table 4: Dimensionless numbers FR

Dimensionless number	FR_H	FR_{H/con}	FR_C	FR_{C/con}	Relative (hot/cold)
Re	2.42	9.68	3.86	15.43	0.63
Fr	3177.67	50842.78	1479.76	23676.12	2.15
Ar	30.38	30.38	75.77	75.77	0.41
D/d_p	911.32	455.66	968.75	484.38	0.94
ρ_s/ρ_f	16501.94	16501.94	7531.39	7531.39	2.19

Figure 26 shows the position of the operating points for the AR and the FR (constricted and free cross section) of the CLC pilot plant and the CFM in the regime map according to Grace. For a perfect similarity the operating points for the CLC pilot plant and the CFM would have to overlap.

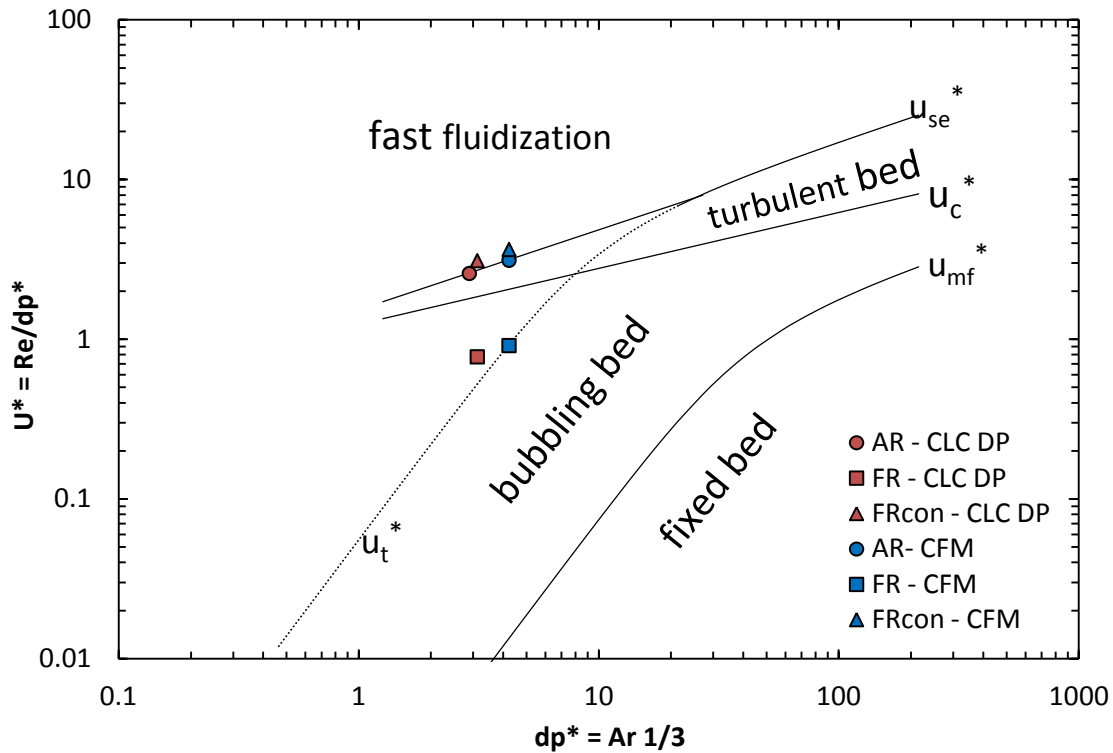


Figure 26: Position of the operating points of the CFM and the CLC demonstration plant in a regime map according to Grace

3.4 Measurement set-up

3.4.1 Volume-flow measurement

To adjust and measure the gas flow rates at the CFM, variable area meters (also called rotameter) are used. These devices are based on the drag force, which acts on a float, caused by a fluid flow through a tapered tube in vertical position. With increasing volume flow rates the drag force increases and the float rises until the tube is wide enough that drag force and gravity force are equal. Figure 27 shows the principal of such a device.

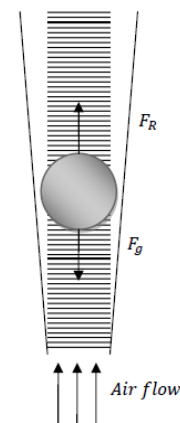


Figure 27: Principal of variable area meter

Table 5: Calibration values

Parameter	Value	Unit
T_0	20	$^{\circ}\text{C}$
p_0	6	bar
μ_0	18.29	Pa s
ρ_0	7.16	kg/m^3

As the drag coefficient depends on fluid density, viscosity, pressure and temperature every variable area meter is calibrated for specific values and a type of gas. Table 5 shows these calibration values of the used Krohne variable area meters and in Table 6 the operating ranges of are listed.

Table 6: Operating ranges of the variable area meter

Variable area meter	Type	Operating range [Nm ³ /h]
AR CYL LS	DK800/N	0.11 – 1.1
FR CYL LS	DK800/N	0.11 – 1.1
FR ILS	DK800/N	0.2 – 2
LLS	DK800/N	0.2 – 2
AR ULS	DK800/N	0.2 – 2
AR BA	DK800/N	0.2 – 2
FR 1	DK800/N	0.5 – 5
FR 2	VA40V/R	2 – 17
FR 3	DK800/N	0.5 – 5
AR 1	VA40V/R	2 – 20
AR 2	VA40V/R	2 – 20

3.4.2 Pressure measurement

For the pressure measurements small holes of 2 mm diameter were drilled into the acryl glass casing of the CFM. Above these holes an adapter with 1/8" internal screw thread was glued with the acryl glass casing. Further, the adapter was filled with cotton wool to prevent bed material to escape and to avoid damage to the pressure measurement system. Flexible tubes are used to connect the adapter to the pressure transmitter of the Type "Kalinsky DS-420". These pressure transmitters are using a piezoresistive cell to measure pressures relative to ambient conditions. To avoid errors due to temperature fluctuations all pressure transmitters are temperature compensated.

Pressure transmitters with four different pressure ranges were used (0 – 500 mbar, 0 – 250 mbar, 0 – 100 mbar and 0 – 50 mbar) and placed according to the expected pressure and required accuracy. The measuring accuracy of the used pressure transmitters is stated with 0.1 % of the final value. Further, to test the pressure measurement system for leaks, it was subjected to a constant pressure and checked for a pressure drop over time. Thereby, no leakage could be determined. An overview of the 40 measurement ports and their positions in the AR, FR, ILS, and ULS is given in Figure 28 to 30.

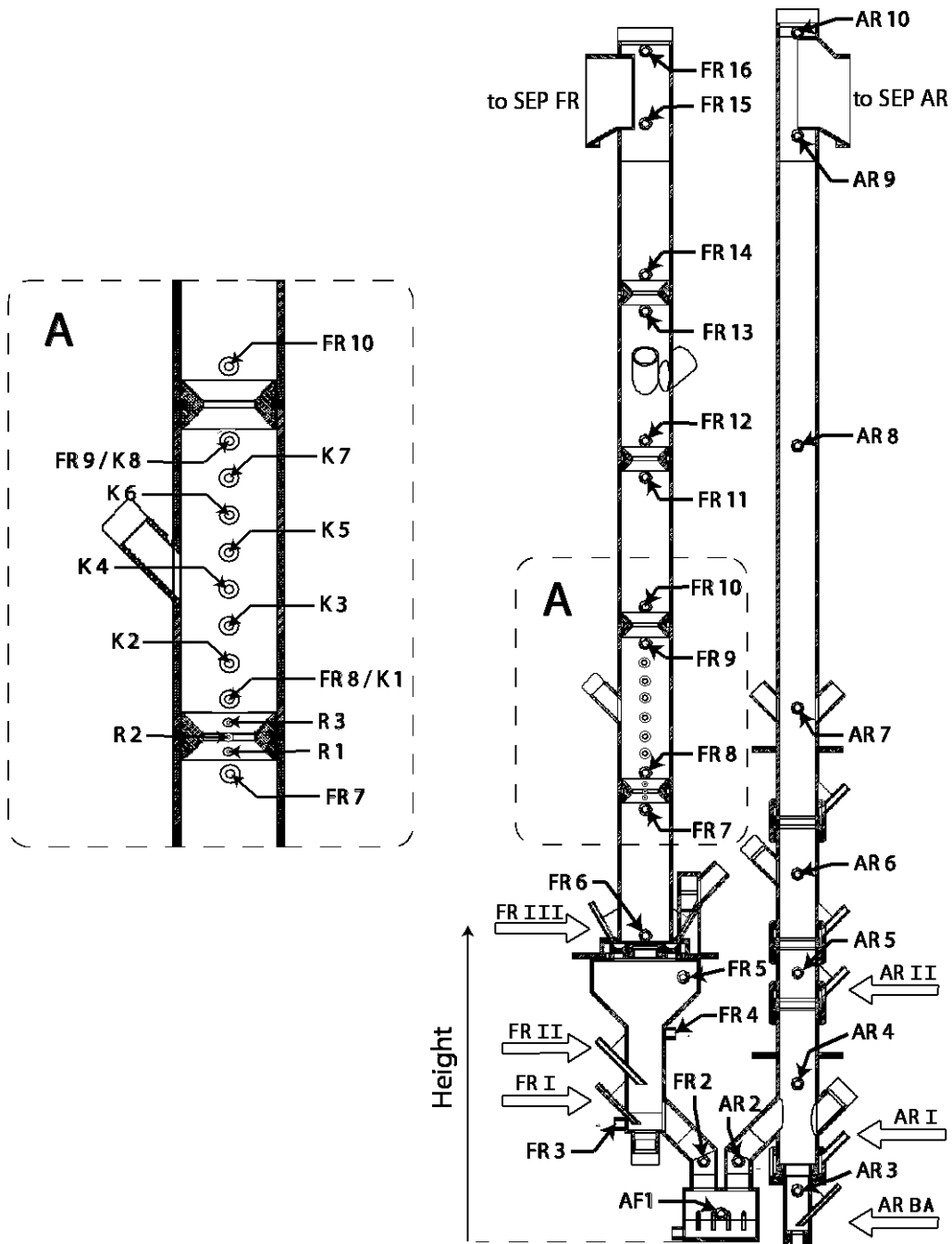


Figure 28: Pressure measurement ports in the AR and FR

The FR with its constrictions is divided into five individual sections, so called chambers. These are arranged, as described in Table 7. For determination of the pressure inside the chambers, chamber two is equipped with pressure measurement ports between the constrictions.

Table 7: Arrangement of the chambers in the FR

	From	To
Chamber 1	FR 5	FR 7
Chamber 2	FR 7	FR 9
Chamber 3	FR 9	FR 11
Chamber 4	FR 11	FR 13
Chamber 5	FR 13	FR 16

The height of the pressure measurement ports can be taken from Table 8, in which the bottom of LLS is used for the zero position.

Table 8: Height of the pressure measurement ports in the CFM

Pressure port	Height [cm]	Range [mbar]	Pressure port	Height [cm]	Range [mbar]
AF 1	4	0 - 500	FR 12	115.8	0 - 250
AR 2	11.7	0 - 500	FR 13	134.5	0 - 100
AR 3	7.4	0 - 500	FR 14	139.8	0 - 100
AR 4	22.8	0 - 250	FR 15	161.6	0 - 100
AR 5	38.9	0 - 250	FR 16	172.2	0 - 100
AR 6	53.2	0 - 250	R 1	64.35	0 - 100
AR 7	77.2	0 - 100	R 2	65.15	0 - 100
AR 8	115.1	0 - 100	R 3	65.95	0 - 100
AR 9	159.9	0 - 100	K 2	70.47	0 - 50
AR 10	174.8	0 - 100	K 3	73.14	0 - 50
FR 2	12.3	0 - 500	K 4	75.81	0 - 50
FR 3	17	0 - 250	K 5	78.48	0 - 50
FR 4	30.1	0 - 250	K 6	81.15	0 - 50
FR 5	38.3	0 - 250	K 7	83.82	0 - 50
FR 6	44.2	0 - 250	ILS 1	114.2	0 - 250
FR 7	62.5	0 - 250	ILS 2	114.2	0 - 250
FR 8 / K 1	67.8	0 - 50	ILS 3	145.8	0 - 250
FR 9 / K 8	86.5	0 - 50	ULS 1	114.2	0 - 250
FR 10	91.8	0 - 250	ULS 2	114.2	0 - 250
FR 11	110.5	0 - 250	ULS 3	143.7	0 - 100

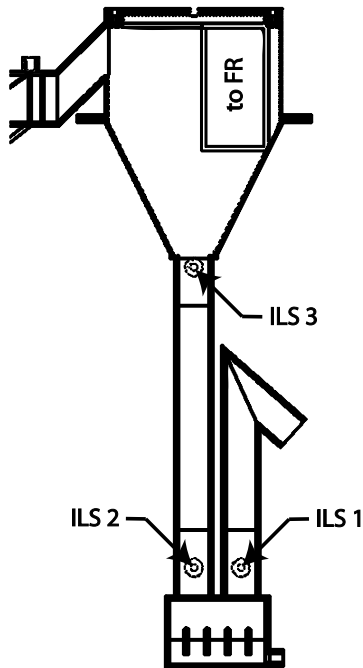


Figure 29: Pressure measurement ports at the ILS

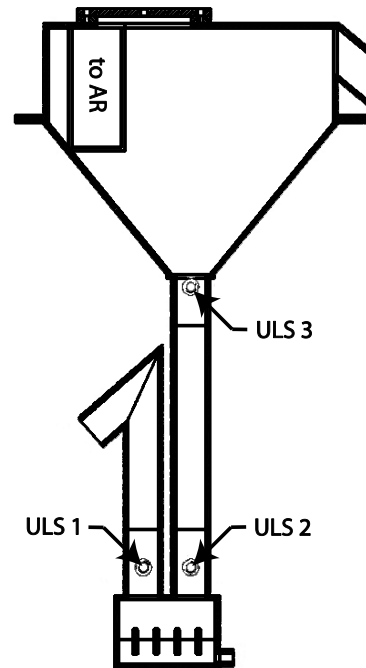


Figure 30: Pressure measurement ports at the ULS

3.4.3 Solids mass flow measurement

The following two mass flows, which are depicted in Figure 31, have been investigated for the CFM. These are the global circulation and the internal circulation.

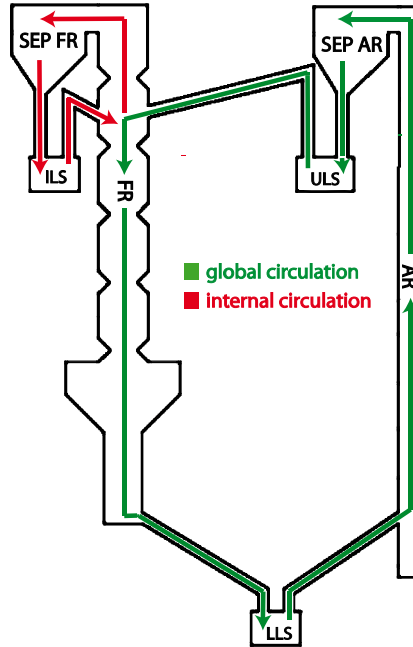


Figure 31: Global and internal circulation

Global circulation

The global circulation rate corresponds to the solid entrainment at the top of the AR and can be determined at the downcomer of the ULS. Therefore, the fluidization to the loop seal is stopped and the solid accumulation in the downcomer is recorded over time.

Internal circulation

The internal circulation rate is equal to the solid entrainment at the top of the FR and can therefore be determined at the downcomer of the ILS. To quantify the internal circulation, the fluidization of the ILS has to be stopped, while the solid accumulation in the downcomer is determined over time.

The global circulation and internal circulation can be calculated according to equation 3.1. Thereby, for the calculation of the global circulation the cross section area of the AR is used, while for the internal circulation that of the FR is used without constriction. The appropriate cross section areas for the downcomer and the riser are given in Table 9.

$$G_S = \frac{A_{downcomer} * \Delta H * \rho_B}{\Delta t * A_{riser}} \quad (3.1)$$

The time measurement was done by hand using a stop watch. To ensure appropriate measurements a minimum of 6 samples per operating point have been taken.

Table 9: Cross section areas

Riser	A_{riser}	A_{downcomer}	Unit
AR	2,10E-03	8,04E-04	m ²
FR	3,02E-02	8,04E-04	m ²

3.4.4 Data-acquisition

For the data acquisition of the pressure, two data acquisition devices of the type “NI PCIe 6323” as well as the software LabVIEW which is a graphical coding language, both from National Instruments, were used.

The data acquisition devices deliver a sample every 25 ms, which are averaged over one second in LabVIEW and stored in a text file (.txt). Afterwards, the samples are transferred to the spreadsheet software Microsoft Excel, where they are averaged over the whole acquisition time. Further, LabVIEW is used for the immediately visualization of the pressure profiles during experiments.

4. Mathematical model

The FR of the CFM, with its constricted areas, shows a totally different behavior than for classic designs without constrictions at some operating ranges. To develop an understanding for the mechanisms which lead to this behavior and to be able to evaluate the influence of these individual mechanisms, a mathematical model was designed.

The equations which are used for the description of the fluid and solid phases are similar on the ones Glicksman used for the scaling relationship in chapter 2.6.1. Therefore, the model is based on the conservation of mass and the equation of motions of the fluid and solid phases. The design of the model was chosen such that it is able to explain the basic mechanisms and is therefore subjected to certain limitations, which will be discussed later.

To keep the mathematical model simple, the following assumptions were made:

- Only one degree of freedom (one dimensional model)
- Steady state (time independent)
- Fluid and solid phases are continuums
- Incompressible fluid
- Friction only between solid particles and fluid
- No zero fluid velocity boundary condition at the wall
- Fluid and solid can move only in one direction (fluid up, solid down)

With the above mentioned assumptions, the following equations (4.1 to 4.5), for the fluid and solid phases can be derived. In contrast to the set of equations of Glicksman, the conservation of mass is given in a non differential form and all variables are only dependent on the degree of freedom, for which the height of the FR was chosen. As an initial condition a starting velocity of the particles must be defined. Further, to be able to consider the lower gas velocity at the wall, despite the missing boundary condition, the expression for the friction force was equipped with an additional factor denoted with s . In Figure 32 the degree of freedom and the directions of the fluid and solid flow as well as the initial condition are depicted.

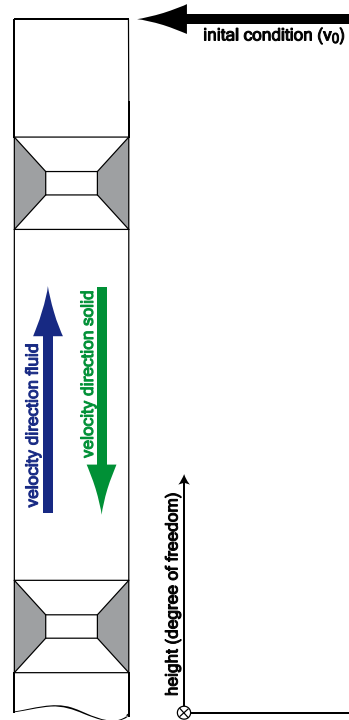


Figure 32: Schema of the mathematical model

Conservation of mass:

For a stable operation of the FR, the mass flow of the solid phase (\dot{m}_g) and the fluid phase (\dot{V}) must be constant over the height of the FR below the ULS inlet into the FR. Above this inlet the values of the mass flows change. Therefore, the equations are only valid from the inlet downwards.

$$\rho_s * (1 - \varepsilon) * v * A = -\dot{m}_g \quad (4.1)$$

$$\rho_f * \varepsilon * u * A = \dot{V} \quad (4.2)$$

Equation of motion:

The equations of motion for the solid phase (4.3) and the fluid phase (4.4) are used in the same form as described in chapter 2.6.1 for the scaling relationships of Glicksman. They consider only friction between fluid and solid and their variables are independent of time. Both equations consist of an acceleration term, a gravitational term and a friction term over which the two phases are coupled. The fluid phase includes a pressure gradient term in addition. The friction term is calculated via the relative velocity between particles and fluid. While the *factor s* is used to consider the lower gas velocity at the wall, the proportionality factor β (4.5) results from an expression for the friction force that acts on a sphere. The coefficient C_D , which is needed for the calculation of β , is determined with the reduced relative velocity ($s * u - v$) using the equations 2.19 to 2.21.

$$\rho_s * (1 - \varepsilon) * a_s + \rho_s * g * (1 - \varepsilon) - \beta * (s * u - v) = 0 \quad (4.3)$$

$$\rho_f * \varepsilon * a_f + \rho_f * g * \varepsilon + grad(p) + \beta * (s * u - v) = 0 \quad (4.4)$$

$$\beta = \frac{\rho_f * C_D * |s * u - v| * (1 - \varepsilon) * A_p}{V_p} \quad (4.5)$$

Initial condition:

As an initial condition, a starting value of the solid velocity has to be chosen. This starting value must be negative.

$$v_0 < 0 \quad (4.6)$$

Solution of the equations:

The unknown variables v , u , ε and $grad\ p$ in the equations 4.1 to 4.4 were determined using the Substitution Method as well as the Euler Method which is a numerical procedure for solving differential equations with a given initial value. [25]

First, the value v_i is used to determine the unknowns u_i and ε_i at the initial height H_i of the FR via the conservation of mass of the fluid and solid phases. Afterwards, the Euler Method is used on the equation of motion of the solid phase to receive the value v_{i+1} at the following height ($H_{i+1} = H_i - \Delta H$). The last remaining unknown $grad\ p_i$ can then be determined from the equation of motion of the fluid phase using the calculation of $grad\ u_i$ ($grad\ u_i = (u_{i+1} - u_i)/\Delta H$). Figure 33 illustrates the approach of the equations.

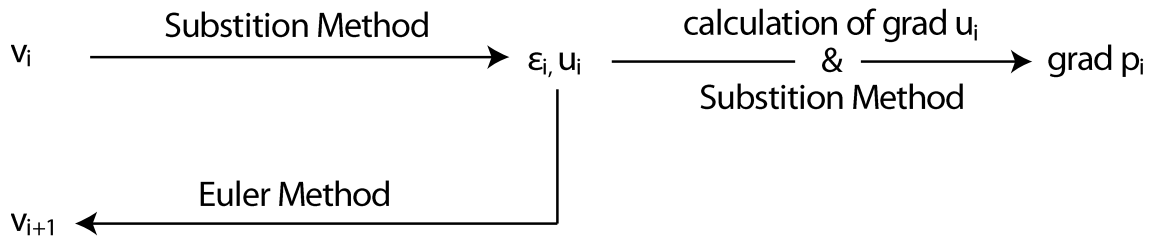


Figure 33: Solution of the equations

Limitations:

Due to the simplifications and assumptions of the model, it is subjected to some limitations thereby excluding certain effects which occur during operation of the FR:

- Due to the assumption of a constant downward direction of the solid velocity, the balance of mass considers only moving particles. Particles which keep in average their position cannot be considered and would always increase the solid fraction as well as the pressure gradient. For example this is the case for solid vortices, where the mass which is going up is compensated by the downward moving mass.

- Due to the missing zero fluid velocity boundary condition at the wall, the decreased friction force, particles are exposed which are closer to the wall can be only considered via the *factor s*. That means that the *factor s* has to be chosen such that the sum of the friction force is equal to reality, which can only be estimated.
- The limitation to a one dimensional model does not offer the possibility to consider special effects like flow contractions or enlargements and vortices.
- The assumption of a continuum reflects not the reality, as the particle concentration is varying locally. Furthermore, it was found out that particles which are near to each other are influencing each other fluid dynamically. This is the case for distances between the particles smaller than ten times their diameter [27]. Due to this fluid dynamical influence the calculation for the friction force in the model, which is based on the friction force on a single sphere, is probably not completely correct.
- As the equation of motion includes only a term for the friction force, the influence of other forces such as electromagnetic forces or impact forces between the particles cannot be considered.

5. Results and Discussion

5.1 Overview of the pressure inside the CFM

Pressure measurements and pressure profiles contain valuable information about the fluid dynamical processes inside a fluidized bed system. They provide information about frictional losses, solid distribution as well as solid flux and much more. Further, pressure profiles and measurements represent the most practical possibility to evaluate important parameters such as solid circulation and solid distribution inside a pilot plant, due to the fact that such a plant does not provide the possibility of visual assessment. Therefore, the aim of pressure measurements at a CFM should be to improve the understanding of the fluid dynamic processes inside a pilot plant.

5.1.1 Pressure without bed material

The measurements without bed material inside the CFM were performed at the standard operating point, which was found by preliminary calculations. The aim of the investigation was to prove the functionality of the measurement system, to identify regions which are subjected to special effects such as vortexes or stagnation points and to improve the understanding for the measurements with bed material inside the CFM.

Figure 34 shows the pressure profile of the CFM for the standard operating point. Further, the detailed pressure profile over the second constriction is depicted in Figure 35. During the measurement the fluidization rates of the LLS, ULS and ILS were kept constant. The adjustment of the different fluidization rates at the standard operating point are shown in Table 10. The overall AR and FR fluidization rates were calculated under the assumption that the LLS fluidization is equally distributed among AR and FR.

Table 10: Fluidization rates at standard operating point

	AR	FR	AR I	AR II	FR I	FR II	LLS	ULS	ILS
Fluidization rate [Nm³/h]	23	9.6	11.3	11.3	2.3	6.9	0.8	0.8	0.6

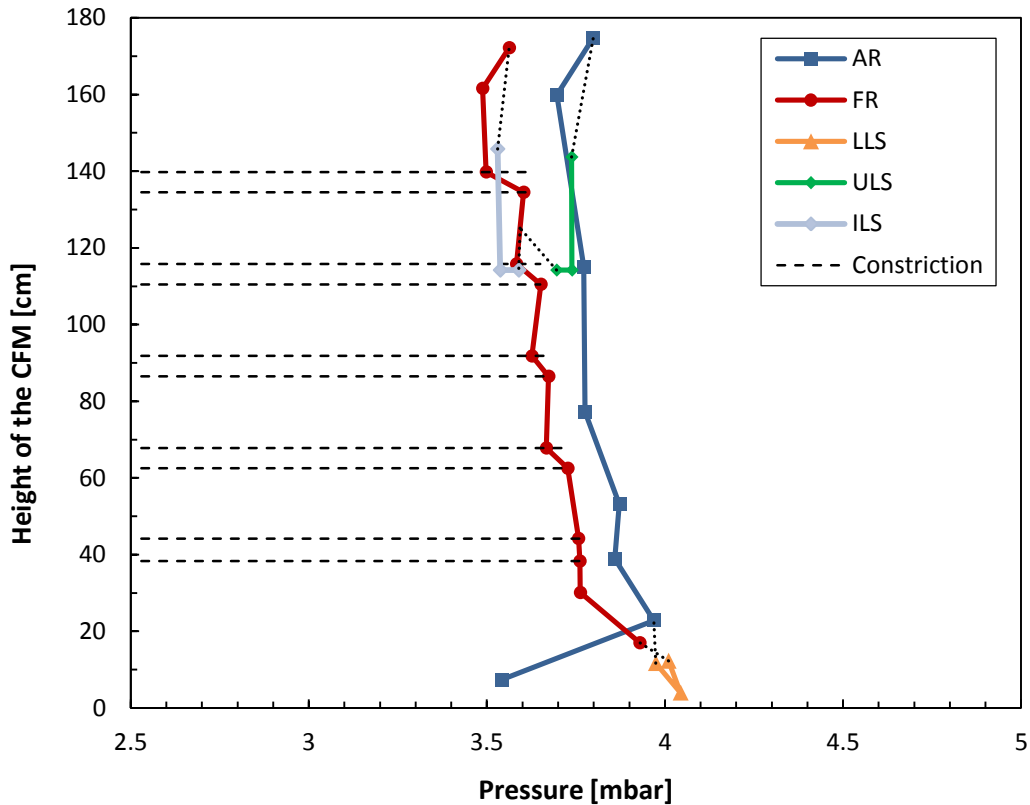


Figure 34: Overview of the pressure in the CFM without bed material
 AR = 23 Nm³/h, ARI : ARII = 50 : 50, FR = 9.6 Nm³/h, FRI : FRII = 25 : 75, LLS = 0.8 Nm³/h,
 ULS = 0.8 Nm³/h, ILS = 0.6 Nm³/h

As can be seen in Figure 34, two regions can be identified which are influenced by a stagnation point. These are both located at the top of the risers at which a sudden increase of the pressure occurs. The reason therefore lies in the riser exit configuration with its abrupt and flat ending where the dynamic pressure of the fluid is converted into static pressure.

In the FR, pressure drops are recognizable over the constrictions, which result from the increased gas velocity and friction loss. The pressure drop in the AR occurs continuously except fluctuations near the bottom which can be explained by the air supply of the different gas inlet ports into the AR. Due to the fact that a majority of the pressure is preserved after the riser outlets it can be assumed that the main pressure drop occurs in the filter.

The pressure profile of the ULS with the lower pressure inside the downcomer which connects the ULS to the FR and additionally the reason that the pressure in the FR is lower than in the AR suggest that the largest part of the ULS fluidization flows into the FR. The increased pressure drop over the last constriction is further an indication for this suggestion. Furthermore, the pressure distribution in the ILS suggests, due to the same considerations as mentioned for the ULS, that the largest part of the ILS fluidization flows into the FR separator.

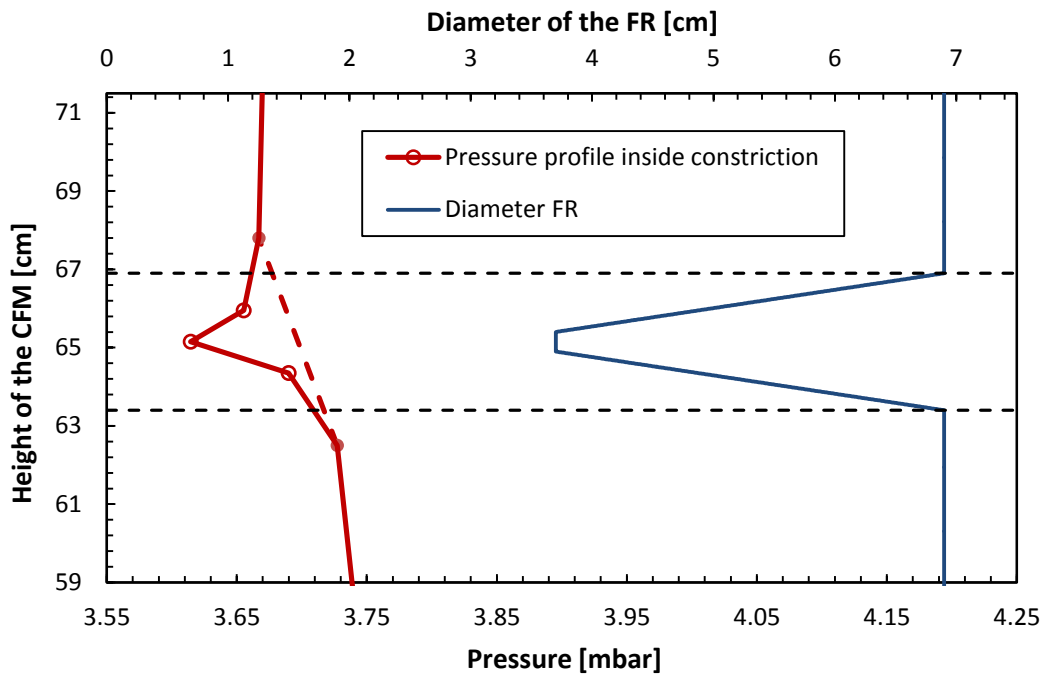


Figure 35: Pressure profile over the second constriction
 AR = 23 Nm³/h, ARI : ARII = 50 : 50, FR = 9.6 Nm³/h, FRI : FRII = 25 : 75, LLS = 0.8 Nm³/h,
 ULS = 0.8 Nm³/h, ILS = 0.6 Nm³/h

The detailed pressure profile of the constriction, illustrated in Figure 35, shows a decreasing pressure until the narrowest part, followed by a pressure increase. This is due to the change of the cross sectional area inside the constriction. The fluid velocity changes with the cross sectional area, thereby the pressure decreases with increasing velocity and vice versa. However, after the constriction the pressure does not recover to its initial state, due to friction losses inside the constriction as well as maybe due to the influence of inertial effects which occur at the outlet of the constriction. Furthermore, the pressure profile of the constriction shows no signs of an existing stagnation point which would influence the measurements.

5.1.2 Pressure at the standard operating point

The measurements at the standard operating point were performed using the standard fluidization rates, but with bed material. The aim of this investigation was to get an overview of the fluid dynamic processes occurring in the CFM and to develop an understanding for the interaction between the individual parts of the CFM.

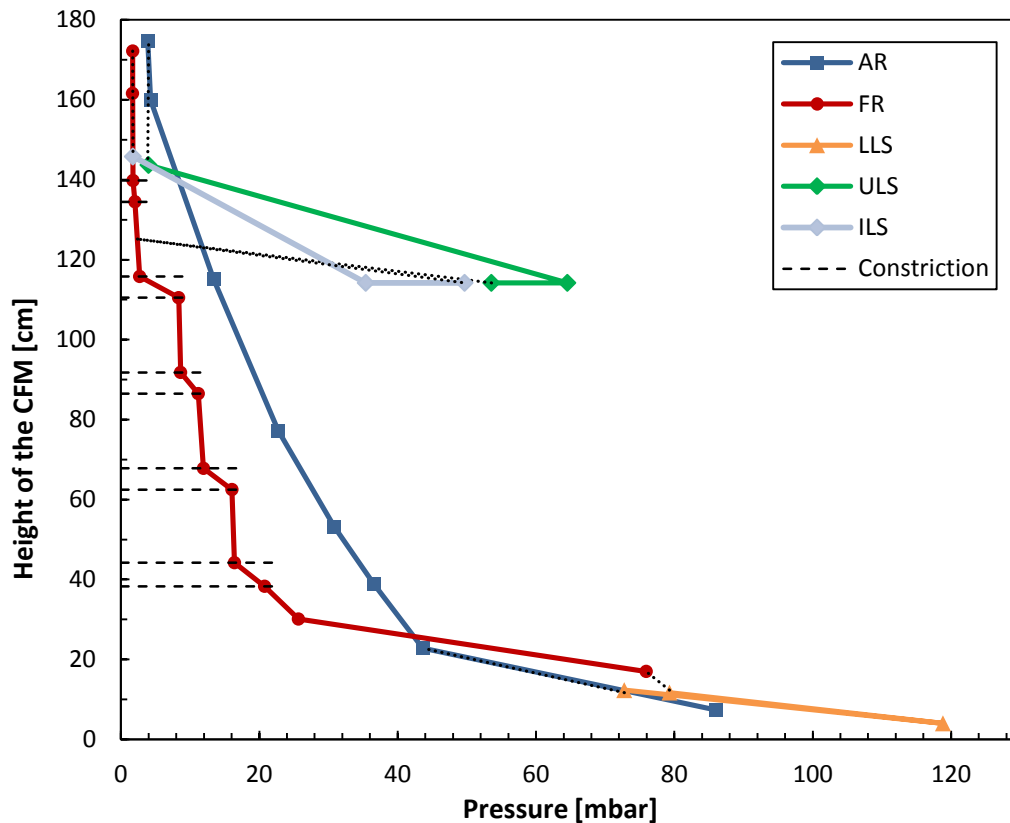


Figure 36: Overview of the pressure in the CFM with bed material
 AR = 23 Nm³/h, ARI : ARII = 50 : 50, FR = 9.6 Nm³/h, FRI : FRII = 25 : 75, LLS = 0.8 Nm³/h,
 ULS = 0.8 Nm³/h, ILS = 0.6 Nm³/h

As can be seen in Figure 36, the pressure along the height of the CFM is mostly higher in the AR than in the FR. Thereby, a leakage between AR and FR is prevented by the much higher pressures in the LLS and the ULS which act as gas locks. Further, the high pressure in the ILS prevents a gas flow from the FR over the ILS into the coarse separator.

The high pressure drops over the loop seals are due to their high solid inventory which is typical for their operation in the bubbling bed regime. Further, the pressure drop over the loop seals can be used as an indicator for their solid inventory. As the pressure drop over the ILS is higher than that over the ULS and both have the same dimensions, it can be assumed that the ILS contains more particles than the ULS. This can be related to the lower fluidization rate of the ILS (0.6 Nm³/h) compared to the ULS (0.8 Nm³/h).

The pressure profiles of both, AR and FR show significant higher pressure drops at the bottom of the reactors, which are due to the dense particle phase in this sections and the resulting high solid fraction. In the upper part of the FR, the pressure drops occur step-wise with significant pressure drops over the constrictions, while the pressure inside the AR decreases continuously. The very low pressure drop, inside the FR above the inlet of the ILS, indicates that almost all particles, transported from the AR to the FR, move to the bottom.

The higher pressure at the inlet of the LLS into the AR, compared to the inlet into the FR, suggests that the bigger part of the LLS fluidization flows into the AR. Due to the lower pressure at the inlet of the ULS into the FR compared to the pressure at the inlet into the coarse separator

of the AR it seems that the bigger part of the ULS fluidization flows into the FR. The pressure profile of the ILS suggests that the main part of the ILS fluidization flows into the coarse separator of the FR.

5.2 Solid circulation

Solid circulation is an important parameter for the oxygen transport as well as for the heat transport in a CLC plant. Therefore it is useful to know the parameters which are influencing the solid circulation. The influences of the AR fluidization, the FR fluidization and gas staging on global and internal circulation were investigated. During these investigations the LLS, ULS and ILS fluidization rates were kept constant. The fluidization rates were chosen such that no limitation of the solid circulation by the loop seals can occur. To provide an overview of the range of the measurements, the corresponding standard deviations are represented by a cap in the following diagrams.

5.2.1 Global circulation

The global circulation for five different AR fluidization rates and three different gas staging distributions were determined. Further, to evaluate the influence of the FR fluidization investigations were performed for two different FR fluidizations.

Figure 37 and Figure 38 show the development of the global circulation as a function of the AR fluidization for different gas staging distributions at a constant FR fluidization of $7.6 \text{ Nm}^3/\text{h}$ and $12.6 \text{ Nm}^3/\text{h}$, respectively. The AR fluidization range in Figure 38 ends prior to these in Figure 37 due to the fact that at higher fluidization rates, stable operation is not possible anymore. The reasons therefore will be discussed later. A comparison of the global circulation at different FR fluidization rates is depicted in Figure 39.

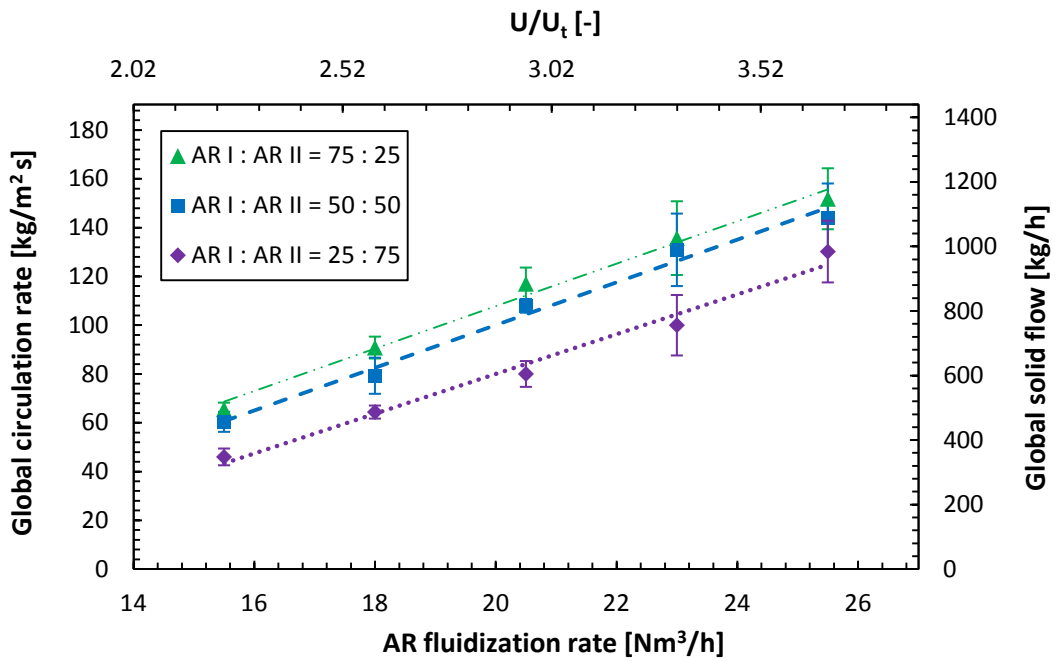


Figure 37: Development of the global circulation with the AR fluidization rate for FR = 7.6 Nm³/h
 FRI : FRII = 25 : 75; LLS = 0.8 Nm³/h; ULS = 0.8 Nm³/h; ILS = 0.6 Nm³/h

As Figure 37 and Figure 38 show there is a linear relationship between the AR fluidization and the global circulation. Further, it can be recognized an increase of the global circulation with increasing share of the AR I fluidization rate. This is due to the fact that the AR I inlet port is situated lower than the AR II inlet port. An increased fluidization to the lower section of the riser leads to an expansion of the dense lower section whereby allowing an easier transport of the particles to the exit of the riser.

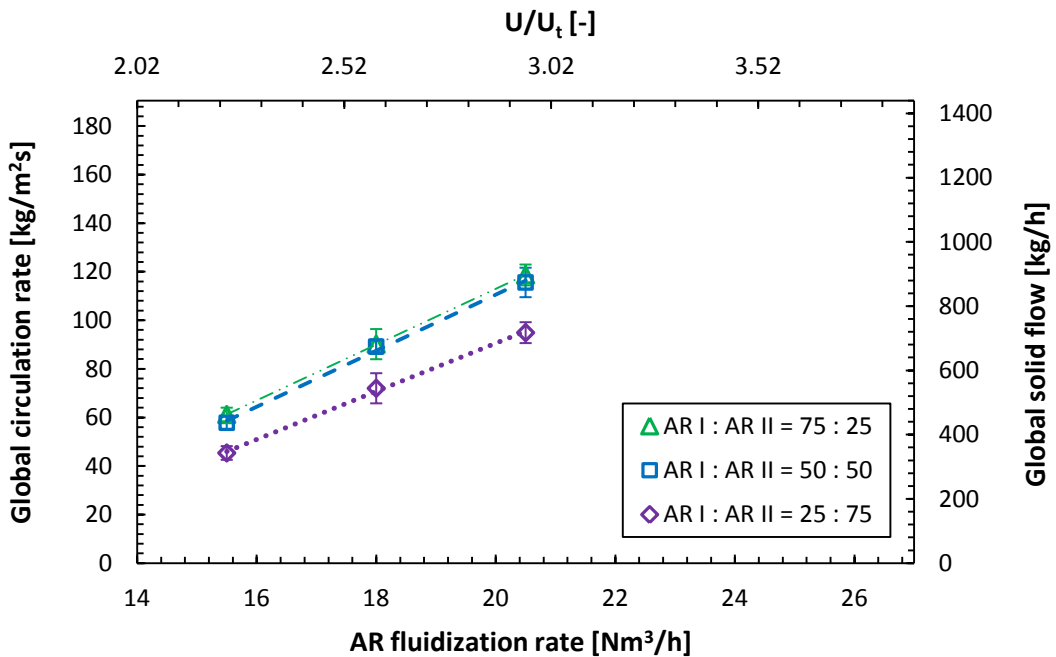


Figure 38: Development of the global circulation with the AR fluidization rate for FR = 12.6 Nm³/h
 FRI : FRII = 25 : 75; LLS = 0.8 Nm³/h; ULS = 0.8 Nm³/h; ILS = 0.6 Nm³/h

Figure 39 shows that the influence of the FR fluidization increases with the AR fluidization and share of the AR II fluidization. This can be recognized at the significant influence of the FR fluidization for an AR II share of 75 %, whereas at an AR II share of 25 % no changes are recognizable. This effect can be related to the increased pressure in the FR which causes a higher share of the LLS fluidization to flow into the AR where it acts same as an additional gas staging between the AR I and AR II inlet port.

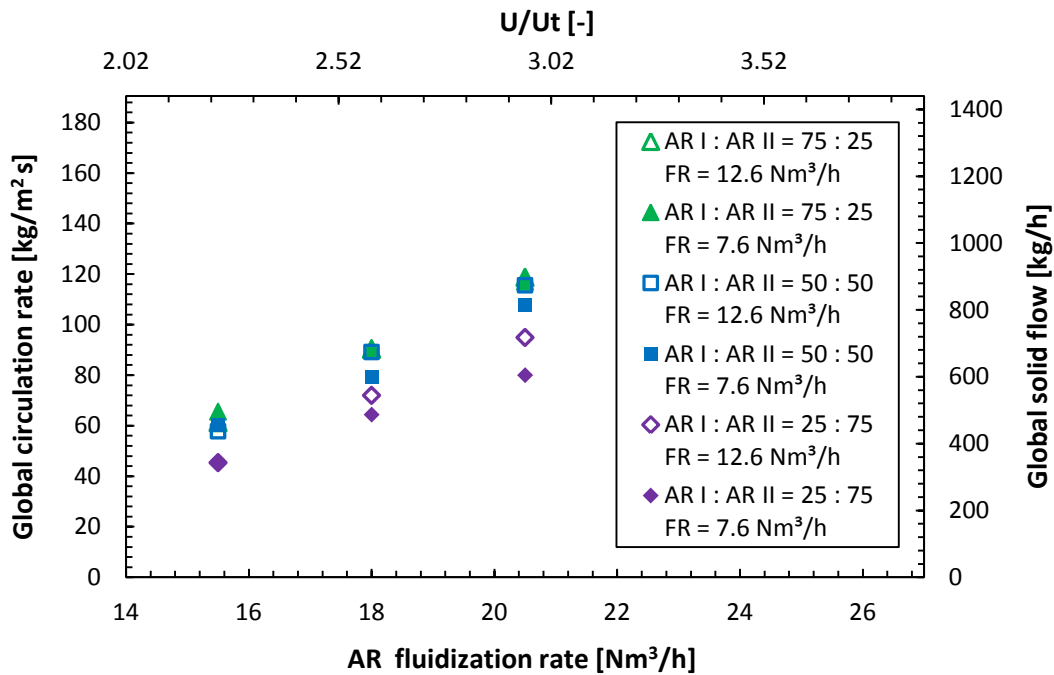


Figure 39: Comparison of the global circulation rate for different FR fluidization rates
 ARI : ARII = 50 : 50, FRI : FRII = 25 : 75, LLS = 0.8 Nm³/h, ULS = 0.8 Nm³/h, ILS = 0.6 Nm³/h

In summary, the global circulation can be influenced by all three investigated parameters (AR fluidization, FR fluidization, gas staging), where the AR fluidization rate has the biggest influence followed by gas staging.

5.2.2 Internal circulation

For the internal circulation, investigations on seven different FR fluidization rates, with and without global circulation were done, with the aim to evaluate the influence of the different parameters. As the operating range of the FR I fluidization is limited to 5 Nm³/h while the FR II fluidization can handle up to 17 Nm³/h only one gas staging distribution was chosen which can be kept constant for the entire investigated FR fluidization range.

Figure 40 shows the development of the internal circulation in dependence of the FR fluidization rate, by comparison with and without a global circulation. Due to the operation of the LLS fluidization, which is distributed into the AR and FR, an AR fluidization rate of zero is not possible. However, due to the low AR fluidization no global circulation occurred and the particles were not able to get from the AR into the FR.

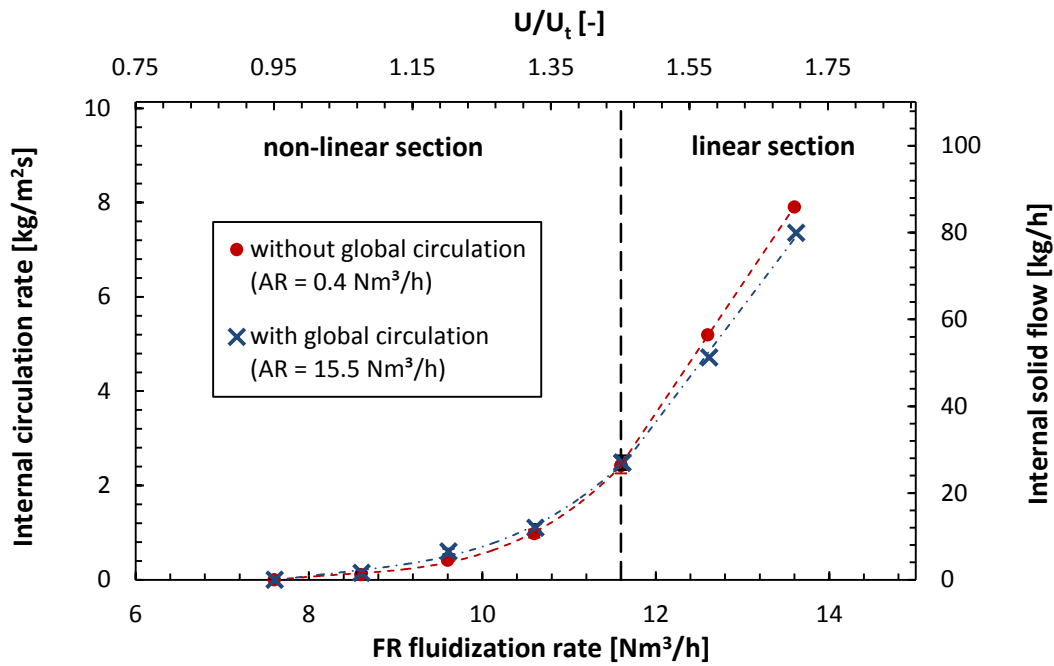


Figure 40: Development of the internal circulation
 ARI : ARII = 50 : 50, FRI : FRII = 25 : 75, LLS = 0.8 Nm³/h, ULS = 0.8 Nm³/h, ILS = 0.6 Nm³/h

The internal circulation in dependence on the FR fluidization can be divided into two sections. These are a section with a non linear increase of the internal circulation, reaching from FR fluidization rates of 7.6 Nm³/h to 11.6 Nm³/h and a section with a linear increase for fluidization rates higher than 11.6 Nm³/h.

It shows that the internal circulation increases in the non linear section with a global circulation, compared to without a global circulation, while it decreases in the linear section. Whereas, at the beginning in the non linear section the benefit of additional particles inside the FR predominates, in the linear section the hindrance of rising particles by particles which are dropping down and acting as barriers dominates.

Comparing the internal circulation to the global circulation it can be recognized that the share of the uprising particles is much smaller than the downward moving particles.

5.3 Solid distribution in the FR

In classical designs of turbulent or fast fluidized beds the solid fraction is substantially higher in the lower parts than in the upper parts of the reactor. Therefore, the upper part of the reactor cannot be used effectively for oxidation of fuel. One of the main objectives of the novel DUAL FLUID reactor concept is to increase the solid fraction over the height of the reactor and consequently to influence the solid distribution.

To investigate the ability of the novel DUAL FLUID reactor concept to influence the solid distribution, pressure measurements over the height of the FR were performed. As pressure drop and pressure gradient provide valuable information on the solid fraction they were used for the evaluation of the solid distribution. Although, it has to be noted that solid fraction and solid particles, respectively, account not exclusively for pressure drops and gradients (see chapter

2.4.1). Only in particular cases or under specific assumptions solid fraction and pressure drop are directly linked (see chapter 2.7).

The influence of the AR and FR fluidization rate on the solid distribution in the FR was under investigation. Thereby, the pressure drop over the height of the FR was used for the evaluation of the progression of the accumulated solid mass or rather particles, over the height of the reactor. Further, the pressure gradient was used for the evaluation of the local solid fraction. As normalization is an important tool to check for similarities, the pressure drops over the height were normalized to compare solid distributions to each other as well as to evaluate their change by variation of a specific parameter (AR and FR fluidization rate). During the measurements, the fluidization of the loop seals as well as the adjustments of the gas staging were kept constant and can be found below the figures.

5.3.1 Solid distribution by variation of the FR fluidization rate

For investigation of the influence of the FR fluidization on the solid distribution, the FR fluidization rate was changed to higher as well as lower fluidization rates compared to the standard operating point.

Figure 41 shows, the pressure drop (left side) and pressure gradient (right side) over the height of the FR for the standard operating point compared to three different FR fluidization rates. Figure 42 illustrates their normalized pressure drops as well as pressure gradients over the height of the FR. Thereby the pressure drop is normalized to the pressure drop over the whole height, while the gradient of these normalized pressure profile represents the normalized pressure gradient (i.e. the slope of the normalized pressure profile).

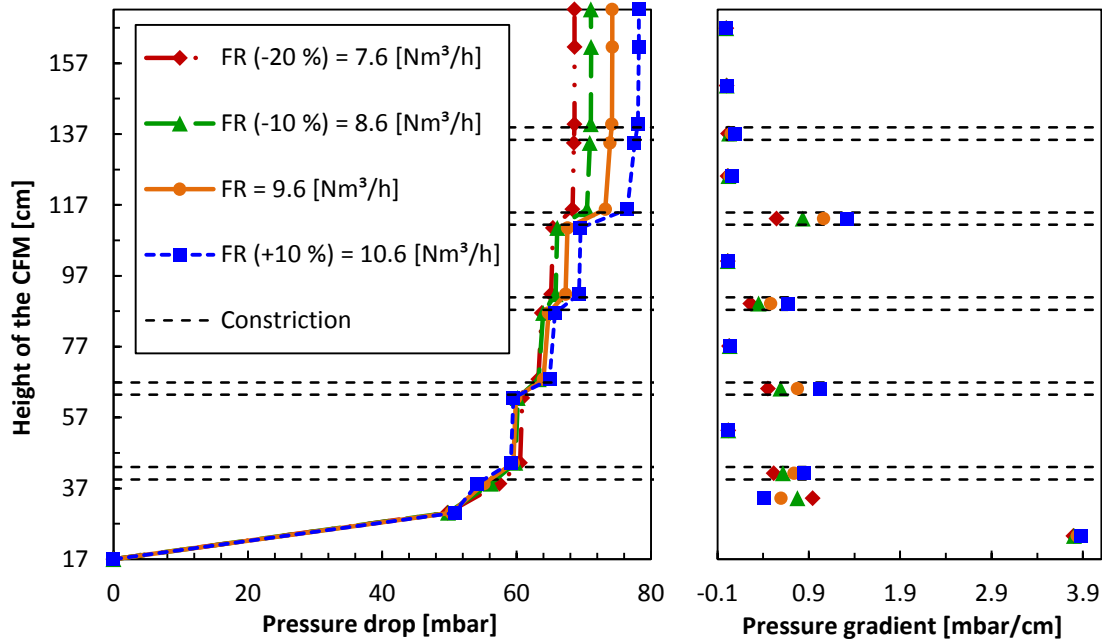


Figure 41: Pressure drop and pressure gradient over the height of the FR by variation of the FR fluidization rate
 AR = 23 Nm³/h, ARII : ARII = 50 : 50, FRI : FRII = 25 : 75, LLS = 0.8 Nm³/h, ULS = 0.8 Nm³/h,
 ILS = 0.6 Nm³/h

From Figure 41 it can be recognized that the pressure drop increases with the FR fluidization rate, which suggests that also the amount of particles situated in the FR increases. Further, the location of the highest pressure gradients shows that most of these particles are located at the bottom of the reactor as well as inside the constrictions.

Figure 42 shows that the share of the pressure drop of the upper parts of the FR increases significantly with the FR fluidization rates. Therefore it can be assumed that also the solid fraction in the upper part of the FR increases with the FR fluidization rate.

The normalized pressure gradient shows the local share on the total pressure drop and can therefore be used to identify local changes in the pressure distribution and consequently the solid distribution. Thereby, differences between the normalized pressure gradients refer to such local changes in the pressure distribution. Comparing the normalized pressure gradients in Figure 42, it can be recognized that the pressure distribution changes mainly in the constrictions and in the dense phase at the bottom with the FR fluidization rate. Changes between the constrictions cannot be observed.

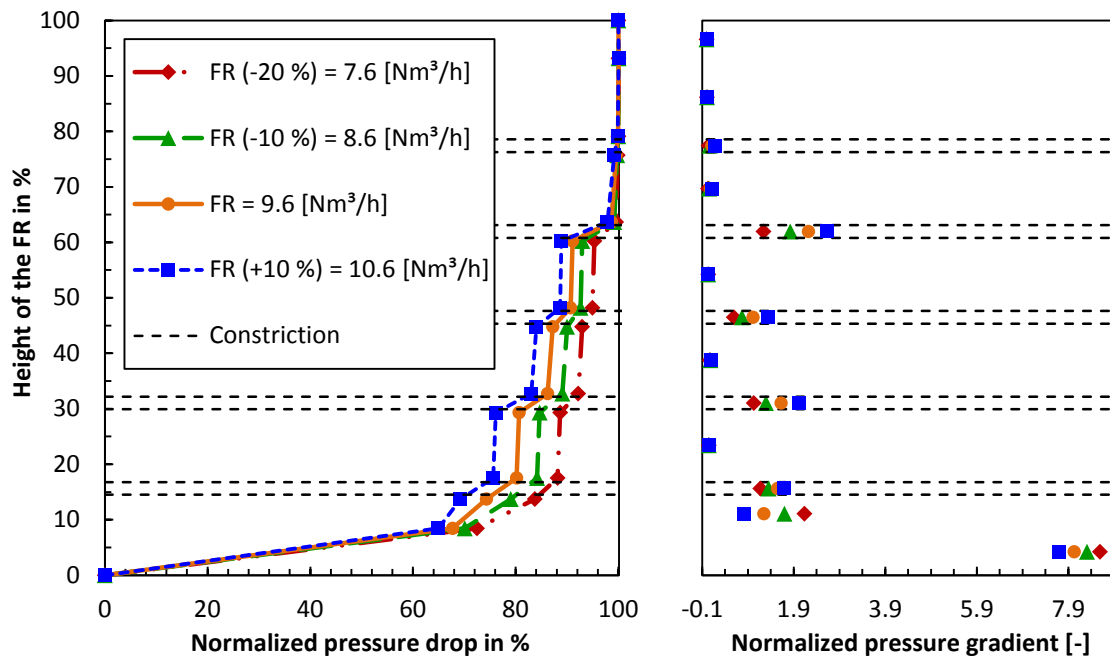


Figure 42: Normalized pressure drop and pressure gradient over the height of the FR by variation of the FR fluidization rate
 AR = 23 Nm³/h, ARI : ARII = 50 : 50, FRI : FRII = 25 : 75, LLS = 0.8 Nm³/h, ULS = 0.8 Nm³/h,
 ILS = 0.6 Nm³/h

5.3.2 Solid distribution by variation of the AR fluidization rate

For investigation of the influence of the AR fluidization on the solid distribution, the AR fluidization rate of the standard operating point was varied to bigger as well as smaller fluidization rates.

Figure 43 shows, the pressure drop (left side) and pressure gradient (right side) over the height of the FR of the standard operating point compared to three different AR fluidization rates. Figure 44 illustrates their normalized pressure drops as well as pressure gradients.

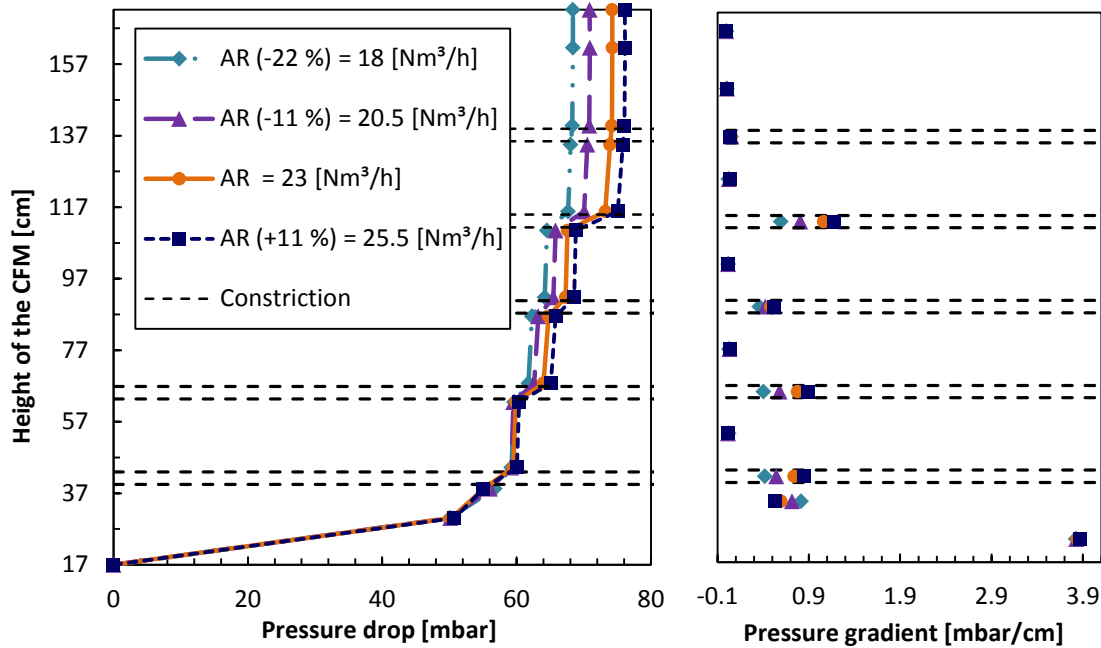


Figure 43: Pressure drop and pressure gradient over the height of the FR by variation of the AR fluidization rate
ARI : ARII = 50 : 50, FR = 9.6 Nm³/h, FRI : FRII = 25 : 75, LLS = 0.8 Nm³/h, ULS = 0.8 Nm³/h,
ILS = 0.6 Nm³/h

As Figure 43 shows, same as for the variation of the FR fluidization rate, the pressure drop over the height of the FR increases with the AR fluidization rate. Therefore, it can be assumed that also an increase of the AR fluidization causes a significant rise of the amount of particles inside the FR. Further, the high pressure gradients at the bottom of the FR as well as inside the constrictions suggest that the majority of the particles are situated there.

Figure 44 shows that the share of the pressure drop of the upper parts of the FR increases significantly with the AR fluidization rate and so it can be assumed that also the solid distribution in the upper parts increases too. Though, it can be recognized that the influence of the AR fluidization rate on the solid distribution is not as strong as for the FR fluidization rate.

Further, the normalized pressure gradients show that these changes in the pressure distribution over the whole height of the FR are caused almost exclusively by local changes in the pressure distribution in the constricted areas.

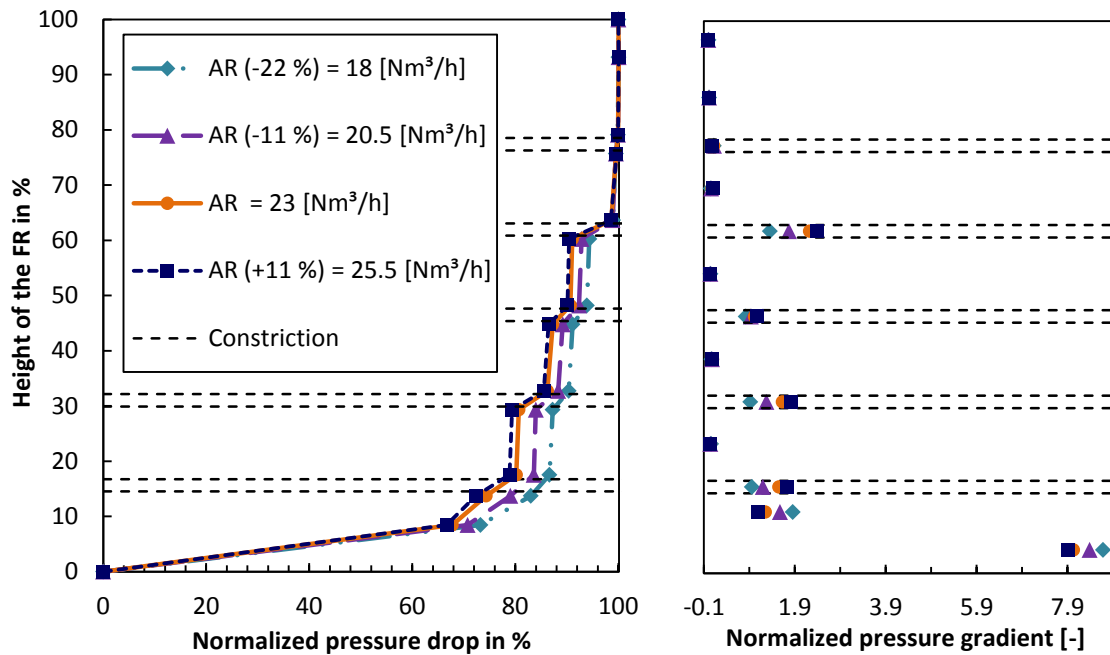


Figure 44: Normalized pressure drop and pressure gradient over the height of the FR by variation of the AR fluidization rate
ARI : ARII = 50 : 50, FR = 9.6 Nm³/h, FRI : FRII = 25 : 75, LLS = 0.8 Nm³/h, ULS = 0.8 Nm³/h,
ILS = 0.6 Nm³/h

Considering the results for the variation of the FR and AR fluidization rates, this leads to the assumption that the constricted areas have a strong influence on the solid distribution of the FR. Thereby, the constrictions cause a significant increase of the solid fraction in the upper parts of the reactor with increasing FR as well as AR fluidization rates.

5.4 Solid distribution in a chamber

The solid distribution in the chamber is important to know, because it provides information about the influence of the constrictions on the solid fraction and allows conclusions for design optimization.

Same as for the investigations of the solid distribution in the FR, pressure drop and pressure gradient, as well as their normalized forms, over the height of the chamber were used for the evaluation of the solid distribution.

For the determination of the pressure drop over a chamber, the pressure profile of the second chamber was chosen. For that purpose, three additional pressure measuring ports were placed inside the second constriction and eight measurement ports were distributed between the second and third constriction. During the measurements, the fluidization of the loop seals as well as the adjustments of the gas staging were kept constant and can be found below the figures.

5.4.1 Solid distribution without AR fluidization

To investigate the fluid dynamic behavior without global circulation and therefore, without solid particles entering the FR from the AR, investigations with almost no AR fluidization were performed. The pressure profiles of these measurements were then compared to pressure profiles which were calculated for a friction free flow without particles inside the FR.

In Figure 45 the pressure profiles over the second chamber for four FR fluidizations and almost no AR fluidization are illustrated. An AR fluidization rate of zero is not possible due to the operation of the LLS fluidization during the experiments, which is distributed into both reactors. However, due to the low AR fluidization no global circulation occurred.

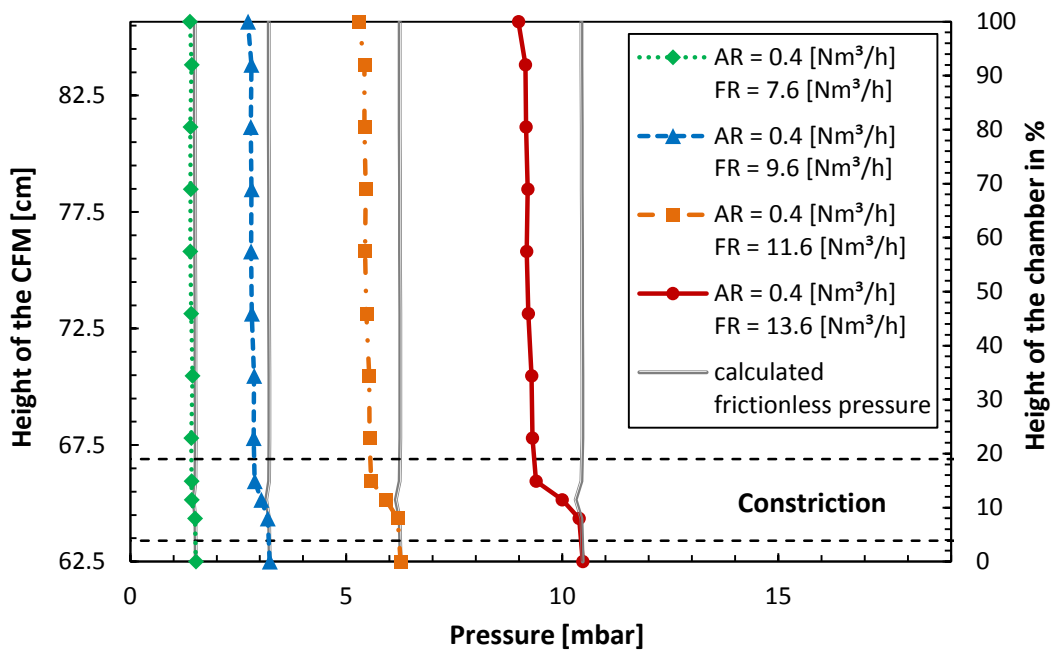


Figure 45: Pressure profile over the second chamber without fluidization of the AR
 ARI : ARII = 50 : 50, FRI : FRII = 25 : 75, LLS = 0.8 Nm³/h, ULS = 0.8 Nm³/h, ILS = 0.6 Nm³/h

Even without fluidization of the AR, particles which rise from the bottom distribute over the height of the FR. This can be seen in Figure 45 at the increased pressure drop compared to the corresponding frictionless pressure profile. As the main pressure drop, compared to the frictionless pressure, occurs in the upper part of the constriction it can be assumed that the majority of the particles are situated there. Moreover, the fact that nearly no pressure drop occurs between the constrictions suggests that only a minor proportion of the particles rise to the next chamber.

Further, visual observations during the measurements without AR fluidization showed that, when particles get close to the constriction they start to circulate. This suggests that the particles located in the upper part of the constriction are arranged in a particle vortex (see section 5.4.2), whereby they are circulating between the middle and the upper end of the constriction.

Further, it can be assumed that also during operation of the AR, particles rise from the bottom and distribute in the upper part of the constriction. This leads to higher pressure drops and

gradients in this region, using a global circulation, than it would be caused only by the particles entering through the ULS.

5.4.2 Solid distribution by variation of the FR fluidization rate

To estimate the influence of the FR fluidization rate on the solid distribution in a chamber, the progression of the pressure drop and the pressure gradient by variation of the FR fluidization rate was investigated. Therefore, the FR fluidization rate of the standard operating point was changed to bigger as well as smaller fluidization rates, while the other fluidization rates of the standard operating point were kept constant.

Figure 46 shows, the pressure drop (left side) and pressure gradient (right side) over the height of the second chamber for the standard operating point compared to three other FR fluidization rates. Figure 48 illustrates their normalized pressure drops as well as pressure gradients.

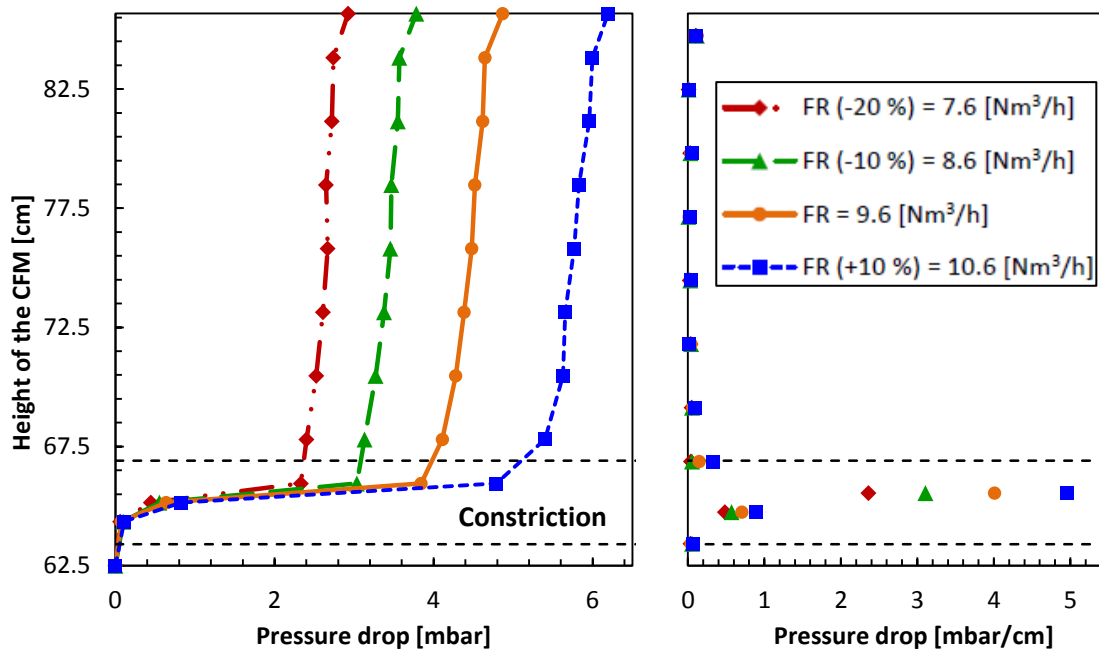


Figure 46: Pressure drop and pressure gradient over the second chamber by variation of the FR fluidization rate
 $AR = 23 \text{ Nm}^3/\text{h}$, $ARI : ARII = 50 : 50$, $FRI : FRII = 25 : 75$, $LLS = 0.8 \text{ Nm}^3/\text{h}$, $ULS = 0.8 \text{ Nm}^3/\text{h}$,
 $ILS = 0.6 \text{ Nm}^3/\text{h}$

Figure 46 shows that the pressure drop over the chamber increases considerably with the FR fluidization. Basically, this is due to the increasing amount of particles inside the chamber. Higher FR fluidizations cause higher friction forces between fluid and particles, whereby the velocity of the downward moving particles in the FR decrease. As can be gathered from the conservation of mass for the solid phase (see equation 4.1), this leads to an increase of the solid fraction due to the fact that the global circulation rate has to be kept constant. Further, due to the increasing number of particles which rise from the bottom of the FR with increasing FR fluidization rates and distribute over the height, the solid fraction in the chamber and so the pressure drop is again increased. As the by far highest pressure gradients occur in the upper part of the constriction, it can to be assumed that the majority of the particles are situated there.

Additionally, it is probable that the formation of a particle vortex is caused by particles rising from the bottom of the reactor as well as downward moving particles which are carried with the upward moving fluid stream.

The very low pressure gradient between the constrictions does not necessarily reflect the real solid fraction at this section. Particles can also cause pressure gradients such that it seems they are situated at other places. Figure 47 illustrates this for a particle vortex.

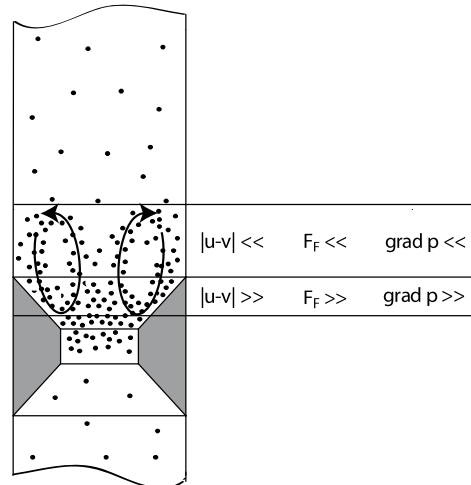


Figure 47: Influence of particle vortex on the pressure gradient

Relative velocity and friction force between fluid and particles as well as pressure gradient are strongly related to each other. Thereby, an increase of the relative velocity causes an increase of friction force and pressure gradient. In a particle vortex, the particles are accelerated at the bottom of the vortex by the fluid stream whereby their velocity increases. Due to the now higher particle velocities the relative velocity decreases which results in a decreasing friction force and pressure gradient. At the top of the vortex, particles change their direction of motion, whereby the relative velocity of the downward moving particles increases again. Expressed in a different way, at the bottom of the vortex the particles receive the kinetic energy which they need to reach the top of the vortex.

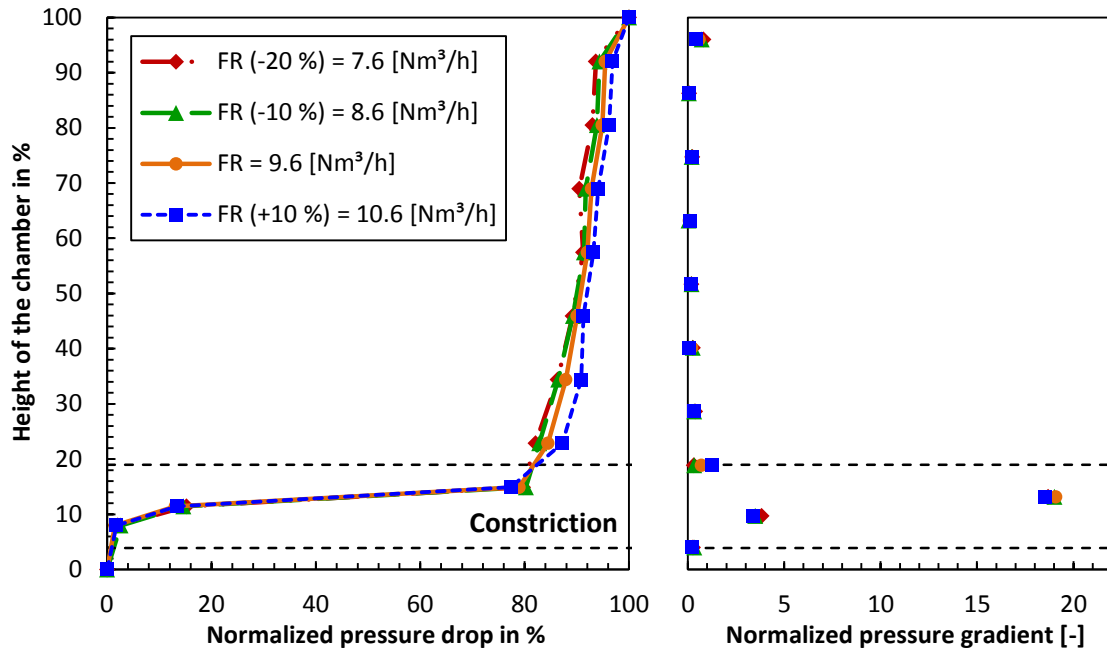


Figure 48: Normalized pressure drop and pressure gradient over the second chamber by variation of the FR fluidization rate
 AR = 23 Nm³/h, ARI : ARII = 50 : 50, FRI : FRII = 25 : 75, LLS = 0.8 Nm³/h, ULS = 0.8 Nm³/h,
 ILS = 0.6 Nm³/h

As Figure 48 shows, changes in the normalized pressure drop as well as the normalized pressure gradient over the chamber are hardly recognizable by variation of the FR fluidization rate. Therefore, it can be expected that the influence of the FR fluidization on the solid distribution in the chamber is negligible.

5.4.3 Solid distribution by variation of the AR fluidization rate

The influence of the AR fluidization rate on the solid distribution in the chamber was investigated by variation of the AR fluidization rate of the standard operating point using the pressure drop and pressure gradient over the height of the chamber.

Figure 49 shows, the pressure drop and the pressure gradient at the standard operating point over the height of the second chamber compared to three other AR fluidization rates. Figure 50 shows the corresponding normalized pressure drops and pressure gradients.

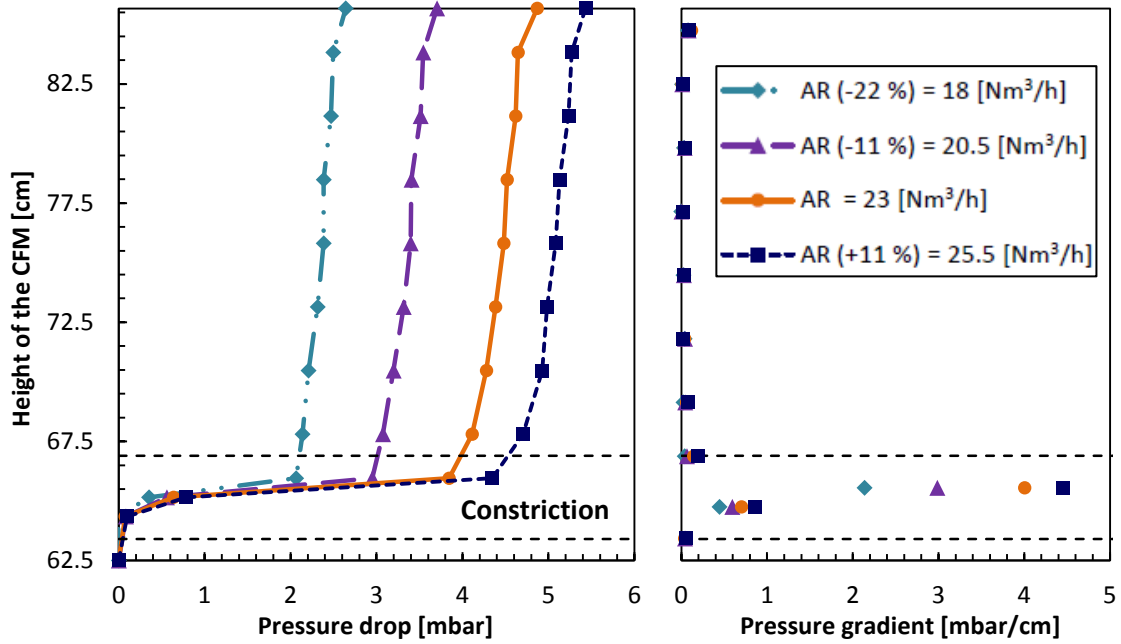


Figure 49: Pressure drop and pressure gradient over the second chamber by variation of the AR fluidization rate
 ARI : ARII = 50 : 50, FR = 9.6 Nm³/h, FRI : FRII = 25 : 75, LLS = 0.8 Nm³/h, ULS = 0.8 Nm³/h,
 ILS = 0.6 Nm³/h

Pressure drop and gradient over the height of the chamber, illustrated in Figure 49, show a very similar development than for the former investigations for the variation of the FR fluidization rate. The pressure drop over the chamber increases with the AR fluidization rate, just as for the variation of the FR fluidization rates. This is due to the increasing amount of particles transported from the AR into the FR, causing an increase of the solid fraction in the chamber. The pressure gradients suggest also that the majority of the particles are situated in the upper part of the constriction.

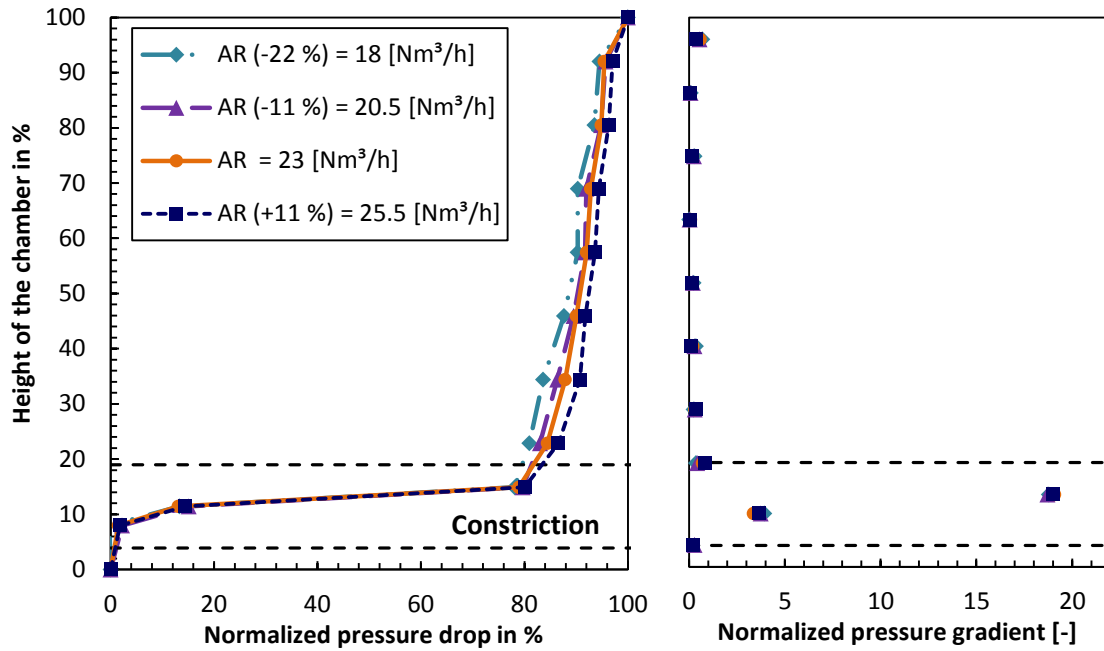


Figure 50: Normalized pressure drop and pressure gradient over the second chamber by variation of the FR fluidization rate
ARI : ARII = 50 : 50, FR = 9.6 Nm³/h, FRI : FRII = 25 : 75, LLS = 0.8 Nm³/h, ULS = 0.8 Nm³/h,
ILS = 0.6 Nm³/h

As Figure 50 shows, same as for the variation of FR fluidization rates, the deviations of normalized pressure drop and pressure gradient are very small. Therefore, it can be assumed that also the influence of the AR fluidization rate on the solid distribution in the chamber can be neglected.

5.5 Mean solid fraction in a chamber

The mean solid fraction in the chambers represents an important operating parameter for the CFM. Therefore, it is useful to know the influencing parameters as well as their individual weightings.

The influence of the AR and FR fluidization rate on the mean solid fraction in the chambers was investigated. Therefore, the development of the mean solid fraction for five AR fluidization rates with the FR fluidization rate was explored. Thereby, the FR fluidization rate was increased until unstable operation, which will be discussed in the next chapter, occurred.

For the evaluation of the mean solid fraction in the chambers, the pressure profile over the FR as well as equation 2.41 were used. As described in chapter 2.7, this equation holds only for equal particle velocities at the pressure measurement points. Therefore, only the last three chambers were used for the calculation of the mean solid fraction, to ensure that the inlet and outlet particle velocity of the chambers have reached equilibrium. Afterwards, the arithmetic middle of the solid fraction in the individual chambers was used for the evaluation of the overall mean solid fraction in a chamber.

During the measurements, the fluidization of the loop seals as well as the adjustments of the gas staging were kept constant and can be found below Figure 51.

Figure 51 shows the calculated overall mean solid fraction of the chambers one to three in dependence of the FR fluidization for the five AR fluidizations. The dashed black lines illustrate the results for the standard operating point.

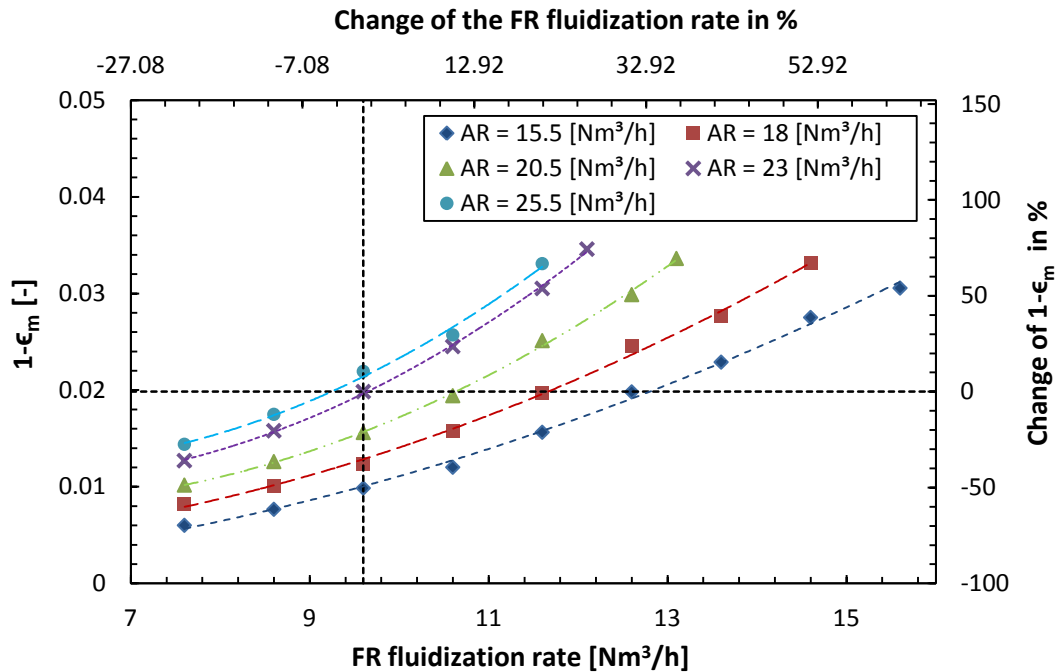


Figure 51: Progress of the mean overall solid fraction in a chamber in dependence of the FR fluidization rate
 ARI : ARII = 50 : 50, FRI : FRII = 25 : 75, LLS = 0.8 Nm³/h, ULS = 0.8 Nm³/h, ILS = 0.6 Nm³/h

The overall mean solid fraction in the chambers increases non-linear with the FR fluidization rate. Further, it can be recognized that an increase of the overall mean solid fraction can also be reached by an increase of the AR fluidization rate.

As for every AR fluidization rate in Figure 51, the operation point with the highest FR fluidization rate represents the limit of stable operation, it can be recognized that the highest possible mean solid fraction in the chamber is approximately the same for all AR fluidization rates. Further, this means that the transition from stable to unstable operation occurs at approximately the same solid fractions in the chambers.

5.6 Mechanisms influencing the operating range

During the investigations at the CFM, limitations of stable operation and therefore a possible operating range occurred. These limitations of stable operation are important to know for such a fluidized bed system. To better understand the mechanisms during stable operation and further to identify the reasons which cause unstable operation, a simulation was performed. To determine the influence of different FR geometries on the operating ranges of the CFM, the results of the circular shaped FR used for this thesis, were compared to these of an rectangular

shaped FR with the same cross sectional area, which was used for previous investigations [25]. Further, to evaluate the influence of the bed inventory on the operating range, three different bed material inventories were used for investigations.

5.6.1 Operating mechanisms

The mechanisms which occur inside the FR during operation, with special interest on the influence of the constrictions were investigated. Therefore, the mathematical model which is described in chapter 4 was used. It turned out that for the explanation of the basic mechanisms one chamber can be divided into three sections. Figure 52 shows a chamber with its three sections and the basic mechanisms during stable operation. In the Figure 53 to 55 the normalized results of the simulation, for the conservation of mass and the equation of motion, for fluid and solid phase are depicted.

Basic mechanisms:

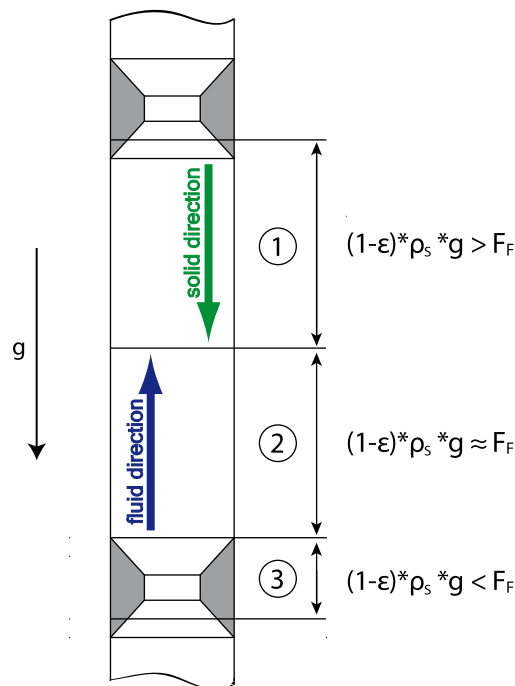


Figure 52: Basic mechanisms in a chamber

Section 1:

The cross sectional area increases and the particles leave the constriction with a smaller frictional force (F_F), acting on the particles, than the gravitational force. This leads to an acceleration of the particles in the direction of the gravitational force, which results in an increase of the particle velocity and a decrease of the solid fraction.

Section 2:

The increased relative velocity between particles and fluid leads to equilibrium between the frictional force and the gravitational force and the particles keep their velocity. Since particle velocity, as well as the cross sectional area, do not change, the solid fraction remains constant.

Section 3:

Due to the decreasing cross sectional area of the FR, the fluid velocity increases and causes an increase of the relative velocity as well as of the frictional force. At a specific cross sectional area, the frictional force is bigger than the gravitational force and the particles get now accelerated against the direction of the gravitational force and their velocity decreases. The decreasing velocity and cross sectional area, cause an increase of the solid fraction. After the narrowest point is reached, the cross sectional area increases, while the solid fraction as well as the difference between frictional force and gravitational force decrease and the procedure is repeated for the next chamber.

Simulated results:

The following figures show the simulated normalized results at the standard operating point for the conservation of mass and the equation of motion for the fluid and solid phase. The mass flow (\dot{m}_g) was chosen with 0.28 kg/s same as measured for the CFM at the standard operating point.

The factor s , which reduces the fluid velocity when calculating the friction force, was chosen with 0.3 such that unstable operation is reached at the same FR fluidization rate as in reality. The initial velocity (v_0) was chosen such that friction force and gravitational force are at equilibrium ($a_s=0$). The integration steps (ΔH) were chosen with 5 μm .

For the conservation of mass the results were normalized by their absolute values at the initial position of the height, for example, $A/|A_0|$, $v/|v_0|$ or $\epsilon/|\epsilon_0|$. As the friction force connects the solid phase and the fluid phase, the results of the equation of motion are normalized by the absolute value of the friction force at the zero position, for example, $F_F/|F_{F0}|$, $F_G/|F_{F0}|$ or $\text{grad } p/|F_{F0}|$.

Solid phase:

As can be seen in Figure 53, a substantial increase of the solid fraction (up to 500 %) occurs in the constricted area, which is a result of the decreasing particle velocity and cross sectional area. Further, the equation of motion which is depicted in Figure 54, shows that the reason for the decreasing particle velocity is a tremendous increase of the friction force (F_F) (up to 900 %) which exceeds the increase of the gravitational force (G_s).

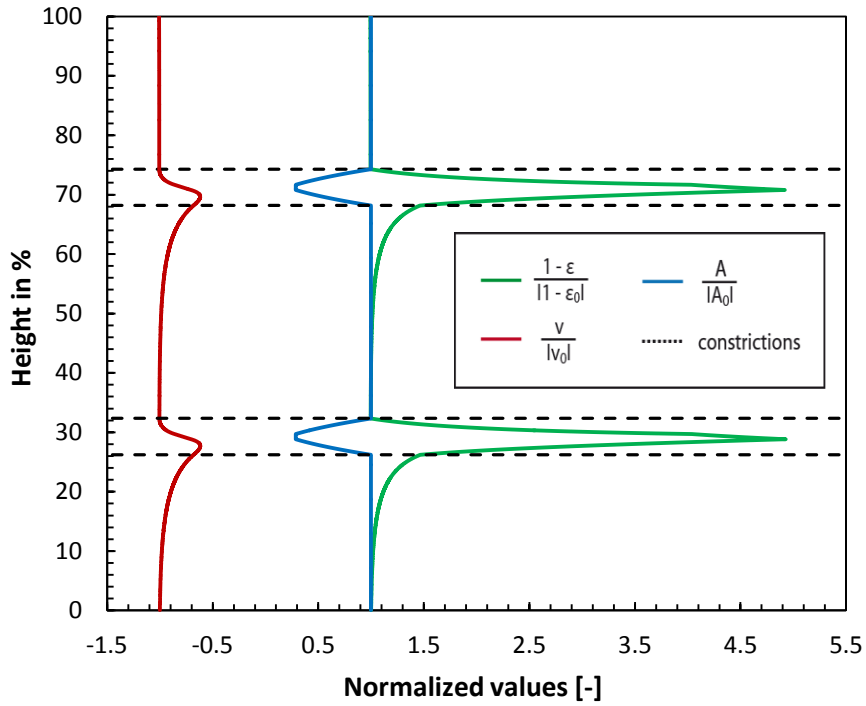


Figure 53: Conservation of mass simulated for the solid phase at the standard operating point

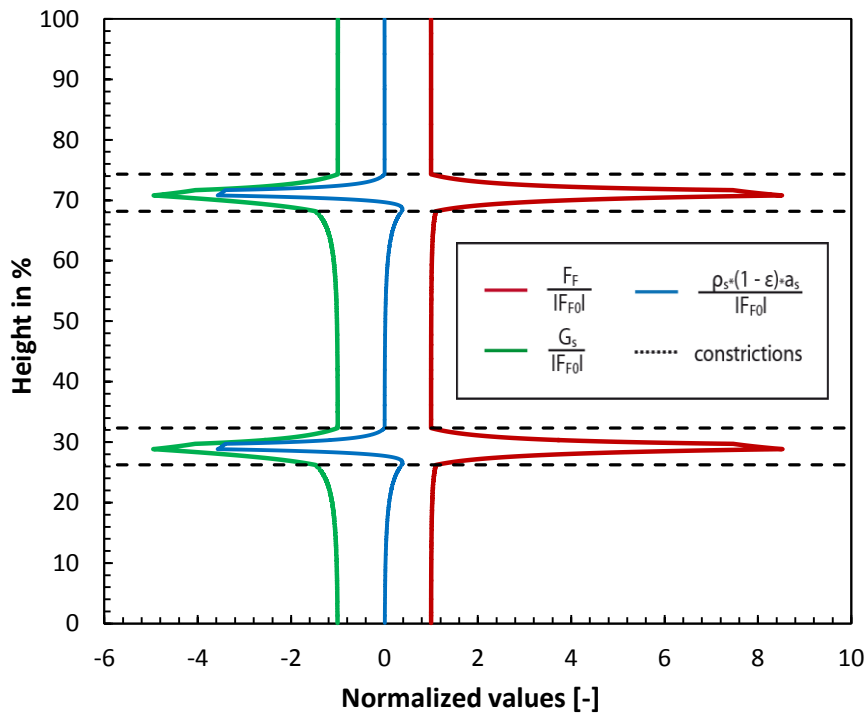


Figure 54: Equation of motion simulated for the solid phase at the standard operating point

Fluid phase:

As illustrated in Figure 55, inside the constriction occurs an increase of the fluid velocity, which is caused by the decreasing cross sectional area and the increasing solid fraction. This leads to a rise of the relative velocity between fluid and solid particles. The equation of motion of the fluid phase, depicted in Figure 56, shows that this causes a tremendous increase of the friction force as well as the pressure gradient (up to more than 900 %). Further, it shows that the pressure gradient is almost caused by the friction force, while the influence of the fluid acceleration term ($\rho_f * \epsilon * a_f$) is rather low. Furthermore, the influence of gravitational force of the fluid (G_f) is, due to the low fluid density so small that it is nearly not recognizable (approximately 0.8 %).

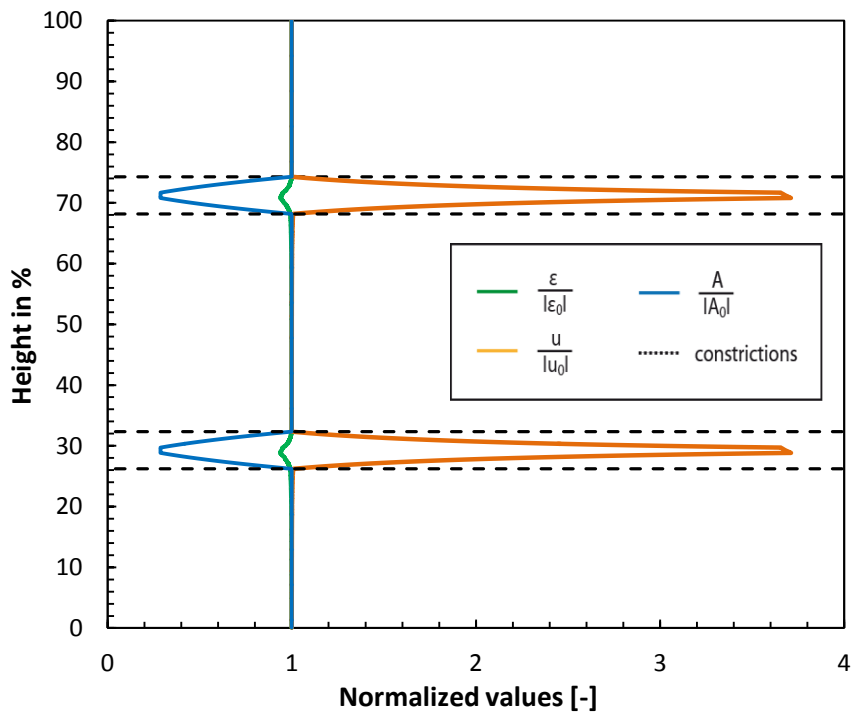


Figure 55: Conservation of mass simulated for the fluid phase at the standard operating point

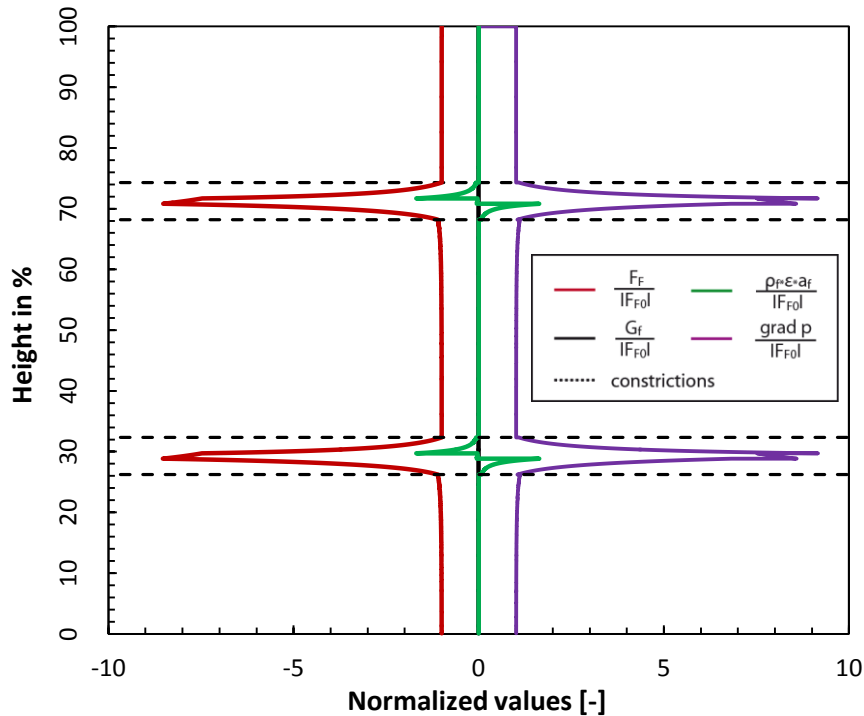


Figure 56: Equation of motion simulated for the fluid phase at the standard operating point

As solid phase and fluid phase are connected over the friction force, it can be noted that the pressure gradient of the fluid phase is mainly influenced by the gravitational force and acceleration force of the solid phase. Therefore, it can be concluded that the pressure gradient can be divided into two parts. One part representing the solid fraction and another valid for the acceleration of the solid phase.

5.6.2 Operating limitations

The operating limitations of the CFM are given by reaching an unstable operating point. To know these operating limitations and therefore the operating range of the CFM, for a constant AR fluidization, the FR fluidization was increased until stable operation was not possible anymore.

Figure 57 shows the operating range of the CFM for five AR fluidizations and three different bed material inventories in dependence of the AR and FR fluidization rate. Thereby, starting from the line and above stable operation is not possible anymore. The dashed black lines refer to the fluidization rates of the standard operating point. In Figure 58 the pressure profile over the FR for an unstable operation over time is depicted.

At an unstable operating condition, the FR is getting filled up with bed material until the FR fluidization rate is reduced or stopped. This behavior can be explained by equation 5.1, which was obtained by formation of the mass balance for the global circulation.

$$1 - \frac{\dot{m}_g}{\rho_s * v * A} > \epsilon_{mf} \quad (5.1)$$

As the particle velocity and the cross-sectional area inside the constriction are decreasing, the porosity has to decrease to fulfill the mass balance for the global circulation. However, this is only possible until the porosity at the minimum fluidization velocity is reached, because a further compaction is not possible anymore under fluidized bed conditions. In other words, at an unstable operating condition the mass flow which is entering the chamber is bigger than the mass flow which is leaving the chamber.

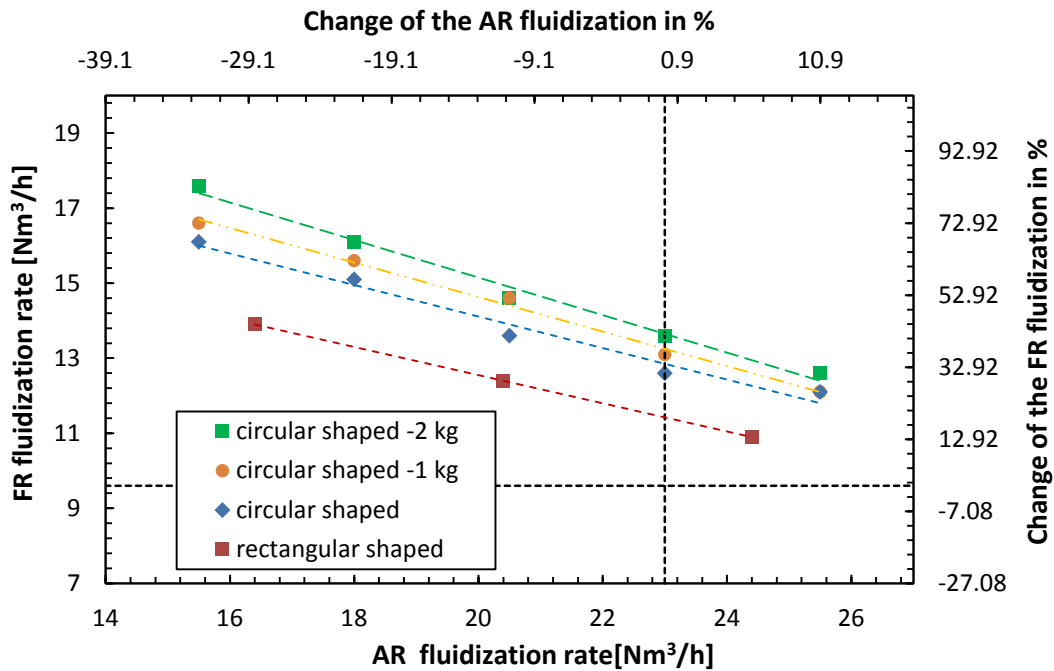


Figure 57: Overview of the operating range of the CFM

As illustrated in Figure 57, the FR with the circular cross-sectional area provides a significant larger operating range for all AR fluidization rates, than the FR with the rectangular cross-sectional area. This can be traced back to the fact that, for the same cross-sectional area, the reactor with the circular cross-sectional area has a 11.38 % smaller surface area than the reactor with the rectangular cross-sectional area. Therefore, the FR with the rectangular cross-sectional area offers more frictional surface along the wall, whereby the velocity of the particles gets more reduced than for the FR with the circular cross-sectional area.

The influence of the bed material inventory can be explained by an increase of the global circulation rate with the amount of bed material inside the CFM. This influence seems to decrease with the AR fluidization, contrary to the influence of the FR shape, which keeps constant over the whole AR fluidization range.

Further, from relative change of the fluidization rates with respect to the standard operating point, depicted in Figure 57, it can be observed that the FR fluidization has a stronger influence on the operating range compared to the AR fluidization.

Figure 58 illustrates the typical increase of the pressure over time and the height of the FR, which can be recognized while unstable operation. This is due to the increasing number of particles which accumulate inside the chambers over time and the related increased friction loss.

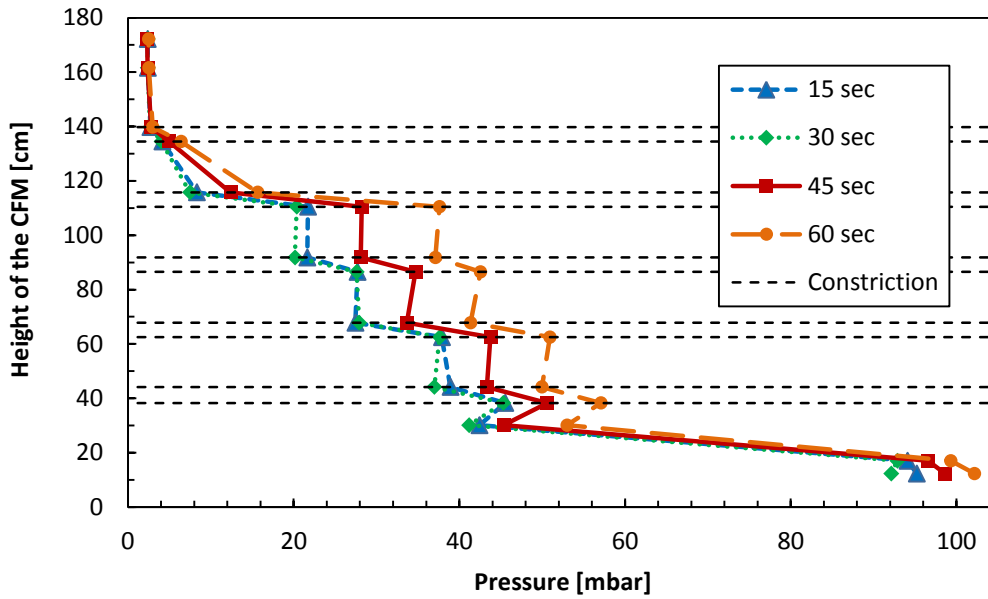


Figure 58: Pressure profile of the FR during unstable operation
 AR = 25.5 Nm³/h, ARI : ARII = 50 : 50, FR = 12.1 Nm³/h, FRI : FRII = 25 : 75, LLS = 0.8 Nm³/h,
 ULS = 0.8 Nm³/h, ILS = 0.6 Nm³/h

5.6.3 Last stable operating points

To estimate the characteristics at the last stable operating points, the pressure drop and pressure gradients over the whole FR as well as the second chamber were investigated.

Figure 59 and Figure 61 show, the pressure drops and the pressure gradients of the last stable operating points over the height of the FR as well as for the second chamber, while in the Figure 60 and Figure 62 the corresponding normalized pressure drops and pressure gradients are depicted.

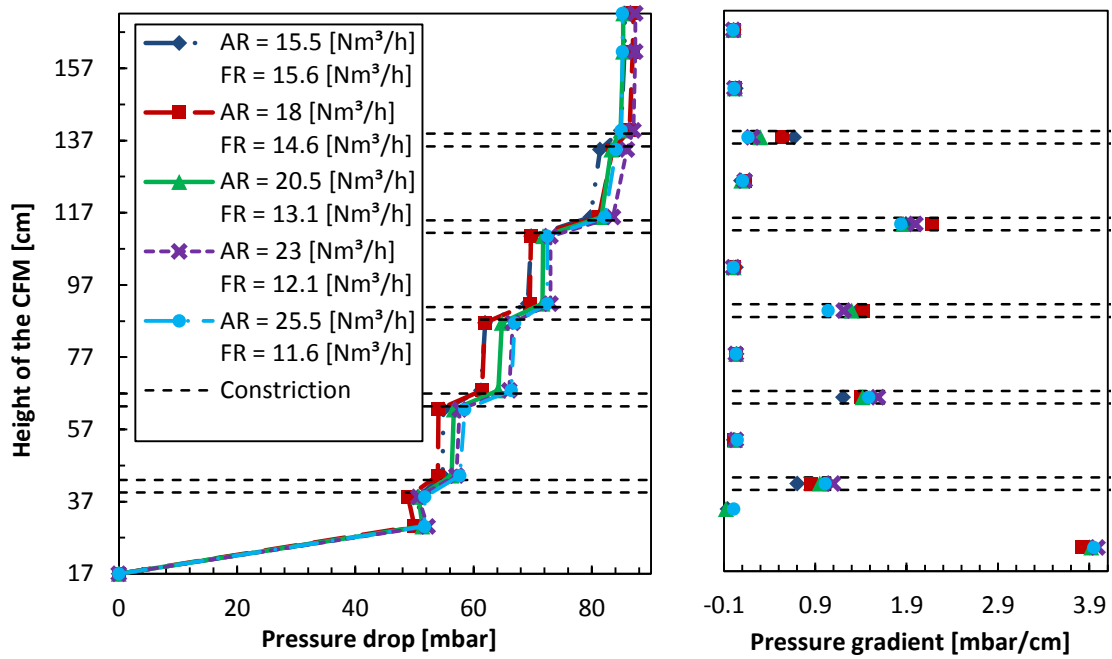


Figure 59: Pressure drop and pressure gradient over the FR at the last stable operating points
 ARI : ARII = 50 : 50, FRI : FRII = 25 : 75, LLS = 0.8 Nm³/h, ULS = 0.8 Nm³/h, ILS = 0.6 Nm³/h

As Figure 59 shows, that the total pressure drop over the FR is very similar for all last stable operating points. This suggests that at the transition from stable to unstable operation the FR contains always the same amount of solid particles. Further, the highest pressure gradient occurs always at constriction four, which leads to the assumption that the unstable operation condition (see equation 5.1) occurs at this constriction. This can be explained by the fact that the inlet of the ILS (returns particles into the FR) as well as the inlet of the ULS (transports particles from the AR into the FR) are situated above this constriction, so that this point represents a maximum of the solid flow into the FR.

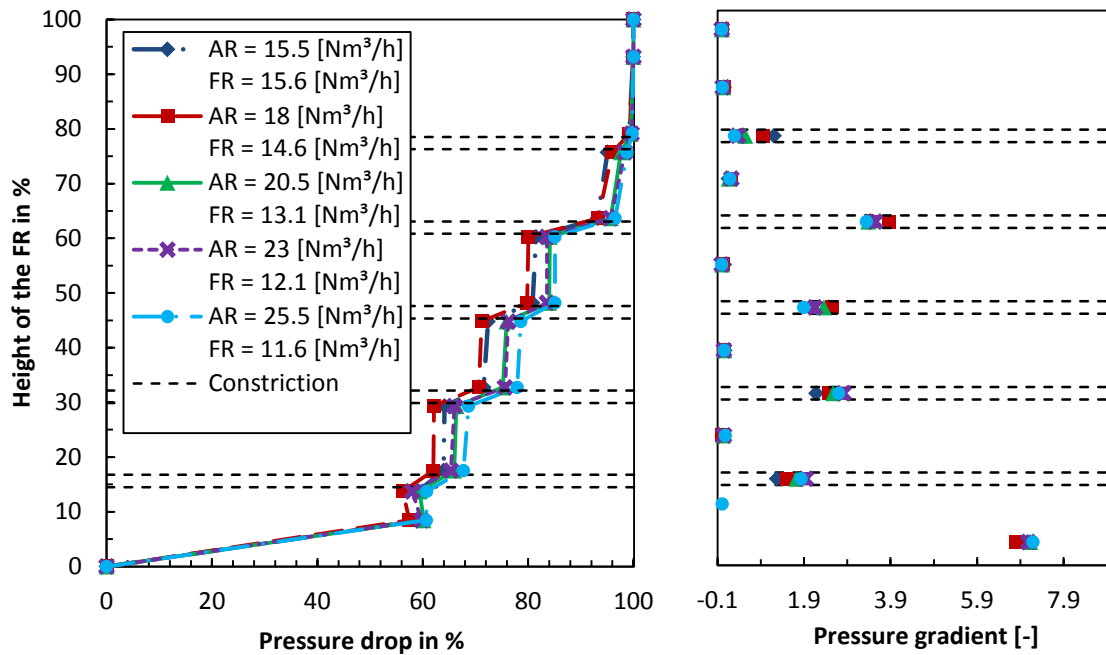


Figure 60: Normalized pressure drop and pressure gradient over the FR at the last stable operating points
 ARI : ARII = 50 : 50, FRI : FRII = 25 : 75, LLS = $0.8 \text{ Nm}^3/\text{h}$, ULS = $0.8 \text{ Nm}^3/\text{h}$, ILS = $0.6 \text{ Nm}^3/\text{h}$

The normalized pressure drops and pressure gradients, illustrated in Figure 60, show small deviations in the pressure drop distribution. Thereby, it can be recognized an increasing solid fraction in the higher situated chambers with the FR fluidization rate at the last stable operating points. This can be traced back to the stronger influence of the FR fluidization rate on the solid distribution (see chapter 5.3.1) than for the AR fluidization rate (see chapter 5.3.2).

The pressure drop over the second chamber at the last stable operating points, shown in Figure 61, is constantly growing with the AR fluidization until a fluidization of $23 \text{ Nm}^3/\text{h}$ is reached. Afterwards, it decreases the first time. This can be explained by the small deviations in the solid distribution over the whole FR (see Figure 60). Therefore an AR fluidization of $23 \text{ Nm}^3/\text{h}$ could represent a maximum for the highest possible mean solid fraction inside this chamber.

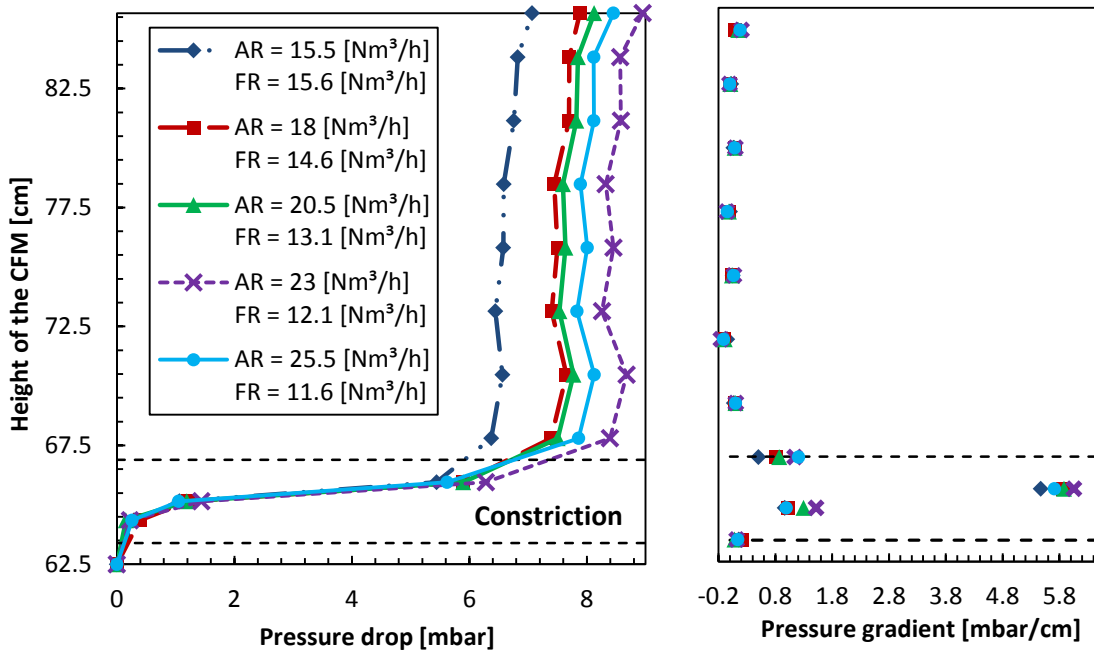


Figure 61: Pressure drop and pressure gradient over the second chamber at the last stable operating points
 ARI : ARII = 50 : 50, FRI : FRII = 25 : 75, LLS = 0.8 Nm³/h, ULS = 0.8 Nm³/h, ILS = 0.6 Nm³/h

Due to the fact that for all last stable operating points the solid fraction at the narrowest part of the constriction should be close to the bulk density at the minimum fluidization velocity, the pressure gradient at his point should also be very similar. This can be seen at the only small deviations of the pressure gradients in Figure 61 at the middle of the constriction.

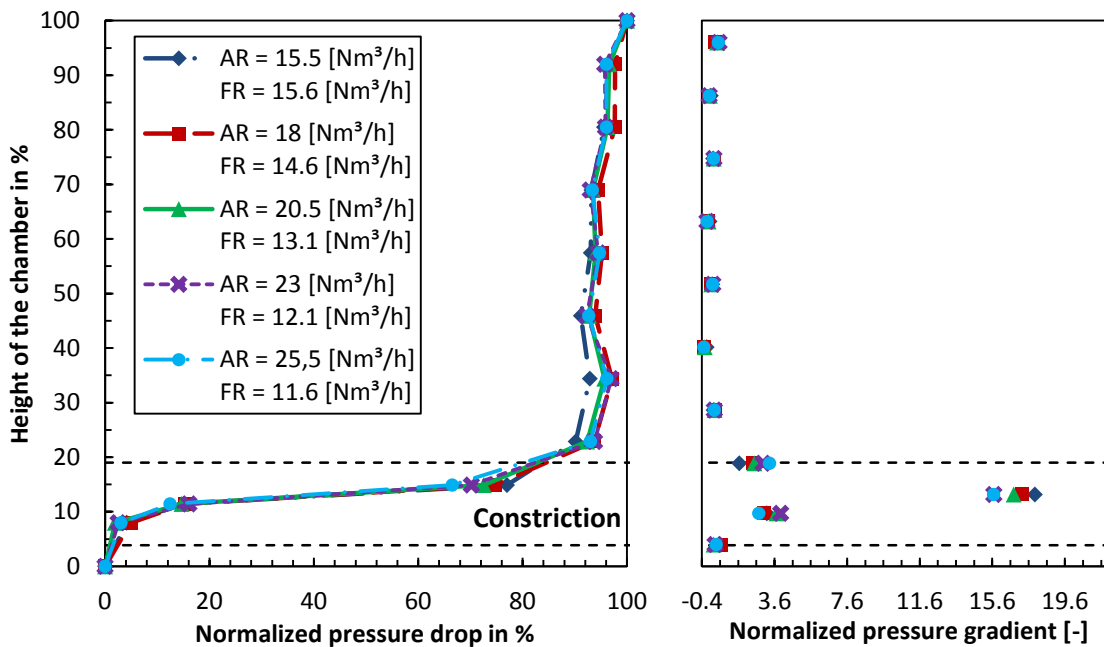


Figure 62: Normalized pressure drop and pressure gradient over the second chamber at the last stable operating points
 ARI : ARII = 50 : 50, FRI : FRII = 25 : 75, LLS = 0.8 Nm³/h, ULS = 0.8 Nm³/h, ILS = 0.6 Nm³/h

While for the variation of the fluidization rates from the standard operating point (see chapters 5.4.2 and 5.4.3) nearly no changes in the normalized pressure drop and pressure gradient were

recognizable, those of the last stable operating points, depicted in Figure 62, show significant larger deviations. As can be recognized from the normalized pressure gradient, these deviations occur mainly in the upper part of the constriction. Further, comparing normalized pressure drop and pressure gradient at the standard operating point (see Figure 48 and Figure 50) with those at the last stable operating points, it can be noticed that the standard operating point shows a different solid distribution than the last stable operating points. This indicates that the solid distribution in the chamber initially changes when near to unstable operation. Thereby, the share of the solid distribution of the upper end of the constriction (pressure port R3 to FR8/K1) increases while those at the middle of the constriction decreases.

6. Conclusion

A cold flow model (CFM) based on the novel DUAL FLUID reactor concept has been investigated. This new reactor concept, with simple geometrical constrictions inside the fuel reactor (FR) was developed at the Vienna University of Technology and constitutes an advanced development of the Dual Circulating Fluidized Bed technology (DCFB).

The installation of these constrictions in the FR has two main reasons. Due to the increased superficial gas velocity in the constrictions, the solid fraction should be increased over the entire height of the FR. Further, it is expected that after each constriction zones of turbulent fluidization regimes develop, which ensure dense areas of particles as well as excellent mixing conditions.

For the investigation of the CFM, pressure measurements were performed at 40 positions distributed over the model. For evaluation of the influence of the constrictions on the solid fraction and distribution of one chamber, three measurement ports were placed inside one constriction and eight more between two constrictions. Additionally, a mathematical model for the fluid dynamic simulation of the constrictions, based on the conservation of mass and the equation of motion, was developed. Further, to be able to draw conclusions about the solid mass flows inside the CFM, the global and internal circulation were determined.

Both, the measurement data and the mathematical model clearly confirm the expected increase of the solid fraction over the height of the FR. The huge increasing pressure gradients over the constrictions compared to that between the constrictions (up to more than 100 times) clearly show this. Further, the highest particle concentration could be identified in the upper part of the constrictions via the pressure profile of the second chamber.

The solid distribution over the height of the FR can be influenced by the AR and FR fluidization rate with stronger influence of the FR fluidization rate. Thereby the share of the solid distribution of the upper parts increases with increasing AR as well as FR fluidization rate. Contrary to the FR, the pressure distribution of the second chamber indicates that the solid distribution in the chambers is neither influenced by the AR fluidization rate nor by the FR fluidization rate.

At some operating points the new reactor concept shows a totally different behavior than the classic designs without constrictions. At certain operating conditions, the mass flow which is entering a chamber is bigger than the one leaving it. This leads to unstable operation and consequently to a limitation of the operating range. Using the developed mathematical model for the fluid dynamic simulation of the constrictions, it was possible to discover the mechanisms which lead to this behavior. Further, the investigations showed that the ratio of the AR to FR fluidization can be used to describe the limits of the operating range of the CFM.

Investigations at the last stable operating points showed that the FR contains always similar amount of solid particles at the transition to unstable operation. Further, it showed that at the last stable operating points the pressure distribution changes. This leads to the assumption that the solid distribution in the chambers changes for operation close to unstable operation.

7. References

- [1] Smil, V., "Energy: A Beginner's Guide (Beginner's Guides)", Oneworld Publications, London, United Kingdom, 2006
- [2] IEA, Key World Energy Statistics 2013, available online at www.iea.org, 2013
- [3] Mitchell, John F. B., "THE "GREENHOUSE" EFFECT AND CLIMATE CHANGE", Reviews of Geophysics (American Geophysical Union) 27 (1), 1989, pp. 115–139
- [4] Solomon, S., Qin, D., Manning, M., Chen, Z., Marquis, M., Averyt, K.B., Tignor, M., Miller, H.L. (Eds.), IPCC, "Climate Change 2007: The Physical Science Basis", Contribution of Working Group I to the Fourth Assessment Report of the Intergovernmental Panel on Climate Change, 2007, Cambridge University Press, Cambridge, United Kingdom and New York, NY, USA
- [5] IEA, World Energy Outlook 2010, available online at www.iea.org, 2010
- [6] Metz, B., Davidson, O., de Coninck, H.C., Loos, M., Meyer, L.A. (Eds.), IPCC, "IPCC Special Report on Carbon Dioxide Capture and Storage", Prepared by Working Group III of the Intergovernmental Panel on Climate Change, Cambridge University Press, Cambridge, United Kingdom and New York, NY, USA, 2005
- [7] Pröll, T., "Innovative Fuel Conversion with CO₂ Capture Using Dual Fluidized Bed Systems", Habilitation, 2011
- [8] Lyngfelt, A., Leckner, B., and Mattisson, T., "A fluidized-bed combustion process with inherent CO₂ separation; Application of chemical-looping combustion", Chemical Engineering Science, 2001, pp. 3101-3113
- [9] Penthor, S., Pröll, T., Hofbauer, H., "Chemical-looping combustion using biomass as fuel", Proc. 2nd Oxyfuel Combustion Conference, 2011, Yeppoon, Australia
- [10] von Bökh, P., Saumweber, C., "Fluidmechanik: Einführendes Lehrbuch", Springer Vieweg, Karlsruhe, Deutschland, 3. Auflage, 2013
- [11] Böswirth, L., Bschorer, S., "Technische Strömungslehre", Vieweg und Teubner, Wiesbaden, Deutschland, 9. Auflage, 2012
- [12] Surek, D., Stempin, S., "Angewandte Strömungsmechanik für Praxis und Studium", Teubner Verlag, Wiesbaden, Deutschland, 1. Auflage, 2007
- [13] Ziegler, F., "Technische Mechanik der festen und flüssigen Körper", Springer Vienna, Wien, Österreich, 3. Auflage, 1998
- [14] Fan, L. S., Zhu, C., "Principles of Gas-Solid Flows", Cambridge University Press, Cambridge, United Kingdom, First Edition, 1998

- [15] Yang, W. C., "FLUIDIZATION, SOLIDS HANDLING, AND PROCESSING, Industrial Applications", NOYES Publications, Westwood, New Jersey, 1998
- [16] Kunii, D., Levenspiel, O., "Fluidization Engineering", Butterworth Heinemann, Stoneham, Massachusetts, Second Edition, 1991
- [17] Geldart, D., "Types of gas fluidization", Powder Technology, 1973, pp. 285-292
- [18] Kunii, D., Levenspiel, O., "Circulating fluidized-bed reactors", Chemical Engineering Science, Vol. 52, No. 15, 1997, pp. 2471-2482
- [19] Hofbauer, H., "Skriptum: Grundlagen der Wirbelschichttechnik", TU Wien, 6. Auflage, 2013
- [20] Grace, J. R., "Circulating Fluidized Beds", BLACKIE ACADEMIC and PROFESSIONAL, London, United Kingdom, First Edition, 1997
- [21] Schmid, J. C., Pröll, T., Pfeifer, C., Rauch, R., Hofbauer, H., "COLD FLOW MODEL INVESTIGATION ON A MODIFIED RISER WITH ENHANCED GAS-SOLID CONTACT – LOCATING THE REGIONS OF OPERATION IN A FLUIDIZATION REGIME MAP", Proc. 21st International Conference on Fluidized Bed Combustion (FBC), Naples, Italy, 2012, pp. 80-87
- [22] GLICKSMAN, L. R., "SCALING RELATIONSHIPS FOR FLUIDIZED BEDS", Chemical Engineering Science Vol. 39, No.9, 1984, pp. 1373-1379
- [23] Pröll, T., Kolbitsch, P., Bolhär-Nordenkampf, J., Hofbauer, H., "A Novel Dual Circulating Fluidized Bed System for Chemical Looping Processes", American Institute of Chemical Engineers Vol. 55, No. 12, 2009, pp. 3255-3266
- [24] Schmid, J. C., Pröll, T., Pfeifer, C., Hofbauer, H., "IMPROVEMENT OF GAS-SOLID INTERACTION IN DUAL CIRCULATING FLUIDIZED BED SYSTEMS", Proc. 9th European Conference on Industrial Furnaces and Boilers (INFUB), Estoril, Portugal, 2011
- [25] Arens, T., Hettlich, F., Karpfinger, Ch., Kockelkorn, U., Lichtenegger, K., Stachel, H., "Mathematik", Spektrum Akademischer Verlag, Heidelberg, Deutschland, 1. Auflage, 2009
- [26] Fuchs, J., "Ermittlung des Betriebskennfeldes einer innovativen Zweibett-wirbelschicht anhand von Kaltmodelluntersuchungen", Diplomarbeit, TU Wien, 2013
- [27] Decker, S., "Berechnung von gerührten Suspensionen mit dem Euler-Lagrange-Verfahren", Dissertation, Martin-Luther-Universität-Halle Wittenberg, 2005

8. Nomenclature

APF	Absolute pressure fluctuations method
AR	Air reactor
AR CYL LS	Air reactor cyclone loop seal
CFM	Cold flow model
DCFB	Dual circulating fluidized bed
DPF	Differential pressure fluctuations method
FR	Fuel reactor
FR CYL LS	Fuel reactor cyclone loop seal
ILS	Internal loop seal
LLS	Lower loop seal
SEP AR	Separator air reactor
SEP FR	Separator fuel reactor
ULS	Upper loop seal
β	[kg/m ³ s]	Coefficient of drag force
Δ	[-]	Distributor plate voidage
ϵ	[-]	Porosity
ϵ_B	[-]	Bed porosity
ϵ_m	[-]	Mean porosity
ϵ_{mf}	[-]	Porosity at the minimum fluidization velocity
μ	[Pa s]	Dynamic viscosity
ρ	[kg/m ³]	Density
ρ_B	[kg/m ³]	Bulk density
ρ_p	[kg/m ³]	Particle density
ρ_f	[kg/m ³]	Fluid density
ρ_s	[kg/m ³]	Solid density
ψ	[-]	Sphericity
A	[m ²]	Cross sectional area
A_{eff}	[m ²]	Effective cross sectional area
$A_{downcomer}$	[m ²]	Cross sectional area of the downcomer
a_f	[m/s ²]	Acceleration of fluid
A_p	[m ²]	Projected area of the particle
Ar	[-]	Archimedes number
A_{riser}	[m ²]	Cross sectional area of the riser
a_s	[m/s ²]	Acceleration of solid
c_D	[-]	Drag coefficient
d	[m]	Diameter
D	[m]	Diameter of the risers
d_p	[m]	Sieve diameter
d_{pm}	[m]	Mean sieve diameter
d_s	[m]	Surface diameter
d_{sv}	[m]	Sauter diameter
d_{svm}	[m]	Mean Sauter diameter
d_v	[m]	Volume diameter
F_F	[N/m ³]	Friction force
Fr	[-]	Froude number
g	[m/s ²]	Gravitational constant

G_f	$[\text{N}/\text{m}^3]$	Gravitational force fluid phase
G_s	$[\text{kg}/\text{m}^2 \text{ s}]$	Global circulation rate
G_s	$[\text{N}/\text{m}^3]$	Gravitational force solid phase
h	$[\text{m}]$	Height
H	$[\text{m}]$	Bed height
H_0	$[\text{m}]$	Initial height
\dot{m}_g	$[\text{kg}/\text{s}]$	Global solid flow
M	$[\text{kg}]$	Mass
M_p	$[\text{kg}]$	Particle mass
p	$[\text{Pa}]$	(Static) pressure
p_{dyn}	$[\text{Pa}]$	Dynamic pressure
p_{tot}	$[\text{Pa}]$	Total pressure
Re	$[-]$	Reynolds number
Re_c	$[-]$	Reynolds number at turbulent fluidization velocity
Re_{umf}	$[-]$	Reynolds number at minimum fluidization velocity
Re_{se}	$[-]$	Reynolds number at significant entrainment velocity
s	$[-]$	Factor for reducing the fluid velocity
T	$[\text{°C}]$	Temperature
u	$[\text{m}/\text{s}]$	Fluid velocity
U_0	$[\text{m}/\text{s}]$	Superficial velocity
U_c	$[\text{m}/\text{s}]$	Turbulent velocity
U_{mb}	$[\text{m}/\text{s}]$	Minimum bubbling velocity
U_{mf}	$[\text{m}/\text{s}]$	Minimum fluidization velocity
U_{slip}	$[\text{m}/\text{s}]$	Slip velocity
U_{se}	$[\text{m}/\text{s}]$	Significant solid entrainment velocity
U_t	$[\text{m}/\text{s}]$	Terminal velocity
v	$[\text{m}/\text{s}]$	Solid velocity
V	$[\text{m}^3]$	Volume
\dot{V}	$[\text{kg}/\text{s}]$	Fluid flow
v_0	$[\text{m}/\text{s}]$	Initial solid velocity
V_B	$[\text{m}^3]$	Bulk volume
v_n	$[\text{m}/\text{s}]$	Velocity normal to the wall
V_p	$[\text{m}^3]$	Particle volume

9. List of Figures

Figure 1: Development of the worldwide energy demand over time in million tons of oil equivalent (Mtoe) [2]	1
Figure 2: Influence of the most important green house gases expressed by their radiative forcing [4]	2
Figure 3: Development of the worldwide CO ₂ emissions over time by fuel in megatonnes (Mt) [2]	3
Figure 4: CO ₂ e savings relative to the Current Policies Scenario [5]	3
Figure 5: CO ₂ emissions with and without CCS [6]	4
Figure 6: Comparison of transportation costs by ship and pipeline [6]	6
Figure 7: Principal of a CLC process.....	8
Figure 8: Measuring methods for pressure [10]	12
Figure 9: Streamlines of flow due to inertial effects.....	14
Figure 10: Geldarts classification of fluidized bed materials [14]	17
Figure 11: Progression of the pressure drop with superficial gas velocity	18
Figure 12: Development of the drag coefficient for a sphere with the Reynolds number [14]	20
Figure 13: Fluidization regimes and corresponding typical solid distributions [21]	21
Figure 14: Regime map according to Reh [21]	23
Figure 15: Regime map according to Grace [21].....	23
Figure 16: Novel DUAL FLUID reactor concept [21]	27
Figure 17: pressure drop, pressure gradient and particle volume fraction [24].....	28
Figure 18: Elevation view of the CFM	29
Figure 19: Drawing of a constriction	29
Figure 20: Ground plan of the CFM.....	30
Figure 21: Flow chart of the CFM [26]	31
Figure 22: Classification of the bed materials according to Geldart	32
Figure 23: Particle size distribution Ilmenite.....	33
Figure 24: Particle size distribution Bronze.....	33
Figure 25: Image of bronze particles [26]	34
Figure 26: Position of the operating points of the CFM and the CLC demonstration plant in a regime map	36
Figure 27: Principal of variable area meter	36
Figure 28: Pressure measurement ports in the AR and FR	38
Figure 29: Pressure measurement ports at the ILS.....	39
Figure 30: Pressure measurement ports at the ULS	39
Figure 31: Global and internal circulation.....	40
Figure 32: Schema of the mathematical model	43
Figure 33: Solution of the equations	44
Figure 34: Overview of the pressure in the CFM without bed material	47
Figure 35: Pressure profile over the second constriction	48
Figure 36: Overview of the pressure in the CFM with bed material.....	49
Figure 37: Development of the global circulation with the AR fluidization rate for FR = 7.6 Nm ³ /h	51

Figure 38: Development of the global circulation with the AR fluidization rate for FR = 12.6 Nm ³ /h	51
Figure 39: Comparison of the global circulation rate for different FR fluidization rates.....	52
Figure 40: Development of the internal circulation.....	53
Figure 41: Pressure drop and pressure gradient over the height of the FR by variation of the FR fluidization rate	55
Figure 42: Normalized pressure drop and pressure gradient over the height of the FR by variation of the	56
Figure 43: Pressure drop and pressure gradient over the height of the FR by variation of the AR fluidization rate	57
Figure 44: Normalized pressure drop and pressure gradient over the height of the FR by variation of the	58
Figure 45: Pressure profile over the second chamber without fluidization of the AR.....	59
Figure 46: Pressure drop and pressure gradient over the second chamber by variation of the FR fluidization rate	60
Figure 47: Influence of particle vortex on the pressure gradient	61
Figure 48: Normalized pressure drop and pressure gradient over the second chamber by variation of the	62
Figure 49: Pressure drop and pressure gradient over the second chamber by variation of the AR fluidization rate	63
Figure 50: Normalized pressure drop and pressure gradient over the second chamber by variation of the	64
Figure 51: Progress of the mean overall solid fraction in a chamber in dependence of the FR fluidization rate	65
Figure 52: Basic mechanisms in a chamber	66
Figure 53: Conservation of mass simulated for the solid phase at the standard operating point	68
Figure 54: Equation of motion simulated for the solid phase at the standard operating point....	68
Figure 55: Conservation of mass simulated for the fluid phase at the standard operating point.	69
Figure 56: Equation of motion simulated for the fluid phase at the standard operating point	70
Figure 57: Overview of the operating range for the CFM.....	71
Figure 58: Pressure profile of the FR during unstable operation.....	72
Figure 59: Pressure drop and pressure gradient over the FR at the last stable operating points.	73
Figure 60: Normalized pressure drop and pressure gradient over the FR at the last stable operating points	74
Figure 61: Pressure drop and pressure gradient over the second chamber at the last stable operating points	75
Figure 62: Normalized pressure drop and pressure gradient over the second chamber at the last stable	75

10. List of Tables

Table 1: Full set of scaling relationships.....	26
Table 2: Scaling parameters for AR and FR	34
Table 3: Dimensionless numbers AR	35
Table 4: Dimensionless numbers FR	35
Table 5: Calibration values	36
Table 6: Operating ranges of the variable area meter.....	37
Table 7: Arrangement of the chambers in the FR.....	38
Table 8: Height of the pressure measurement ports in the CFM	39
Table 9: Cross section areas	41
Table 10: Fluidization rates at standard operating point.....	46